Sub-GHz Resolution On-chip Silicon Nitride Spectrometer for C-band Scanning

Houman Ghorbani

Thesis submitted to the University of Ottawa
in partial Fulfillment of the requirements for the
Doctor of Philosophy Degree in Electrical and Computer Engineering

School of Electrical Engineering and Computer Science
Faculty of Engineering
University of Ottawa

Abstract

The thesis is based on an industry project offered to our research laboratory. The industry required the feasibility evaluation of designing a spectrometer that scans the C-band (1530 – 1565 nm) with a resolution of lower than 1 GHz, has a scanning speed of at least 10 Hz, a maximum occupied area of 10 square centimeters, and a maximum consumed power of 3 watts. A compact integrated solution to fulfill the requirements was considered. The ring resonator and arrayed waveguide grating (AWG) were selected as the fine and coarse filter, respectively; being the main components of the spectrometer. Among different integrated platforms silicon nitride was chosen because of its relatively low loss performance and small footprint compared to other available platforms. The ring resonator needs to have a resolution of lower than 1 GHz and be tunable over its free spectral range (FSR) to scan the whole C-band. The AWG on the other hand needs to separate the individual resonant frequencies that exit the ring resonator. Conventional AWGs have bell-shaped channel profiles and cannot achieve flat output responses for varied input frequency. Thus, the incoherent weighted summation technique was used to construct virtual channel profiles (VCP) from AWG channel profiles to attain a flat on-resonance frequency response over the C-band. This method requires the ring resonator FSR to be as large as possible relative to AWG channel spacing, and the AWG channel profiles have overlapping passbands that intersect sufficiently above noise level, to achieve desired crosstalk performance. After choosing the right method and finding out performance requirements for the ring resonator and AWG, the feasibility of designing a silicon nitride ring resonator to have a resolution of lower than 1 GHz was evaluated. This step includes bend simulation to acquire the minimum bend radius, transmission

simulations to know the right power coupling ratio to achieve a resolution of lower than 1 GHz and determining the minimum gap size in the ring coupler region. Next, the thermal tunability of the ring resonator was assessed by simulation to determine maximum tunable FSR of the ring resonator, its consumed power, and scanning speed. In the following, based on the requirements imposed by the incoherent weighted summation method, and known maximum tunable ring resonator FSR, design specifications for the AWG were determined, and the feasibility of designing the target AWG was evaluated by simulation. Finally, the combined performance of the ring resonator and AWG was simulated to evaluate the spectrometer as a whole. The industry requirements for the spectrometer including the frequency range, resolution, consumed power, scanning speed, and area are met. The scanning of the C-band with a resolution of lower than 1 GHz significantly beefs up the capacity of the band by allowing the use of a huge number of channels and the effective monitoring of the band to use empty channels or replace damaged ones.

Dedicated to:

Ehsan

Acknowledgements

Pursuing a Ph.D. program typically requires four to five years to complete; however, my journey extended beyond this timeframe. Throughout this period, I encountered unforeseen challenges and gained invaluable lessons that transcended the scientific scope of my research. Although I faced setbacks that occasionally hindered my progress, I remained firm in my determination and ultimately reached the finish line. As a resolute individual, I worked tirelessly to achieve my goal. Nevertheless, the support I received from numerous individuals was pivotal, without which I could not have succeeded. I am grateful to all those who supported me.

I express my gratitude to Professor Ramanand Tewari and Professor Neda Nabavi for their inestimable support, which extended beyond the academic sphere. Additionally, I extend my appreciation to Ms. Suzanne St-Michel, Professor Michel Saydé, Mr. Mathieu Leclair, and Ms. Alexandra McAllister for their generous support and insightful guidance. I wish them all the very best.

I appreciate the financial support provided by the Department of Electrical Engineering and Computer Science through teaching assistantships and by the Financial Aid and Awards Office through scholarships. I extend my heartfelt gratitude to Mr. Daniel Melanson and Ms. Myriam Diafwila for their thoughtful and kindly support.

I express my profound appreciation to Professor Michel Labrosse, Dean of the Faculty of Engineering, for his gracious support in ensuring my program proceeded without administrative obstacles. Additionally, the uninterrupted support provided by the Graduate Office of the Faculty of Engineering was instrumental. I am greatly thankful for

all the support received. In particular, I extend my sincere gratitude to Ms. Sylvie Chénier for her considerate guidance and priceless advice.

Despite being thousands of miles away, my mother and grandmother consistently provided steady support and encouragement throughout my journey. They made every effort to ensure my success and well-being. I express my deepest appreciation for their unconditional and precious support and kindness.

Finally, and most significantly, I express my profound gratitude to my brother and true friend, Ehsan. His essential and unwavering support lifted me from despair, as though guiding me to rise. I am deeply grateful to Ehsan for his steadfast presence during my most challenging moments.

Acronyms

2D	Two-Dimensional
3D	Three-Dimensional
ADS	Asymmetric Double Strip
AWG	Arrayed Waveguide Grating
BPM	Beam Propagation Method
CCPR	Cross-Coupling Power Ratio
CMT	Coupled Mode Theory
EME	Eigen-Mode Expansion
EO	Electro-Optic
ER	Extinction Ratio
EON	Elastic Optical Network
FDM	Finite Difference Method
FEM	Finite Element Method
FPR	Free Propagation Region
FPV	Fabrication Process Variation
FSR	Free Spectral Range
FT	Fourier Transform
FWHM	Full Width at Half Maximum
GMZDI	Generalized Mach-Zehnder Delay Interferometer
MEMS	Micro Electro Mechanical Systems
MMI	Multi-Mode Interferometer
MTM	Matrix Transfer Method
MZDI	Mach-Zehnder Delay Interferometer
MZI	Mach-Zehnder Interferometer
PE	Piezo-Electric
PEC	perfect electrical conductor
PEG	Planar Echelle Grating
PIC	Photonics Integrated Circuit

SDN	Software Defined Networking
SOI	Silicon On Insulator
TO	Thermo-Optic
VCP	Virtual Channel Profile
WGM	whispering gallery mode

Table of Contents

Table of Figures

List of Tables

Chapter 1 Introduction

1.1 Motivation and specifications

Nowadays, with the invention of the internet and advance of digital technology, communications infrastructure across the globe needs to be regularly upgraded to meet exponentially growing capacity requirements. Optical fibers, due to their higher center frequencies with respect to microwave transmission means, provide high speed data channels while not being affected by weather conditions and electromagnetic interference [1], [2]. Nonetheless, due to high user demand, optical communications face challenges in their available capacity [3], [4].

Different methods are proposed that improve the capacity of optical communication systems [5], [6]. One of the techniques to improve channel efficiency is to pack optical channels closer to each other. While dense packing of data channels is easier in the microwave domain, performing the technique in the optical domain adds flexibility to replace data channels in the optical domain without needing to down modulate the entire signal to the microwave domain and up modulate it back to the optical domain. To take advantage of densely packed optical channels, high-resolution optical filtering [7], [8], [9] is required to comprehensively monitor the band and find out each channel's state and adjust allocations to channels based on availability and user requests. This flexibility allows the optical network to be programmable and easier to manage on how and to where data should be flowed. This concept is called Software Defined Networking (SDN) [10], [11], [12], and its implementation on the physical layer (fiber optics layer) makes it an Elastic Optical Network (EON) [13], [14].

Another application of high-resolution optical filters is in sensing [15], [16], [17]. high-resolution optical filters, which are usually achieved by light resonating at a certain frequency, are sensitive to the slightest changes in the surrounding environment and thus, can be used in bio-photonics to detect molecular changes in a certain tissue. Also, they can be used for structural health monitoring of civil infrastructure to detect changes in the dimensions of structures.

High-resolution optical filters also have applications in nonlinear optics [18], [19]. An optical resonator needs to have a high resolution to unfold nonlinear properties such as four-wave mixing or Kerr effects used for generating frequency combs or creating ultra-fast optical switches.

The comprehensive monitoring of an optical network requires cost effective technology and hence, compact integrated solutions that leverage the economics of mass production. On-chip technologies not only reduce the room occupied by the device and thus, make it easier to mount on platforms with space limitations, but also decrease power consumption, sensitivity to ambient factors such as temperature, humidity, shock, and so on [20], [21].

The C-band (1530 – 1565 nm) is the most crowded optical band in communications and has drawn significant attention from academia and industry to improve its efficiency. In 2018, the feasibility evaluation of designing a spectrometer with the following specifications was proposed by industry to our research group:

1) Monitoring range: C-band (1530 – 1565 nm)
2) Resolution: < 1 GHz

3) Scanning rate: > 10 Hz

4) Power consumption: < 3 W

5) Measurement accuracy: < 1dB

6) Size: < 10 cm^2.

The length of the C-band is 35 nm or equivalently 4.4 THz. The capability of scanning the C-band with a resolution of lower than 1 GHz allows partitioning it into 4400 channels, each with a bandwidth of no more than 1 GHz, significantly improving the band capacity, its flexibility, and network efficiency. On the other hand, the specified limits in power consumption and spectrometer size implies that a compact integrated spectrometer is the right choice because of cost effectiveness alongside the other advantages of an integrated solution namely reduced vulnerability to ambient conditions such as mechanical vibration, temperature, moisture and so on.

In the following, the components used in the spectrometer design are selected and the right platform that satisfies the specifications is introduced. Next, the objectives of the thesis are clarified. Then, the thesis structure is demonstrated. Finally, the list of publications worked on during the program that are directly or otherwise related to the thesis is provided.

1.2 Spectrometer components

Spectrometers are used to determine the state of spectrum in a signal. Optical spectrometers are categorized into four general types in [22]:

The first type are dispersive devices. The prism is a good example of it in bulk optics where light is directed at a distinct angle depending on its frequency and is read out on the receiver plane [23]. Examples of on-chip dispersive components are Planar Echelle Gratings (PEG) [24], [25], and Arrayed Waveguide Gratings (AWG) [26], [27].

The second type is the narrowband filter. They filter out a certain frequency spectrum at the resonant frequency of the filter. These filters do not have just one resonant frequency; rather, the filter can generate a comb of resonant frequencies over a certain frequency band where each comb element is a resonant frequency spaced from the adjacent resonant frequency by the free spectral range (FSR) of the filter. The resonant frequency array can move versus frequency by tuning the filter. Fabry-Pérot filters [28], and whispering gallery mode (WGM) resonators [9], [29] are examples of narrowband filters in bulk optics while ring resonators [30] are for integrated optics. They can achieve sub-GHz resolutions provided their loss is reduced sufficiently. However, to scan a certain bandwidth they need to be tuned by the amount of their FSRs.

The third type is the Fourier Transform (FT) spectrometer. They are made of interferometers where light is split into at least two branches. The light gains different phase in each path depending on optical path length difference and frequency. The frequency response of the spectrometer is repeated in each FSR, which is dependent on optical path length difference. The Michelson interferometer [31] and Mach-Zehnder interferometer (MZI) [32] are examples of FT spectrometers. Tuning is achieved by changing the phase shift in the paths of the interferometer.

The fourth type of spectrometers is reconstructive spectrometer [33], [34], which as the name suggests, reconstructs its input spectral response from the spatial and frequency components of the received response as well as the expected spatial and frequency patten for all spectral components by carrying out computations. It is possible to extract the spectrum of any signal — with certain resolution that is dependent upon the length of the signal in time domain — using this method provided mathematical calculations are effectively conducted.

Based on the specifications of the industry defined spectrometer, the second type is a suitable option as it has the potential to achieve sub-GHz resolution. The first and third type cannot achieve the specified resolution and sweep the C-band with that resolution. The fourth type may work well, but needs a large amount of computation, which adds to its complexity and power consumption. Thus, the ring resonator is a suitable candidate to achieve a resolution of lower than 1 GHz as a compact integrated narrow band filter.

The ring resonator must be made on a low loss platform to achieve a resolution of lower than 1 GHz, and its resonant frequency must be tunable over its FSR to scan the entire frequency range within the FSR. To scan the C-band with a ring resonator, its FSR needs to be larger than the length of the C-band which is circa 4.4 THz. The FSR of a ring is inversely proportional to its radius; hence, increasing the FSR requires tighter bends. On the other hand, its radius must be large enough to prevent bend loss to negatively impact the resolution. The ring resonators made on available photonics integrated circuits (PIC) platforms cannot reach an FSR in the order of THz because of the required tight bends that enormously augment bend loss and thus, cannot have a

resolution of lower than 1 GHz. Consequently, the ring resonator FSR is going to be lower than the C-band length. In this case, multiple resonant frequencies exist within the C-band and a second filter is needed to separate the resonant points for a full C-band scan. The resonant frequencies of the ring resonator can be spaced enough so that a dispersive filter such as a PEG or an AWG as a coarse filter can separate the resonant frequencies. The AWG and PEG apply the same mechanism to separate light into different frequency components. In both devices, light is radiated into an array and each array element adds a specific phase shift to light. After traversing in the array, depending upon the array phase arrangement, light is directed toward the device output at a distinct angle. The phase shift is dependent on frequency. Therefore, each frequency component gains a different phase shift and is directed to the output at a different angle. The AWG is selected as the coarse filter, and in combination with the ring resonator as the fine filter, constitutes the key components of the spectrometer.

1.3 Integration platform

Among available PIC platforms, CMOS compatible platforms are desired due to their easy integration with electronic circuitry [35], [36], [37]. Three well-known CMOS compatible platforms are the doped silica [38], [39], [40], [41], silicon on insulator (SOI) [42], [43] and silicon nitride (Si_3N_4) [44], [21]. The doped silica platform consists of a silica cladding and a silica core doped with germanium to slightly increase its refractive index with respect to the cladding. The SOI has a silicon core and a silica cladding. The silicon nitride platform has a silicon nitride core and a silica cladding. The approximate values of the refractive indices of the three platforms at 1550 nm are displayed in Table 1.1.

Table 1.1. The comparison of three CMOS compatible integration platforms. Numerical values are approximate values at 1550 nm.

	Core refractive index	Cladding refractive index	Loss	Footprint
Doped silica	1.4515	1.444	low	high
SOI	3.48	1.444	high	low
Silicon nitride	1.977	1.444	low	moderate

The doped silica has the lowest loss because of its lowest index contrast as well as the relatively low intrinsic loss in silica. This makes it a proper candidate for low-loss applications. However, the components made of it take up more area because of a limit in bend radius for a specified bend loss, which is due to the low index contrast. The SOI on the other hand, can put up with the tightest bends because of its highest index contrast and hence, requires the lowest footprint, but its loss is the highest as well. In an SOI waveguide, the higher refractive index difference scales up waveguide scattering loss as the high index contrast causes more interaction between a confined mode and the waveguide core boundaries, and thus, loss increases. Moreover, silicon intrinsically has a higher absorption loss than silica and silicon nitride. The silicon nitride platform is between the two other platforms in terms of footprint and loss, although its performance is closer to the doped silica. The loss of silicon nitride is in the same order as that of the doped silica, while its corresponding footprint is between those of the doped silica and SOI.

To gain a better insight into the effect of loss in resolution, the resolution of the SOI is compared to that of the silicon nitride platform. The spectrum of a signal is achieved by taking the Fourier Transform of it when its unlimited time-domain profile is available. In practice, a signal is available for only a limited amount of time, and thus, short-time Fourier transform is used to acquire its spectrum. In this case, the resolution of the obtained spectrum is:

$$\Delta f \cong 1/\Delta t \tag{1.1}$$

where Δt is the duration of the signal. If the signal is sufficiently narrowband, the envelope of the signal traverses at the group velocity $v_g = c/N_g$, where c is light speed in vacuum and N_g is the group index defined as:

$$N_g = N_{eff} - \lambda_0 \frac{dN_{eff}}{d\lambda} \tag{1.2}$$

where λ_0 is the wavelength at which the group index is calculated and N_{eff} is the effective index of the mode. A spectrometer must have a means of storing a signal of duration Δt sufficient to meet the desired resolution. Hence, storing a segment of the signal envelope corresponds to propagation over a path length Δl given by:

$$\Delta l = v_g \Delta t = \left(c/N_g\right)\Delta t \cong \left(c/N_g\right)(1/\Delta f) \tag{1.3}$$

The rough values of the group index for typical single mode SOI and silicon nitride waveguides are 3.5, and 2, respectively. If $\Delta f = 1\ GHz$, the corresponding rough values of Δl are 8.5 cm and 15 cm, respectively. In the case of a ring resonator, the signal must circulate inside the ring without significant loss to traverse the required distance for a resolution of lower than 1 GHz. That is, $\alpha\ \Delta l \ll 1$ needs to be satisfied, where α is loss

(1/cm). This gives the loss for the silicon nitride waveguide as $\alpha \ll 0.07\ (-0.3\ dB/cm)$ and for SOI equal to $\alpha \ll 0.12\ (-0.5\ dB/cm)$. The magnitude of loss for practical silicon nitride waveguides is in the same order as 0.3 dB/cm. However, for the SOI, the typical loss is 2 dB/cm because of the higher intrinsic loss of silicon and extra scattering loss at waveguide walls emanating from the higher index contrast. It is obvious that attaining a resolution of lower than 1 GHz is unlikely with the SOI platform, while silicon nitride at the cost of tolerating some insertion loss may achieve this resolution. In conclusion, as high resolution and low footprint are key in this project, silicon nitride is opted for the spectrometer design.

1.4 Objectives

At this point, silicon nitride is selected as the right integration platform. Moreover, the ring resonator and AWG are chosen as the fine and coarse filter, respectively. The objectives of the thesis are as follows:

1.4.1 Establishing a suitable method to achieve a flat spectrometer response

In a cyclic AWG, the output channel profiles are bell-shaped and not flat. Moreover, the envelope of its channel profiles falls off towards the edges of the band by as much as -3dB. Thereby, the combination of a ring resonator and an AWG may work well as a spectrometer only for the frequency ranges at which the resonant frequencies of the ring resonator are within the -3dB passband of each AWG channel profile. Even within the -3dB passband, the output channels have varied insertion losses depending on their

position within the band, preventing the spectrometer from having a flat frequency response. A technique is required and needs to be established to achieve a flat response in the spectrometer as the band is scanned.

1.4.2 Feasibility evaluation of a silicon nitride ring resonator with a resolution of lower than 1 GHz

For the ring resonator, it is first required to evaluate the feasibility of achieving a resolution of lower than 1 GHz. The resolution in a lossy ring resonator is dependent on total loss including waveguide intrinsic loss, scattering loss, bend loss as well as loss in ring coupler regions. Loss negatively impacts resolution. In such a case, adjusting the cross-coupling power ratio (CCPR) in the ring couplers improves the resolution. Therefore, for a practically used waveguide, bend loss must be calculated, and then the right value for the CCPR needs to be computed. Subsequently, the gap value in the middle of the ring coupler for the corresponding CCPR must be found. Performing these computations is key in the feasibility evaluation of attaining a silicon nitride ring resonator with a resolution of lower than 1 GHz.

1.4.3 Tunability evaluation of the ring resonator over its Free Spectral Range using thermal tuning

The ring resonator must be tunable over one FSR. There are several tuning methods for PIC components. They include thermal tuning [45], piezo-electric tuning [46], electro-optic tuning [47], etc.. Thermal tuning is the most common tuning method, which is performed by a resistive heater that is deposited on top of a waveguide. The heater is

connected to an electrical circuit and the electrical current passing through it heats it up. The generated heat irradiates downward and increases the temperature at the waveguide. As refractive indices are temperature dependent, changing temperature modifies the mode effective index, and as a result, tuning is conducted. It is slower than the other methods but is easier to implement as the tuning can be applied to any waveguide material unlike the other methods that call for specific types of waveguide materials. The thermal tunability of ring resonators with different FSRs are to be assessed to identify the tuning limits of silicon nitride ring resonators. The simulations provide valuable information on the tunability extent, scanning speed, and consumed tuning power of silicon nitride ring resonators.

1.4.4 Feasibility evaluation of an Arrayed Waveguide Grating design to attain a flat on-resonance spectrometer response

An AWG needs to be designed according to the specifications required by the method for a flat on-resonance spectrometer response. First, the AWG design feasibility needs to be examined. Then, the overall performance of the spectrometer encompassing the ring resonator and AWG and applying the above-mentioned technique must be evaluated.

1.5 Contribution to knowledge

The architecture of the spectrometer on silicon nitride platform with a ring resonator as the fine filter and the AWG as the coarse filter together with a method to flatten the on-

resonance response was introduced to scan the C-band with a resolution of lower than 1 GHz.

The incoherent weighted summation method was used to achieve a flat on-resonance frequency response regardless of the position of resonant frequencies. It makes Virtual Channel Profiles (VCP) with the weighted summation of AWG output channel profiles at instantaneous resonant frequencies of the ring resonator and filters out each tunable resonant frequency. Its optical part is simpler than the coherent superposition method while its electrical part does not need handovers between channel profiles. It can achieve a flat unity on-resonance response for any resonant frequency while keeping the crosstalk caused by neighboring resonant frequencies at a sufficiently low level. Also, the effect of nonuniformity of the envelope of AWG channel profiles on the spectrometer response is removed by using this method.

The silicon nitride ring resonator was evaluated to determine its bend radius limit and the feasibility of achieving a resolution of lower than 1 GHz. Also, the design of the ring coupler by using different methods was evaluated. It was noted that a resolution of lower than 1 GHz was attainable for silicon nitride ring resonators at the expense of some insertion loss. Moreover, the super-mode theory combined with the mode effective index simulation results was proved to be the right technique to determine the size of the minimum gap in the ring coupler.

The thermal tunability of silicon nitride ring resonators for different waveguide-heater structures was assessed. The effects of heater material, heater width, and heater distance from the waveguide were examined. The ring resonator FSR limit for tuning by

the amount of one FSR was identified. Furthermore, scanning speed and tuning power values were computed for rings with different waveguides, heaters, and radii.

The use of multiple parallel AWGs was replaced with a consolidated AWG that was designed to have desired overlapping channel profiles. The design of the special AWG proved to be feasible. The wider input waveguide reduces the number of arrayed waveguides and thus, the overall footprint of the AWG. The reduced footprint not only reduces the fabrication cost of the component but also improves the insertion loss as the arrayed waveguides become shorter. By applying the mentioned technique, a flat scanning of the C-band is achieved even though the AWG channel profiles are bell-shaped, and the envelope of the AWG channel profiles is not flat in a cyclic AWG.

1.6 Thesis structure

The structure of the thesis is as follows:

In chapter 2, a novel method to achieve a flat on-resonance response for a spectrometer consisting of a ring resonator as the fine filter with a resolution of lower than 1 GHz and tunable over its FSR, and an AWG as the coarse filter is introduced. The desired requirements for the ring resonator and AWG for the method to work properly are identified.

The evaluation of the ring resonator with the aim of achieving a resolution of lower than 1 GHz is performed in chapter 3. First, the constituent waveguide of the ring resonator is introduced. Then, bend simulations are performed to find out the right range of ring radii. Next, the CCPR is computed for the ring resonator with a resolution of lower

than 1 GHz. Finally, the design of the ring coupler with the aim of determining the gap size in the middle of the ring coupler is carried out.

Chapter 4 is devoted to the tunability assessment of the ring resonator over its FSR. Thermal tuning simulations are carried out for a structure with a resistive heater placed atop the waveguide in the ring area. The resistive heater heats up the ring resonator and thus, the resonant frequency is tuned by changing the mode effective index. The limits of applied electrical tuning power for a safe operation for different waveguide-heater structures are determined. The effects of the waveguide type, heater width and the vertical distance of the heater from the waveguide as well as the heater material on consumed tuning power are also evaluated. Finally, scanning speed for ring resonators with different radii and waveguide-heater structures are calculated. The simulations shed light on the thermal tunability of silicon nitride ring resonators.

The feasibility of designing a special AWG based on the constraints imposed by the method is evaluated in chapter 5. First, design specifications for the AWG are extracted. Next, the AWG is designed and simulated; and finally, the performance of the spectrometer including the ring resonator as the fine filter and AWG as the coarse filter, with the application of the method is assessed by simulation.

The thesis is summarized in chapter 6. It includes a summary of the main findings, original contributions to knowledge, and suggestions for future work.

1.7 Publications

1.7.1 Published and directly related to the thesis

Here is the list of published papers in which the work is directly related to the spectrometer project:

1. Houman Ghorbani, Ramanand Tewari, Mohammad Rad, Eric Bernier, Trevor J. Hall, “Design and Simulation of a Si3N4 Sub-GHz Resolution Integrated Micro-Spectrometer”, *2019 International Conference on Numerical Simulation of Optoelectronic Devices (NUSOD)*, Ottawa, ON, Canada, 2019, pp. 45-46, doi: 10.1109/NUSOD.2019.8806837.

2. Mehedi Hasan, Mohammad Rad, Gazi M. Hasan, Houman Ghorbani, Peng Liu, Patric dumais, Eric Bernier, and Trevor Hall, "Circuit architecture and integration feasibility of a high-resolution broadband on-chip spectral sensor", in *OSA Advanced Photonics Congress (AP) 2020 (IPR, NP, NOMA, Networks, PVLED, PSC, SPPCom, SOF)*, L. Caspani, A. Tauke-Pedretti, F. Leo, and B. Yang, eds., OSA Technical Digest (Optica Publishing Group, 2020), paper SpM3I.1.

3. Gazi M. Hasan, Peng Liu, Mehedi Hasan, Houman Ghorbani, Mohammad Rad, Eric Bernier, and Trevor Hall, "Ring Resonator Gap Determination Design Rule and Parameter Extraction Method for Sub-GHz Resolution Whole C-Band Si_3N_4 Integrated Spectrometer", *Photonics* 2022, *9*, 651. https://doi.org/10.3390/photonics9090651.

4. Mehedi Hasan, Gazi Mahamud Hasan, Houman Ghorbani, Mohammad Rad, Peng Liu, Eric Bernier, and Trevor Hall, "High-resolution Si_3N_4 spectrometer: architecture

& virtual channel synthesis and experimental demonstration," Opt. Express 32, 8697-8714 (2024).

1.7.2 Published and indirectly related to the thesis

As part of background research related to PICs, which enhanced my knowledge and understanding of PIC design, I have contributed to two publications:

1. Weifeng Zhang, Houman Ghorbani, Tong Shao and Jianping Yao, "Mode-Division Multiplexed PAM-4 Signal Transmission in a Silicon Photonic Chip," *2019 International Topical Meeting on Microwave Photonics (MWP)*, Ottawa, ON, Canada, 2019, pp. 1-4, doi: 10.1109/MWP.2019.8892155.

2. Weifeng Zhang, Houman Ghorbani, Tong Shao and Jianping Yao, "On-Chip 4×10 GBaud/s Mode-Division Multiplexed PAM-4 Signal Transmission," in *IEEE Journal of Selected Topics in Quantum Electronics*, vol. 26, no. 2, pp. 1-8, March-April 2020, Art no. 8302308, doi: 10.1109/JSTQE.2020.2964388.

Chapter 2 Method

2.1 Introduction

In this chapter a scheme is proposed to achieve a flat on-resonance spectrometer response. First, the fundamental principles in the spectrometer design are discussed by taking into account the performance requirements. Then, a virtual channel synthesis technique to obtain a flat spectrometer response is explained. The parameters affecting the quality of the spectrometer response are also discussed. Finally, the operational mechanism of the spectrometer is illustrated. The findings of this chapter pave the way for the right simulations to be conducted in the following chapters to assess the feasibility of implementing the spectrometer.

2.2 Fundamental principles

As stated in Chapter 1, the spectrometer needs to be made of photonics integrated circuits (PIC) components and scan the C-band (1530 – 1565 nm) with a resolution of lower than 1 GHz. Silicon Nitride was chosen as the integration platform to achieve low loss performance. The ring resonator was selected as a fine filter to achieve a resolution of lower than 1 GHz, and the arrayed waveguide grating (AWG) was selected as the coarse filter to separate the resonant frequencies of the ring resonator. The reason to have both filters in the spectrometer is the fact that ring resonator has a limit in the maximum free spectral range (FSR) that it can have. The minimum bend radius due to bend loss and the maximum tunable FSR constrain the ring resonator to have an FSR much smaller than the length of the C-band, which is circa 4.4 THz. As such, scanning

the C-band with a ring resonator generates a comb of resonant frequencies that need to be separated. Moreover, the comb generated must be tunable over the FSR of the ring resonator to scan the whole C-band. The separation of the resonant frequencies is done by the coarse filter, which is an AWG in this project. The conventional AWG has multiple outputs, each with a bell-shaped channel profile. To separate the resonant frequencies of the ring resonator, the AWG channel spacing must be at most equal to the FSR of the ring resonator to direct different resonant frequencies to distinct output ports. However, because of the bell-shaped nature of the AWG channel profiles, the insertion loss of the AWG output significantly varies as the frequency is tuned. Fig. 2.1 shows the schematic representation of the AWG output channel profiles and the location of resonant frequencies in black arrows. The black arrows move along the frequency axis as the ring resonator is tuned, experiencing uneven insertion loss. This requires a modification of the AWG to resolve the problem.

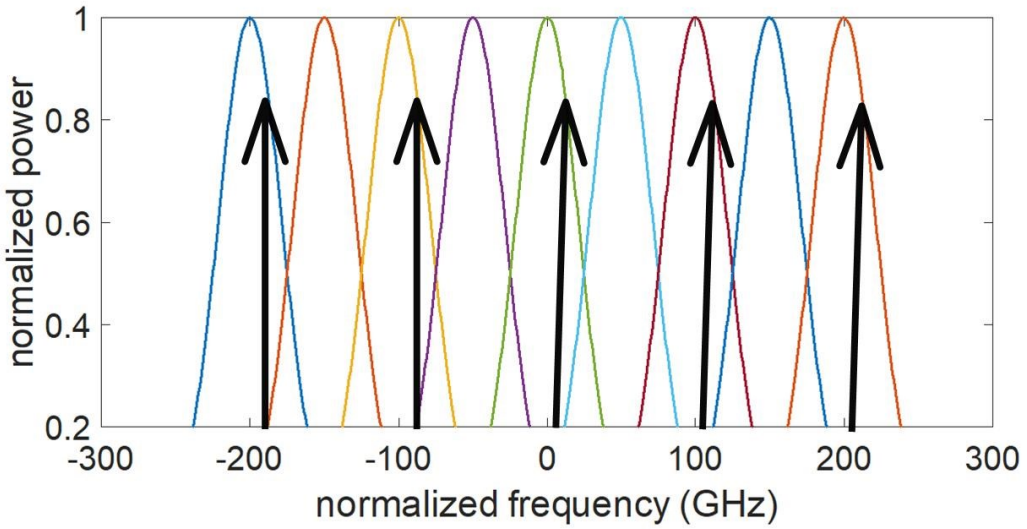

Fig. 2.1. Schematic representation of AWG output channel profiles and the location of resonant frequencies of a ring resonator.

2.3 Method

In this section, first the methods used to overcome the problem of uneven AWG channel profiles are introduced and then, the method applied in the thesis is described.

2.3.1 Arrayed Waveguide Grating thermal or mechanical tuning

Some techniques attempt to tune the AWG output channel profiles. The AWG channel profiles may be shifted over frequency by applying thermal tuning to the arrayed waveguides for the case of the channel spacing being equal to the ring resonator FSR [48], [49]. This is possible but would require a large amount of tuning power to affect the arrayed waveguides especially in silicon nitride platform, which is larger in size than SOI based AWGs, and thus, is inefficient. Mechanical tuning of the AWG input using micro electromechanical systems (MEMS) may also do the same tuning of the WG output channel profiles, which complicates the implementation [50], [51].

2.3.2 Passband flattened Arrayed Waveguide Grating

Other techniques flatten the passband of the AWG channel profile. Authors in [52] modified the shape of the input waveguide into a parabola followed by a multi-mode interferometer (MMI) to attain a flat band with the length of the AWG channel spacing. The response is flattened but does not fully cover the whole channel spacing and has a steep drop at the edges of the passband. It also has ripples in the flat part. The problem of steep drops may be fixed by widening the input structure; however, it will cause overlapping outputs and will require a handover between the outputs. Moreover, the flattened response is only achieved for a limited frequency range in the signal input.

Another technique is modifying the magnitudes and phases of the arrayed waveguides [53]. It is noted that the output far field image is obtained by taking the Fourier transform of the array consisting of the outputs of the arrayed waveguides. This method requires manipulating the arrayed waveguides individually to adjust their amplitude and phases, which might be challenging especially in an AWG with many arrayed waveguides.

2.3.3 Arrayed Waveguide Grating channel superposition

The third way to attain a flat response for a spectrometer encompassing the ring resonator as the fine filter and the AWG as the coarse filter is the superposition of AWG channel profiles. A conventional AWG with identical input and output waveguides — that is, the output center to center distance is minimized for optimum AWG performance while the output waveguide width at the interface is maximized for a maximum channel bandwidth, and the input is identical to the output to minimize the mode mismatch insertion loss— does not have overlapping passband channel profiles. To acquire a flat on-resonance frequency response, optical (coherent) or electrical (incoherent) superposition method may be considered.

2.3.3.1 Coherent (optical) superposition

In the optical superposition method, which has been reported in [54], [55], the ring resonator FSR is equal to the AWG channel spacing and thus, at a certain ring detuning point, each resonant frequency is exiting from corresponding AWG output. The AWG has two inputs that are connected to the output of a synchronous Mach-Zehnder delay interferometer (MZDI) or in the case of a generalized MZDI (GMZDI), the AWG has multiple inputs. Each AWG input creates a distinct set of virtual output channel profiles

that is identical to the ones created by the other inputs expect for being shifted in frequency due to different input waveguide positions. The illumination of the (G)MZDI outputs are arranged versus frequency in a way to keep the AWG output frequency channel profile peaks aligned with the center of respective output ports. Hence, the AWG output channel profiles are formed by a weighted superposition of the virtual channel profiles. The optical superposition method flattens the AWG output channel profiles with the addition of optical components including a (G)MZDI and switch, which increases the design and implementation complexity and overall footprint affecting insertion loss and fabrication cost.

2.3.3.2 Incoherent (electrical) superposition

The electrical (incoherent) superposition of channel profiles is another technique to overcome the problem of uneven AWG channel profiles and is reported in [56], [57]. In this technique, the superposition of AWG channel profiles is performed in the electrical domain at the output of photodetectors. The superposition may be conducted with the unweighted or a weighted summation of overlapping channel profiles.

2.3.3.2.1 Unweighted summation

The unweighted summation of AWG channel profiles is performed by summing the electrical power amounts of AWG outputs. The technique aims at achieving a flat on-resonance response as the resonance frequency of the ring resonator is tuned. To achieve a flat on-resonance response, adjacent AWG channel profiles need to intersect at -3dB lower than their peaks. This design ensures the summation of two adjacent channel profiles achieves a flat frequency response at the peaks and the intersection

point. The summation, however, has, although slightly, lower values elsewhere within the two adjacent peaks. By tuning the ring resonator and using the technique, an almost flat response is achieved at instantaneous resonant frequency points. The superposition of all AWG outputs, however, encompasses the other resonant frequency components as well. Hence, to minimize the effect of other resonant frequencies, only two adjacent overlapping AWG channel profiles must be used in the summation. The selection of the two adjacent channel profiles depends on the position of the resonant frequency with respect to AWG channel profile peaks. A handover of the AWG channel profiles takes place when the resonant frequency is aligned with the peak of an AWG channel profile. Conventional cyclic AWGs have Gaussian-like channel profiles so that adjacent channel profiles intersect at a value that is an order of magnitude lower than their peaks. Therefore, to achieve -3 dB overlapping AWG channel profiles, and to ease the handover process, 2 or more AWGs need to be used. The AWGs must be identical except for one's channel profiles being shifted by the amount of half of its channel spacing. In this case, the parallel combination of two AWGs responses generates overlapping channel profiles that can obtain -3 dB intersection between adjacent channel profiles.

Fig. 2.2 represents the schematic view of the unweighted incoherent summation method using N=2 AWGs. The parallel AWGs are identical except for their output channel profile shifted in frequency by the amount of 1/2 of their channel spacing. If the -3dB bandwidth of each channel profile is 1/2 of the channel spacing of individual AWGs, then the parallel combination forms two interlaced AWGs with overlapping channel profiles that intersect at -3dB.

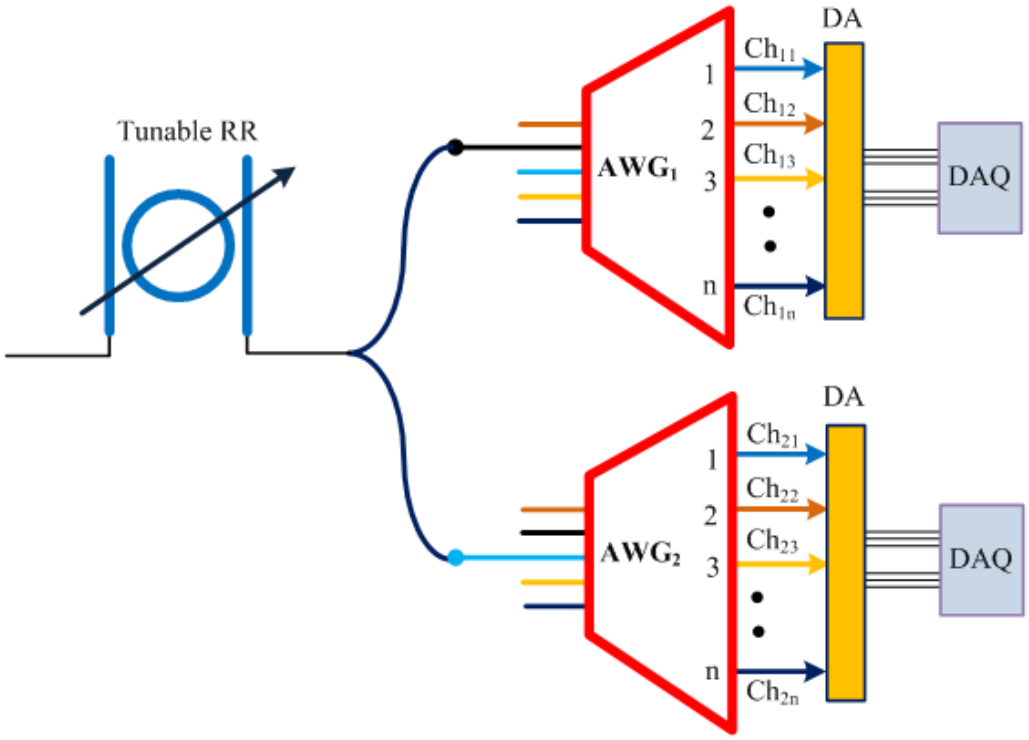

Fig. 2.2. Schematic view of unweighted incoherent summation configuration with 2 AWGs. RR; ring resonator, DA; detector array, DAQ; data acquisition system, Ch; AWG output channel. Adapted from M. Hasan *et al.* [56], licensed under Creative Commons Attribution 4.0 International.

In this case, the ring resonator FSR is equal to each AWG's channel spacing. Therefore, the handovers take place 2 times during the ring resonator tuning over its FSR. The combined AWG channel profiles together with the ring resonator resonant frequencies are illustrated in Fig. 2.3. Dotted channel profiles represent AWG1 while solid ones account for AWG2. The ring resonator has an FSR of 50 GHz, which is the same as each AWG channel spacing. Channel profiles have the -3 dB bandwidths equal to 25 GHz each. This technique still produces ripples in the output power versus ring resonator resonant frequency. Its crosstalk performance is not desirable either. To improve the

crosstalk, the bandwidths of the AWG channel profiles can be reduced; however, it further degrades the flatness of the output power.

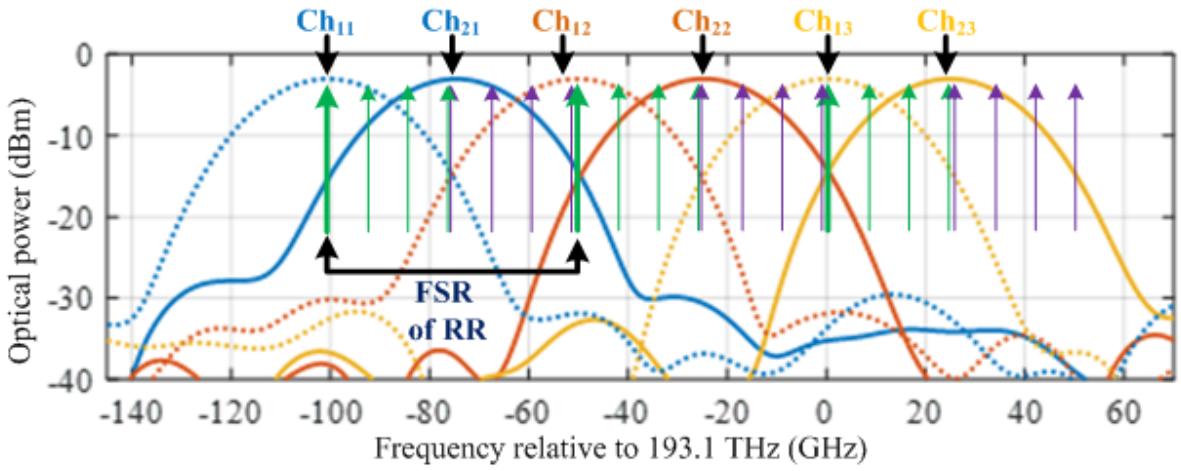

Fig. 2.3. Overlapped channel profiles of two parallel AWGs. Dotted channel profiles represent AWG1 while solid ones account for AWG2. RR; ring resonator, Ch; AWG output channel. Adapted from M. Hasan *et al.* [56], licensed under Creative Commons Attribution 4.0 International.

The resultant output power obtained by the summation of two adjacent channel profiles versus the position of resonant frequency for different -3 dB bandwidths of AWG channel profiles is displayed in Fig. 2.4a. It is seen that for a fixed AWG channel spacing, a lower AWG channel profile bandwidth increases the ripples. An improvement of 8 – 10 dB in crosstalk at the cost of up to 1 dB ripple is achieved.

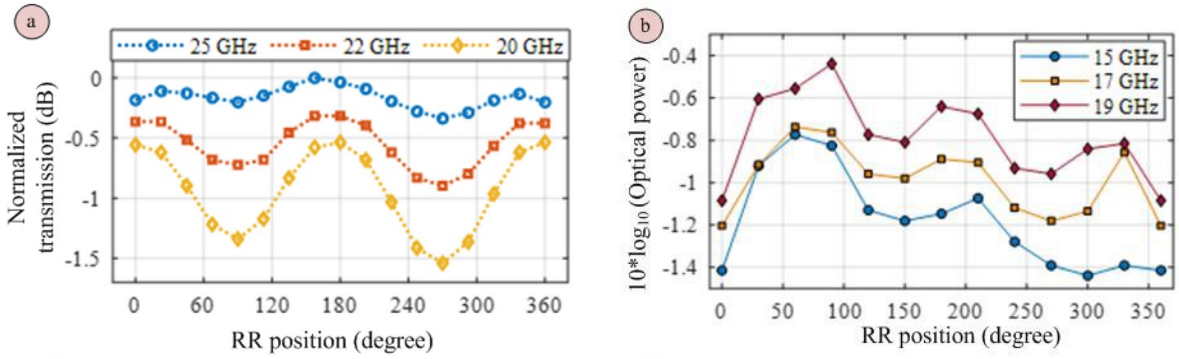

Fig. 2.4. Output power of the unweighted summation of two adjacent AWG channel profiles versus resonant frequency within one ring resonator FSR for different AWG channel profile bandwidths. RR; ring resonator. a) 2 parallel AWG, and b) 3 parallel AWG configurations. Adapted from M. Hasan *et al.* [56], and M. Hasan *et al.* [57], licensed under Creative Commons Attribution 4.0 International, and Optica Open Access Publishing Agreement, respectively.

To further improve the crosstalk, N=3 parallel AWGs may be used. Similar to the previous case, the N=3 parallel AWGs are identical, each with a channel spacing equal to the ring resonator FSR, and -3dB bandwidth equal to 1/3 of the channel spacing. The only difference with the N=2 configuration is that their channel profiles are shifted by 1/3 of the channel spacing with respect to each other. The schematic is shown in Fig. 2.5.

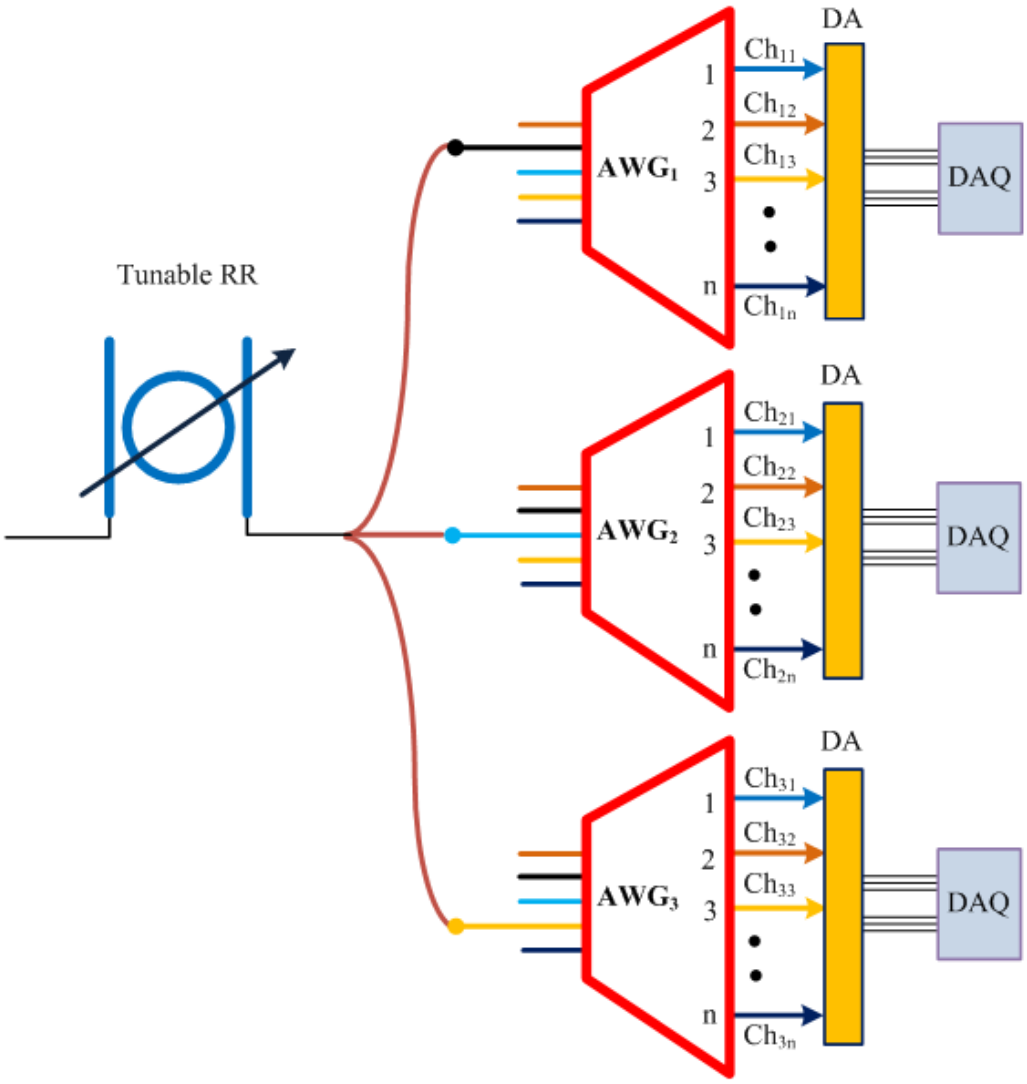

Fig. 2.5. Schematic view of unweighted incoherent summation configuration with 3 AWGs. RR; ring resonator, DA; detector array, DAQ; data acquisition system, Ch; AWG output channel. Adapted from M. Hasan *et al.* [56], licensed under Creative Commons Attribution 4.0 International.

If the -3 dB bandwidth of each channel profile is 1/3 of each AWG's channel spacing, the combined frequency response represents an interlaced set of channel profiles that intersect at -3dB power transmission point as depicted in Fig. 2.6. In this example, the AWG channel spacing and the ring resonator FSR are both 51 GHz, and

each channel profile has a bandwidth of 17 GHz. Dotted channel profiles represent AWG1, solid ones are for AWG2, and dashed ones are for AWG3.

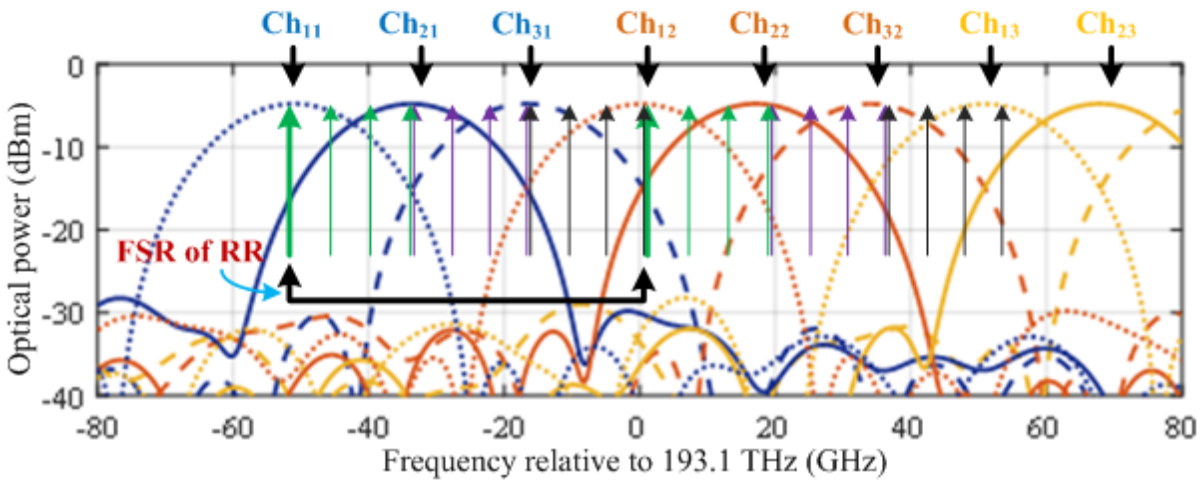

Fig. 2.6. Overlapped channel profiles of three parallel AWGs. Dotted channel profiles represent AWG1, solid ones are for AWG2, and dashed ones are for AWG3. RR; ring resonator, Ch; AWG output channel. Adapted from M. Hasan *et al.* [56], licensed under Creative Commons Attribution 4.0 International.

To form a virtual channel profile for each resonant frequency, two adjacent channel profiles of the interlaced channel profiles (see Fig. 2.6) are used at each resonant point (channel profiles whose peaks are the closest to the resonant frequency). Like N=2, handovers between channels take place when a resonant frequency is aligned with a channel profile peak. Thus, handovers take place 3 times during the ring resonator tuning over its FSR. In this case, adjacent resonant frequencies have much lower amounts in the selected two channel profiles than the case of 2 AWGs, and thereby, crosstalk is improved without having to further compromise the flatness of the frequency response. However, the extra AWG adds to the required footprint and the complexity of the splitter. The summation of two adjacent AWG channel profiles versus resonant frequency in the

N=3 AWG configuration for 3 different AWG channel profile bandwidths is shown in Fig. 2.4b. The ring resonator and AWG channel spacing are both 51 GHz. It is noted that the performance for the AWG bandwidth of 17 GHz is better than the other two cases in terms of ripples, which is due to their intersection with adjacent channel profiles at -3 dB lower than the peaks.

2.3.3.2.2 Weighted summation

The weighted summation of all channel profiles is the technique used in this thesis, which is also described in [57]. In the proposed method, a virtual channel profile (VCP) is synthesized for each resonant frequency that enters the AWG. The VCP is made by a normalized weighted summation of each output of the dispersive device. The weights are real numbers between 0 and 1, and their magnitudes are proportional to the frequency distance between the respective resonant frequency and the peak of each channel profile. The passband of each AWG channel profile may be approximated by a Gaussian profile whose peak is the same as the channel profile peak and its full width at half maximum (FWHM) is equal to the -3 dB bandwidth of the channel profile. Each weight then is set to be the magnitude of the respective Gaussian profile at the position of the resonant frequency for which the VCP is made. Fig. 2.7 illustrates the schematic view of a Gaussian profile and a resonant frequency that is distanced by the amount of Δf from the peak. It is noted that the weight becomes closer to its maximum as the resonant frequency is placed closer to the peak and vice versa. As a result, the channel profiles whose peaks are closer to the resonant frequency have larger weights and thus, are more important in the formation of the VCP. Each resonant frequency that enters the AWG (see Fig. 2.1),

requires a VCP to be filtered out. Therefore, if the number of channel profiles is *M*, then at each detuning stage, *M* weights are generated for each resonant frequency.

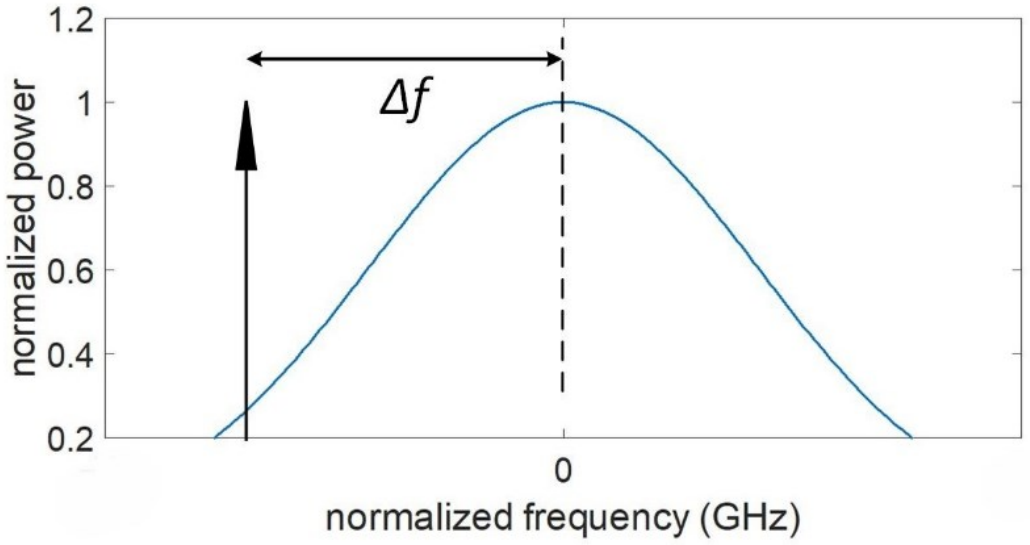

Fig. 2.7. Schematic representation of a Gaussian profile and resonant frequency.

The ring resonator detuning point is informed to the processing unit through a wavelength meter [58] that reads out the resonant frequencies of the ring resonator instantaneously, and subsequently a unique set of weights are made for each resonant frequency for the respective detuning point. Once the weights are generated, the VCP for each resonant frequency is made as a normalized weighted summation of all channel profiles as:

$$VCP_j(f) = \sum_{i=1}^{M} w_{ij} H_i(f) \,/\, \sum_{i=1}^{M} {w_{ij}}^2 \tag{2.1}$$

where j, M, w_{ij}, and $H_i(f)$ are the j^{th} resonant frequency, the number of channel profiles, the weight corresponding to j^{th} resonant frequency and i^{th} channel profile, and i^{th} channel profile, respectively. The goal is to achieve a flat response at the resonant frequency. Thus, the VCP needs to remain constant at the resonant frequency for which

it is formed as the resonant frequency is tuned. To evaluate the VCP value at the resonant frequency, two cases for the position of the resonant frequency are considered:

A) the case of Δf = 0

When Δf = 0, the resonant frequency is aligned with the peak of a channel profile (see Fig. 2.7). If the background noise as well as the other channel profiles at this resonant frequency are at least an order of magnitude lower than the primary channel profile, then in relation (2.1), the other terms are negligible compared to the one corresponding to the primary channel profile, and the VCP becomes:

$$VCP_j(\Delta f = 0) = w_{1j}H_1(0)/w_{1j}^2 = 1. \quad (2.2)$$

In (2.2), $H_1(0)$ and w_{1j} are the magnitude and corresponding weight of a channel profile at its peak, respectively, and are both equal to unity and thus, the VCP becomes unity.

B) the case of 0 < Δf < Δf_0

In this case, Δf_0 is defined as channel spacing, and the resonant frequency may be anywhere between two adjacent channel profiles. With the constraints applied in case A, stating that at the peak of a certain channel profile the magnitudes of the other channel profiles are well below it, it is understood that for 0 < Δf < Δf_0, only the two channel profiles at either side of the resonant frequency can have noticeable values. Hence, (2.1) may be simplified to:

$$VCP_j(f) = [w_{1j}H_1(f) + w_{2j}H_2(f)]/[w_{1j}^2 + w_{2j}^2]. \quad (2.3)$$

Relation (2.3) is unity provided the intersection point between the two channel profiles is at least an order of magnitude above noise level.

Therefore, to obtain the flat unity VCP for all frequencies, both conditions in A and B need to be fulfilled, that is,

- At the peak frequency of a certain channel profile, the peak value must be at least an order of magnitude above the magnitude of the other channel profiles and noise level, and
- The intersection points of the adjacent channel profiles must be at least an order of magnitude above noise level.

At this point, the only remaining thing is the evaluation of the crosstalk caused by adjacent resonant frequencies as according to (2.1) all channels are included in the formation of a VCP; hence, the other resonant frequencies are present in the VCP, and their effects must be mitigated. As stated, for a certain resonant frequency, the channel on either side of it are the closest channels and thus, have the largest weights. The weights of channels become smaller as their peaks are placed farther from the primary resonant frequency. Hence, the adjacent resonant frequencies must be placed as far as possible from the primary resonant frequency so that the weights of the channels in which the adjacent resonant frequencies are sizable, are small enough and do not cause significant crosstalk. In other words, the ring resonator FSR must be as large as possible. To better realize the effect of ring resonator FSR on crosstalk, a VCP is created for channel profiles that are spaced by the amount of 25 GHz and intersect at -3dB. The primary resonant frequency is aligned with a channel profile peak. Two rings with FSRs

of 30 GHz and 50 GHz are considered. The VCP as well as the combined ring resonator and virtual channel responses are shown in Fig. 2.8. It is noted that a larger FSR significantly improves crosstalk.

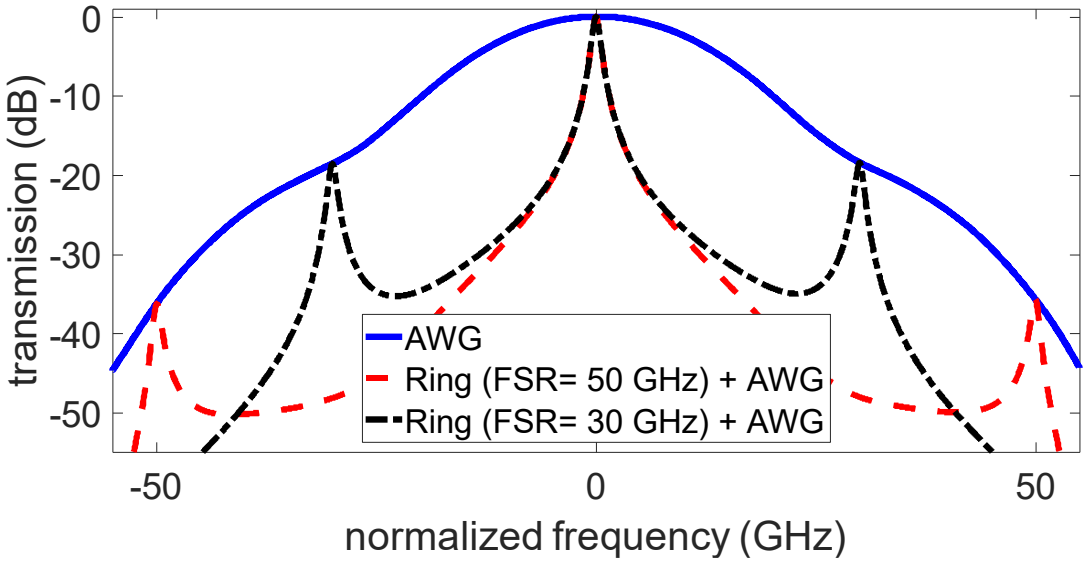

Fig. 2.8. An example of VCP and the effect of ring resonator FSR on crosstalk.

It is noted from Fig. 2.8 that a designer must maximize the FSR of the ring resonator for better crosstalk performance. However, the maximum achievable tunable ring resonator FSR is limited. Therefore, adjustments must be made in the design of channel profiles for a specified ring resonator FSR to obtain desired crosstalk. For the case of a fixed amount of ring resonator FSR, two approaches may be taken to improve crosstalk.

- Keeping transmission at the intersection points of channel profiles unchanged and reducing channel spacing, or
- Keeping channel spacing unchanged and reducing transmission at channel profile intersection points.

Both methods lower the -3dB bandwidth of channels and the weights of channel profiles at a certain distance from the primary resonant frequency is scaled down, resulting in improved crosstalk. Reducing channel spacing increases the susceptibility of AWG channel profiles to the arrayed waveguides phase error [59], which is caused by fabrication imperfection; thus, degrading phase error crosstalk. Thereby, the first method although improves neighboring resonant frequency crosstalk, it has a negative effect on phase error crosstalk. On the other hand, the second method keeps the channel spacing unchanged, but reduces the transmission amount at the intersection points, which reduces the distance between the intersection points and noise level, again increasing the susceptibility of AWG channel profiles to the arrayed waveguides phase error, which increases background noise level. Hence, both methods have pros and cons, and neither is preferred to the other. Fig. 2.9 demonstrates the effect of reduced channel spacing on improving the crosstalk emanating from neighboring resonant frequencies. In this example, the ring resonator FSR is fixed to 150 GHz, and the VCP is formed for two cases. In the first case, the channel spacing is 50 GHz, while in the second case it is 75 GHz. In both cases, adjacent channel profiles intersect at -3dB, which fulfills the design requirements. As a result, unity transmission is attained at the primary resonant frequency (in this case f=0). The AWG with reduced channel spacing has significantly improved crosstalk.

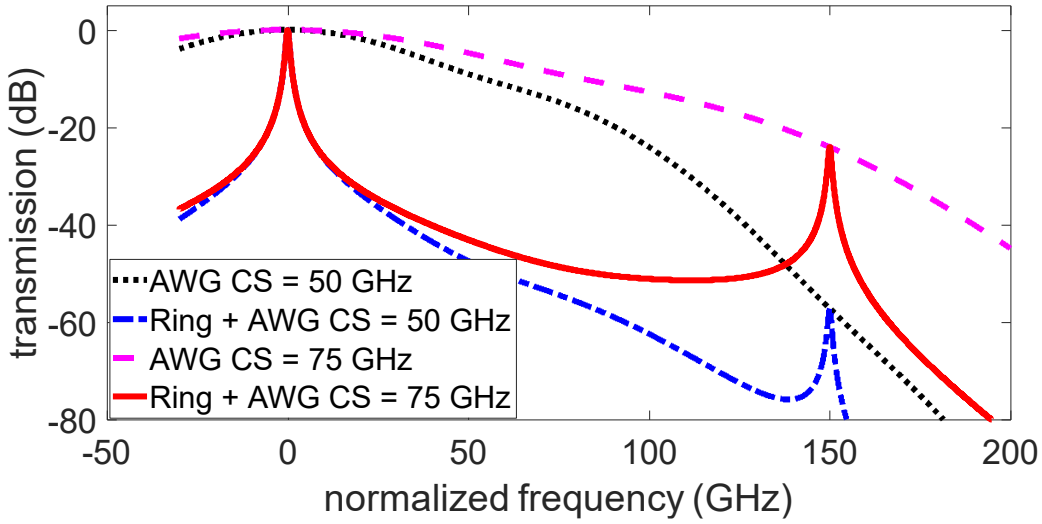

Fig. 2.9. The effect of AWG channel spacing (CS) on the crosstalk caused by neighboring resonant frequency.

The incoherent weighted summation method achieves unity response for any VCP for any primary resonant frequency provided the design constraints are respected. Its optical architecture is much simpler than the one for coherent superposition method and unlike unweighted summation method, can achieve a unity on-resonance response as frequency is tuned by the ring resonator. Moreover, handovers between channels are not required as every channel has a weight, and it makes the electrical part simpler to implement. Furthermore, the intersection points between adjacent channel profiles do not need to be at -3dB necessarily, which is another design flexibility. Also, in the absence of a need for channel handover, the ring resonator FSR is not required to be an integer multiple of channel spacing. Another advantage of this method is that although the envelope of the channel profiles of a cyclic AWG has nonuniformity, because of the normalized weighted summation, a flat unity on-resonance frequency response can be achieved at any frequency point over the band. In general, the incoherent weighted

summation method is simpler in architecture in optical and electrical domains and enjoys fewer design restrictions while achieving a better performance.

To compare the performances of the unweighted and weighted summation methods, an experiment was conducted by other members in our research team. In the experiment, a tunable ring resonator with an FSR of 50 GHz was connected to two parallel AWGs each a channel spacing of 50 GHz and -3 dB bandwidth of 20 GHz. The input ports of the AWGs are different so that the combined AWGs' frequency response are interlaced channel profiles, separated by 25 GHz. The schematic view of the implemented circuit is illustrated in Fig. 2.10.

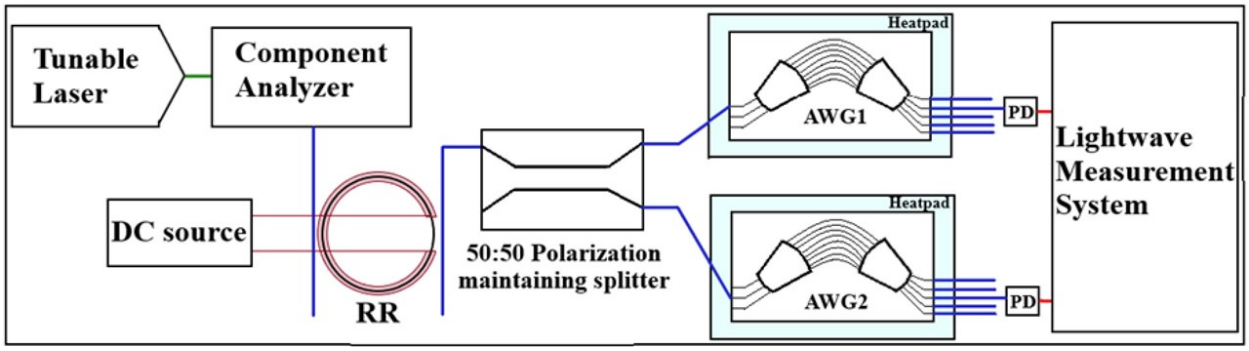

Fig. 2.10. Schematic view of the experimental setup with two parallel AWGs. RR; ring resonator, PD; photo detector. Adapted from M. Hasan *et al.* [57], licensed under Optica Open Access Publishing Agreement.

Both the unweighted and weighted summation techniques are applied to calculate the output power of the spectrometer versus the resonant frequency of the ring resonator. The comparison of the results achieved is shown in Fig. 2.11. The rectangular weighting method stated in the figure is the same as the unweighted summation method except that each of the two AWG channel profiles that are used between two successive hand-overs,

is multiplied by its own distinct constant coefficient to attain a flatter response. The Gaussian weight refers to the weighted summation method.

It is seen that the weighted (Gaussian) summation technique has a flatter response as expected. The ripples in the weighted method are due to the interlaced AWG channel profiles not being spaced evenly while the weighted are generated for evenly spaced channel profiles. The uneven arrangement of the interlaced channel profiles is due to the imperfect thermal trimming of the AWGs that is performed by placing a hot plate under the AWG. Moreover, no wavelength meter is used in the formation of the synthesized output power profile, and thus, the generated weights are not accurate.

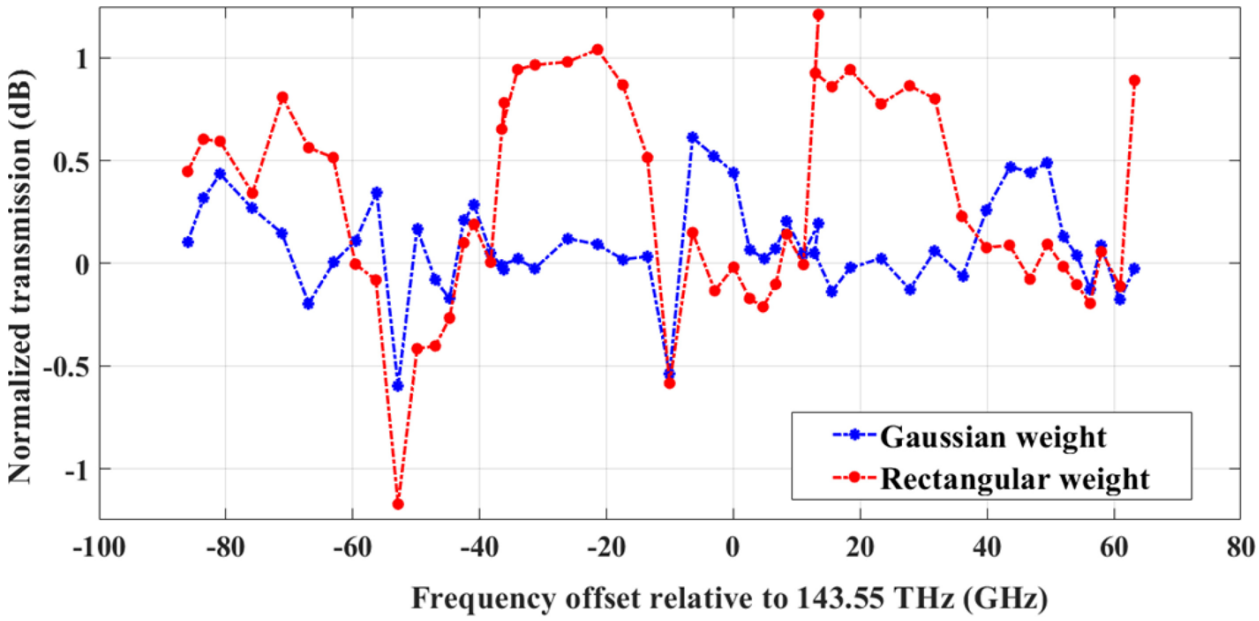

Fig. 2.11. Comparison of the synthesized output power versus the resonant frequency of the ring resonator using Gaussian (weighted summation) and Rectangular (modified unweighted summation) methods. Adapted from M. Hasan *et al.* [57], licensed under Optica Open Access Publishing Agreement.

Even though multiple AWGs may be used in parallel to achieve overlapping channel profiles with interleaved channels, the parallel AWGs can be consolidated into just one AWG. This is demonstrated in Chapter 5. This innovation further reduces optical implementation complication, insertion loss, chip footprint, fabrication cost, and the mentioned measurement trimming issues of the parallel AWGs. Once the maximum achievable tunable ring resonator FSR is determined in Chapter 3 and 4, the design of the special AWG can be conducted accordingly.

2.4 Spectrometer architecture

With the incoherent weighted summation technique, and the consolidation of multiple parallel AWGs into one, the architecture of the spectrometer consists of a ring resonator with a resolution of lower than 1 GHz that is tunable over its FSR, a specially designed AWG to possess passband overlapping channel profiles that intersect at desired transmission level, a wavelength meter, and the processing unit. The schematic of the proposed spectrometer is shown in Fig. 2.12.

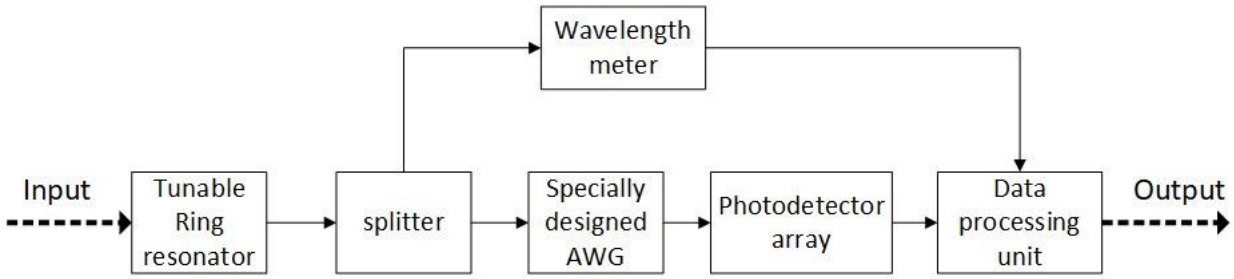

Fig. 2.12. Schematic view of the spectrometer

Light is first fed into the ring resonator. The ring resonator generates a comb of resonant frequencies at its drop port. The comb elements are spaced by the amount of

the ring resonator FSR, where each comb element has a bandwidth of lower than 1 GHz. Tuning the ring resonator for one resonant frequency over the FSR shifts all resonant frequencies by the amount of one FSR and thus scans the whole band. A splitter (for example 99% - 1% power division) splits the output comb of the ring resonator into two parts. The larger part is then fed into the AWG and ultimately, the photodetector array outputs are fed into the processing unit. The smaller output of the splitter enters the wavelength meter. At any tuning moment, instantaneous resonant frequencies are read out by the wavelength meter and informed to the processing unit to generate the right instantaneous set of weights for each instantaneous resonant frequency. Once the weights are generated, corresponding VCPs are formed to filter out each resonant frequency. By tuning the ring resonator over its FSR with a certain scanning speed, the whole C-band is scanned with a resolution of lower than 1 GHz.

2.5 Summary of the main findings

First, fundamental principles in the spectrometer design consisting of the need for ring resonator with a resolution of lower than 1 GHz and tunable over its FSR, an AWG to separate the resonances of the fine filter, and the need for a method to achieve a flat on-resonance response when scanning the C-band are clarified. Next, different techniques that have been used to achieve flat scanning are introduced and subsequently, the method used in this work is elucidated. The method is called incoherent weighted summation, which makes a flat on-resonance response to scan the C-band by the superposition of interlaced AWG channel profiles in the electrical domain. Then, the

proposed spectrometer architecture is described by introducing its constituent components and explaining its scanning mechanism.

Chapter 3 Ring Resonator Resolution

3.1 Introduction

This chapter is devoted to the analysis of the silicon nitride ring resonator to evaluate the feasibility of achieving a ring resonator with a resolution of lower than 1 GHz. The chapter starts with introducing the ring resonator and its related theory to obtain insight into the design of the ring resonator with a resolution of lower than 1 GHz. Next, the constituent waveguide in the ring resonator is introduced. In the following, simulation results to identify the bend loss, and required cross-coupling power ratio in the ring coupler are illustrated. Then, the method to determine the minimum gap size in the ring coupler for a specified cross-coupling power ratio is demonstrated and finally, the minimum gap size for a ring resonator with a resolution of lower than 1 GHz is obtained.

3.2 Theory

The ring resonator is one of the photonics integrated circuits (PIC) components that is used in filtering an spectrum at its resonant frequencies [60], [61], [62], [63], [64], [65], [66]. There are two types of ring resonators with the first being named as the all-pass ring resonator, and the second as the add-drop ring resonator.

The all-pass ring resonator consists of a ring that is placed adjacent to a straight waveguide as shown in Fig. 3.1(a). Light enters from the input port and is partially coupled into the ring. At certain frequencies, the phase shift that light gains in one complete trip in the ring is an integer multiple of 2π. In this case, the light that has traversed in the ring becomes in-phase with the new light that is just coupled into the ring from the waveguide,

increasing its magnitude. The phenomenon is called resonance and the frequency at which it takes place is the resonant frequency as illustrated in equation (3.1):

$$\lambda_{res} = \frac{N_{eff} L}{m}, \qquad m = 1,2,3, \ldots \tag{3.1}$$

where $\lambda_{res} = c/f_{res}$ and is resonant wavelength, c is light speed in vacuum, m is a positive integer, L is ring circumference, and N_{eff} is the effective index of a mode that causes resonance. It is noted that there are numerous resonances for a certain ring, each corresponding to a specific value of m. The interval between the resonances is called the free spectral range (FSR):

$$FSR = \frac{\lambda^2}{N_g L} \tag{3.2}$$

in which, λ is the wavelength around which FSR is computed, and N_g is the group index. The group index corresponds to the velocity of a group of frequencies that are studied (in this case, the frequencies within one FSR), and is defined as:

$$N_g = N_{eff} - \lambda_0 \frac{dN_{eff}}{d\lambda} \tag{3.3}$$

where λ_0 is the wavelength at which the group index is calculated. The all-pass ring resonator filters out the resonant frequency and passes the rest of the spectrum by making a notch in its output frequency response.

Fig. 3.1(b) shows the add-drop ring resonator, which has two waveguides. Light enters from the input port and exits at the through-port at non-resonant frequencies. At

resonant frequencies, however, light exits from the drop port and a notch appears at the through-port. Hence, resonance frequencies are separated from input spectrum. Similarly, light entering from the add port at resonant frequencies exits from the through-port. The power transmission of an add-drop ring resonator is expressed in [62] as:

$$T_d = \frac{(1 - r_1^2)(1 - r_2^2)a}{1 - 2r_1 r_2 \operatorname{acos}(\varphi) + (r_1 r_2 a)^2} \tag{3.4}$$

where $\varphi = N_{eff} L \frac{2\pi}{\lambda}$, r_1 and r_2 are amplitude self-coupling ratios (e.g. from input to pass) in the first and second ring coupler regions, respectively, and a is single-pass amplitude transmission (the amplitude transmission of light for one complete trip inside the ring), and is related to power attenuation coefficient α (1/cm) by:

$$a^2 = e^{-\alpha L} \tag{3.5}$$

The coefficient α takes in all losses in a single-pass trip including absorption loss, scattering loss, bend loss and loss in the ring couplers. It is noted that at resonance, φ becomes an integer multiple of 2π and for a lossless ring ($a = 1$), and identical couplers transmission at drop port becomes unity. In a lossy ring resonator, $a < 1$, and the drop port experiences insertion loss.

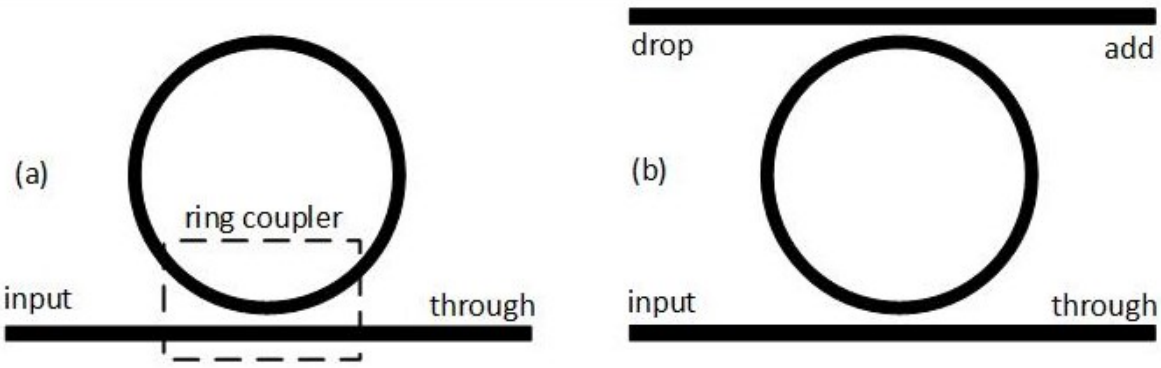

Fig. 3.1. a) all-pass, b) add-drop ring resonator.

The full wave at half maximum (FWHM) of frequency response, which is also called -3dB bandwidth or resolution is computed in [62] using relation (3.4) as:

$$FWHM = \frac{(1 - r_1 r_2 a)\lambda_{res}^2}{\pi N_g L \sqrt{r_1 r_2 a}}. \tag{3.6}$$

Relation (3.6) indicates that the resolution can be minimized when the parameter $r_1 r_2 a$ tends to unity. Thus, reducing loss and outcoupling from the ring scales down resolution.

The goal of this chapter is to examine the possibility of designing a ring resonator with the FSR of at least 50 GHz and the resolution of lower than 1 GHz at the C-band. The quality factor (Q) of a resonator is defined as the ratio of its resonant frequency to its resolution. The finesse of a resonator is the ratio of its FSR over its resolution. Hence, the requirement of this study is to achieve a Q of 200,000 and a finesse of at least 50. There has been significant work on high-Q resonators. WGM resonators have achieved ultra-high Q performances. However, they are mounted structures and are not considered as integrated circuit components [9], [67], [68]. Higher order ring resonators can achieve high-Q performances, but their multi-ring nature complicates the design and increases

their vulnerability to fabrication imperfection [69], [70]. Micro-disks and micro-donuts that generally enlarge the waveguide cross-section inside the resonator have also been used for high-Q applications. Nevertheless, the generation of higher order modes in the resonator consumes part of the optical power, increasing the loss. Also, the generated higher order modes degrade the crosstalk [71], [72], [73], [74], [75], [76], [77], [78]. Other authors have reported high-Q ring resonators, but the low loss (high-Q) performance attained at the cost of lower than 50 GHz FSRs [79], [80]. In the following the low loss waveguide used in this work is first introduced and characterized, and then, ring resonator response simulation is carried out.

3.3 Waveguide

The waveguide structure used for the ring resonator has a core consisting of two separate silicon nitride strips with a lower layer thickness of 75 nm and an upper layer thickness of 175 nm separated by a 100 nm thick silica layer. The width of the top side of the upper strip is 1100 nm with a sidewall etching angle of 82 degrees with respect to the horizontal axis for the whole structure. These dimensions ensure a single mode operation in the C-band. It is introduced by industry and is referred to as the Asymmetric Double Strip (ADS) waveguide [81], [82]. The double layer nature of the waveguide is to overcome the fracture issue in thick silicon nitride layers caused by mechanical stress. With a double layer waveguide, not only is the stress issue resolved, but also the effective index of the mode scales up. This makes the waveguide more tolerant to tighter bends than a single layer structure with similar thicknesses of each layer. Another advantage of this waveguide is that at the chip ends where fiber coupling is required, the upper layer

may be tapered down to zero thickness, leaving only the lower layer. This action makes the waveguide mode spread much more in the cladding and thus, fiber coupling is conducted with less mode mismatch loss. The guaranteed maximum intrinsic loss by the manufacturer for the straight waveguide is 0.5 dB/cm. The cross-section of the waveguide together with the fundamental TE mode at 1550 nm is presented in Fig. 3.2. Photon Design's FIMMWAVE tool was used to simulate the structure. The simulations were done by applying the finite difference method (FDM). Non-uniform horizontal and vertical meshes were used and increased in multiple simulations until the results converged. The fabrication process variation (FPV) for the waveguide was stated to be ±200 nm using contact lithography, which means a fabricated waveguide may be wider or narrower than the desired width by up to 200 nm.

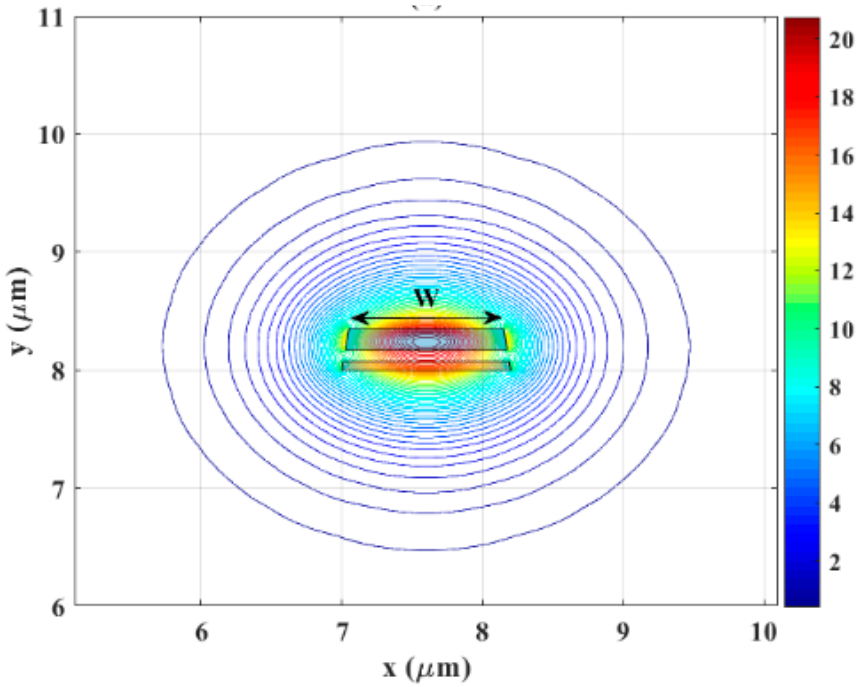

Fig. 3.2. The cross section of the ADS waveguide illuminated by the fundamental TE mode at 1550 nm. Adapted from G. M. Hasan *et al.* [83], licensed under Creative Commons Attribution 4.0 International.

The effective index and group index of the waveguide versus the width of the upper strip's top side for the three lowest modes at 1550 nm are demonstrated in Fig. 3.3. It is noted that at 1100 nm and even with 200 nm extra width due to fabrication process variation error, the waveguide remains in the single mode regime.

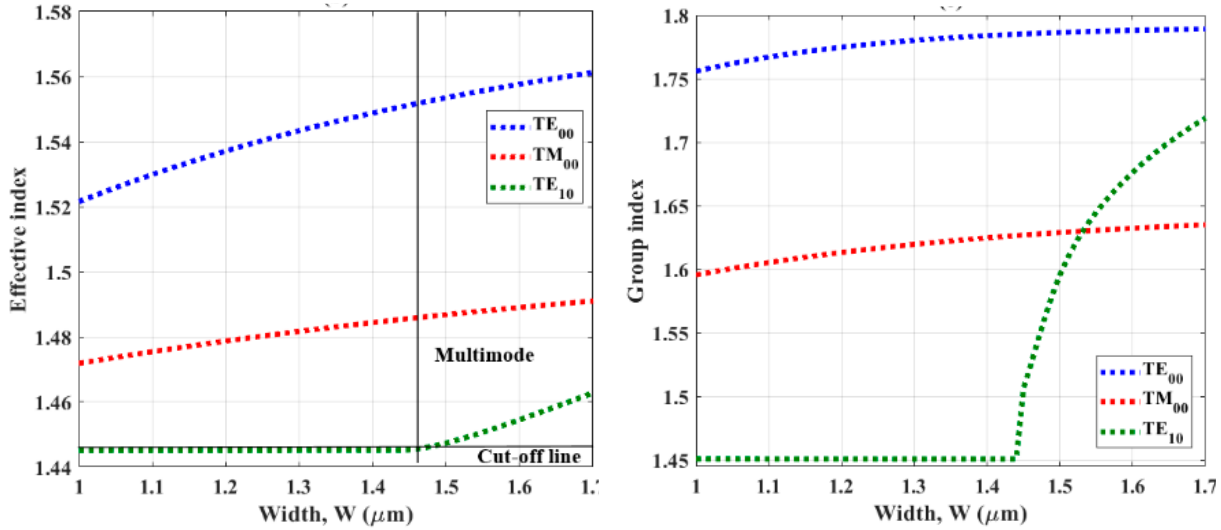

(a) (b)

Fig. 3.3. a) Effective and group index characterization of the ADS waveguide at 1550 nm for the three lowest modes versus the length of the top side of its upper strip. Adapted from G. M. Hasan *et al.* [83], licensed under Creative Commons Attribution 4.0 International.

3.4 Ring resonator simulations

In this section the evaluation of the possibility of attaining an add-drop ring resonator to filter out light with a resolution of lower than 1 GHz over the C-band (1530 – 1565 nm) using the introduced waveguide is carried out. In the first step, bend loss needs to be computed to determine the right value for the ring radius and FSR. Bend simulations are performed using Photon Design's FIMMWAVE tool for TE polarization because of its better robustness in putting up with tighter bends compared to TM polarization.

Maintaining a bound mode for a certain bend radius becomes challenging when a waveguide is narrower, and the wavelength is larger. As such, bend simulations are performed for the waveguide whose width is 200 nm lower than the standard value of 1100 nm and at the largest wavelength in the C-band (1565 nm). Such simulation results are reliable for a wider waveguide and a lower wavelength, too. The numerical method used in the bend simulations was FDM. Three walls of the simulation cross-section had perfect electrical conductor (PEC) boundary conditions (where no outward radiation is expected), but the 4^{th} wall where power moves away from the waveguide (causing bend loss) had an absorption layer boundary condition before the PEC wall. The role of the absorption layer is to attenuate the radiating light and prevent it from reflecting into the waveguide core. The thickness of the absorption layer is determined by multiple simulations for a certain waveguide structure until the results converge. In our case, its thickness was computed to be 1 μm. Fig. 3.4 depicts the bend loss versus ring radius for TE polarization for the ADS waveguide with a width of 200 nm lower than the standard waveguide at the wavelength of 1565 nm. The radius is defined as the distance between the center of the ring and the middle of the waveguide. It is noted that for radii equal to or larger than 180 μm, the bend loss is an order of magnitude less than the intrinsic waveguide loss. Hence, a radius equal to or larger than 180 μm does not negatively affect the resolution and thus, the value of a remains constant in (3.6). Therefore, tuning the outcoupling values r_1 and r_2 adjusts the resolution. It should be noted that other than intrinsic and bend loss, the loss in the transition from the pure ring to the ring coupler, which occurs because of a mismatch between the straight and bend modes, and the loss caused during a cross-coupling in the ring coupler because of different propagation

constants of the straight and bend waveguides, also affect parameter a. Unfortunately, it was not possible to simulate the ring coupler for the purpose of loss evaluation because of technical difficulties in the simulation, which are elaborated later in the chapter. Therefore, it is expected that a will have a lower value in practice than the one used in this simulation. Nonetheless, adjusting r_1 and r_2 can still compensate for a and maintain a resolution of lower than 1 GHz.

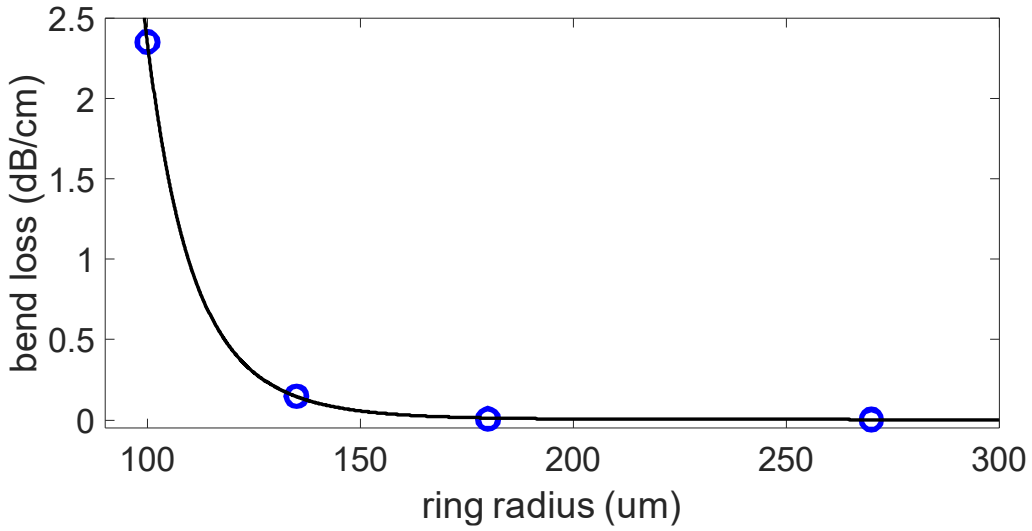

Fig. 3.4. Bend loss versus ring radius for the ADS waveguide with a width of 200 nm lower than the standard waveguide at the wavelength of 1565 nm. Markers show data points, and the solid line is the fitted curve.

The add drop ring resonator in this design has identical ring couplers so $r_1 = r_2$. Resolutions were computed using MATLAB for rings whose radii are 180 and 540 μm, corresponding to FSRs of 150, and 50 GHz, respectively. In both cases, the bend loss is negligible compared to the intrinsic waveguide loss. Using (3.4), (3.5), and (3.6), computed cross-coupling power ratio (CCPR) values for the ring resonators with the resolutions of lower than 1 GHz and the FSRs of 50 and 150 GHz are 4% and 1.35%, respectively. The MATLAB code is provided in Appendix B. Fig. 3.5 displays the frequency

responses of the two ring resonators at the drop port using (3.4) and performed in MATLAB. The insertion loss values at the resonant wavelengths for both rings are the same and equal to -3.4dB. The length difference between the two peripheries has a negligible effect on the single pass transmission (a), resulting in similar insertion loss amounts. The extinction ratio (ER), which is the difference between the maximum and minimum values of power transmission over an FSR, is higher for the ring with larger FSR. It is due to the lower amount of cross-coupling into the ring in non-resonant frequencies; and thus, less power exits through the drop port. The quality factor values for both cases are 200,000 while the finesse values for the rings with the FSRs of 50 GHz, and 150 GHz are 50, and 150, respectively.

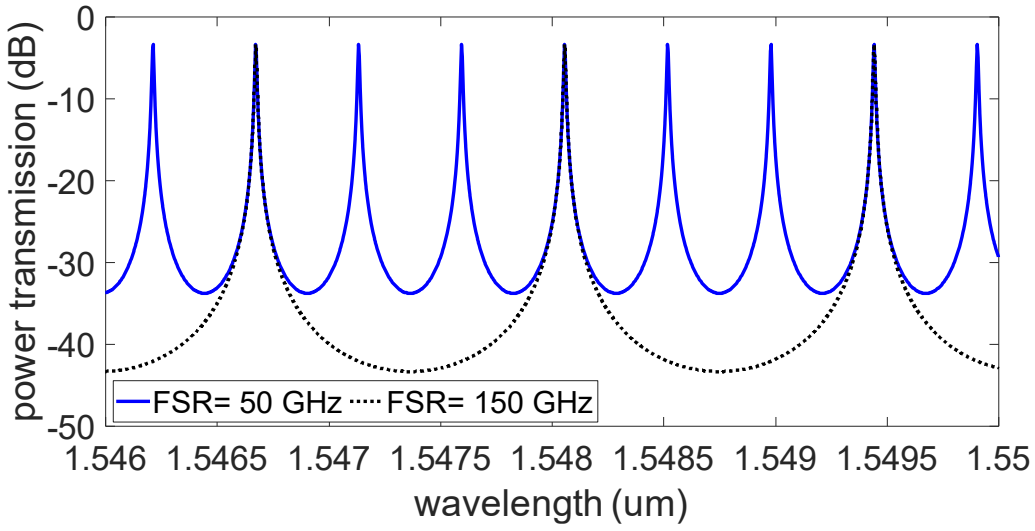

Fig. 3.5. Frequency responses of the ring resonators at their drop ports with a resolution of lower than 1 GHz for two FSR values of 50 GHz, and 150 GHz.

3.5 Ring coupler design

Once the values of CCPR in the ring couplers (see Fig. 3.1(a)) are determined, the ring coupler needs to be designed to find the minimum gap size between the ring and straight waveguide for desired CCPRs.

There are several methods that may be considered for the study of a ring coupler structure. The Coupled Mode Theory (CMT) is a basic theoretical method for analyzing couplers [59], [84], which may be used as a rough initial estimation; however, as it assumes orthogonality between the modes of the two waveguides (which is not the case), and some simplifications in the formulae, it cannot be considered precise.

A second option is applying the beam propagation method (BPM) [85], [86]. Although effective for low index contrast structures, it does not achieve rigorous results where reflections take place in a structure. The silicon nitride ring coupler has sharp angles, and the platform is relatively high index contrast; thus, the BPM is inefficient.

Another method is to perform 3D FDTD [87], [88] simulations. It is accurate but only effective for a structure that the number of generated meshes are small enough for the simulation to take reasonable time; otherwise, the resultant massive computational burden renders the simulation very slow and inefficient.

The next option is 2.5D FDTD [89], which is an intermediate technique that collapses the 3D structure into a 2D one — e.g. replacing the 3D ring coupler with the 2D surface shown in Fig. 3.1(a). It first computes the effective index of the fundamental 1D slab mode in the 3rd dimension and then performs a 2D FDTD simulation for the 2D

structure, separately. Finally, the two results are combined. The method is useful for planar components in which the vertical slab does not change in dimensions, and also for a structure that only the lowest vertical slab mode for a certain polarization is excited with no significant coupling between vertical modes. It is much faster than 3D FDTD but is not as rigorous; because it ignores the inherent nature of a 3D structure where vertical coupling can take place between electromagnetic modes.

Yet another method is the Eigen-mode expansion (EME) method [90], [91], which uses several Eigen-modes in the cross-section — normal to the direction of wave propagation — of a structure to constitute the real existing mode profile by adding up the weighted Eigen-modes. The EME method works reliably for a structure without sharp angles. However, sharp angles in a structure require a huge number of Eigen-modes, and thus, may result in failure. The silicon nitride ring coupler due to having waveguides with lower index contrast than the ones in platforms like silicon-on-insulator (SOI), requires a larger distance between the ring and straight waveguide for the coupling to be considered negligible. Hence, at the ends of the coupler, the ring waveguide acquires a larger angle with respect to the straight waveguide, and the EME method fails.

One effective method is the use of the super-mode theory [92], [93]. This method considers the two waveguides in a coupler as a single structure and calculates the two lowest order modes (called symmetric and anti-symmetric super-modes, which are orthogonal) at the input cross section — normal to the direction of wave propagation — of the coupler. The coefficient of each super-mode is computed by taking the overlap integral of the super-mode and the mode in each input waveguide. Provided the two waveguides in the coupler are parallel and the cross section remains unchanged, the two

super-modes maintain their respective effective indices as they traverse along the directional coupler. At the coupler output, the two super-modes arrive with a certain phase difference and thus, their overlap integrals with individual output modes determine each output amplitude. The method is rigorous provided the waveguides are well separated at input/output interfaces, and the mode profile of the super-modes well match with the individual input/output mode profiles and so the overlap integrals show no mismatch. Otherwise, the overlap integrals reveal mismatch loss and inaccuracy in results. Nevertheless, the technique is utilized with acceptable accuracy [83], [93]. A low-loss coupler may be modeled as:

$$T = \begin{pmatrix} r & k \\ -k^* & r^* \end{pmatrix}, \qquad with\ |r|^2 + |k|^2 = 1 \tag{3.7}$$

where r and k represent amplitude self-coupling and cross-coupling ratios, respectively. If the normalized coefficients of the super-modes with respect to input/output individual modes are chosen as:

$$S = \frac{1}{\sqrt{2}} \begin{pmatrix} 1 \\ 1 \end{pmatrix}; \qquad A = \frac{1}{\sqrt{2}} \begin{pmatrix} 1 \\ -1 \end{pmatrix} \tag{3.8}$$

where S and A correspond to symmetric and anti-symmetric super-modes, respectively, the overlap integral between the super-modes and the individual modes at the input/output interface gives

$$M = \frac{1}{\sqrt{2}} \begin{pmatrix} 1 & 1 \\ 1 & -1 \end{pmatrix}. \tag{3.9}$$

It is shown in [93] that if β_S and β_A are the propagation constants of the symmetric and anti-symmetric super-modes, respectively, the transfer matrix of the coupler is computed as:

$$T = M^{-1}EM = M^{-1}\begin{pmatrix}\exp(-j\beta_S l) & 0\\ 0 & \exp(-j\beta_A l)\end{pmatrix}M \tag{3.10a}$$

$$T = \exp(-j\beta_+ l)\begin{pmatrix}\cos(\beta_- l) & -\mathrm{j}\sin(\beta_- l)\\ -\mathrm{j}\sin(\beta_- l) & \cos(\beta_- l)\end{pmatrix} \tag{3.10b}$$

in which, E is the transfer matrix of the super-modes within the coupler and l is the coupler length. Also,

$$\beta_+ = (\beta_S + \beta_A)/2 \tag{2.11a}$$
$$\beta_- = (\beta_S - \beta_A)/2 \tag{2.11b}$$

Relation (3.10) is consistent with (3.7) and CCPR is the square of amplitude cross-coupling ratio, and is equal to

$$\mathrm{CCPR} = |k|^2 = sin^2(\beta_- l) = sin^2((\beta_S - \beta_A)l/2). \tag{3.12}$$

Relation (3.12) computes the CCPR for a directional coupler with parallel waveguides as already stated. A ring coupler, however, has a varying gap between its waveguides. To apply the super-mode theory to this structure, the ring coupler may be divided into a host of concatenated couplers, each with a small enough length so that for each section, the gap may be presumed constant, and relation (3.12) can be applied. Hence, the ring coupler can be modeled as a cascade of numerous small concatenate couplers. The overall transfer matrix is then attained using the Matrix Transfer Method (MTM) and is computed by multiplying the transfer matrixes of the cascaded elements. For a matrix in the form of the RHS of (3.10) we have

$$\begin{pmatrix} \cos(A) & -jsin(A) \\ -jsin(A) & \cos(A) \end{pmatrix} * \begin{pmatrix} \cos(B) & -jsin(B) \\ -jsin(B) & \cos(B) \end{pmatrix} = \begin{pmatrix} \cos(A+B) & -jsin(A+B) \\ -jsin(A+B) & \cos(A+B) \end{pmatrix} \quad (3.13)$$

Thus, the cascade of the small couplers results in

$$T = \exp(-j\varphi_+) \begin{pmatrix} \cos(\varphi_-) & -\mathrm{jsin}(\varphi_-) \\ -\mathrm{jsin}(\varphi_-) & \cos(\varphi_-) \end{pmatrix} \quad (3.14)$$

where

$$\varphi_+ = \frac{2\pi}{\lambda} \sum_{i=1}^{N} \frac{n_S(g_i) + n_A(g_i)}{2} \Delta z \quad (3.15a)$$

$$\varphi_- = \frac{2\pi}{\lambda} \sum_{i=1}^{N} \frac{n_S(g_i) - n_A(g_i)}{2} \Delta z \quad (3.15b)$$

in which, N, g_i, Δz, n_S, and n_A are the number of the small couplers, gap size at the i^{th} coupler, and the length of the i^{th} coupler, and symmetric and anti-symmetric super-mode effective indices, respectively. If $N \longrightarrow \infty$, then $\Delta z \longrightarrow 0$, and the summations in (3.15a) and (3.15b) turn into integrals as:

$$\varphi_+ = \frac{\pi}{\lambda} \int_{-z_{max}}^{+z_{max}} [n_S(x) + n_A(x)] dz \quad (3.16a)$$

$$\varphi_- = \frac{\pi}{\lambda} \int_{-z_{max}}^{+z_{max}} [n_S(x) - n_A(x)] dz \quad (3.16b)$$

where z_{max} is the distance from the center of the coupler to the point where the coupling starts/ends. At z_{max} the two super-modes have identical effective indexes beyond which no coupling occurs. Hence, the integral limits for φ_- can be extended to ±∞ as the integrand tends to 0 beyond z_{max}.

On the other hand, above a certain minimum gap size, $[n_S(x) - n_A(x)]$ may be modeled by an exponential function so:

$$\frac{\pi}{\lambda}\,[n_S(x) - n_A(x)] \simeq be^{-dx}. \tag{3.17}$$

For a ring coupler with a circular ring and a straight waveguide, the gap (x) is related to z as:

$$x(z) = x_0 + r\left(1 - \sqrt{1 - (z/r)^2}\right) \tag{3.18}$$

where r and x_0 are the outer radius of the ring, and the gap size in the middle of the coupler, respectively. Using Taylor series and for $z \ll r$, relation (3.18) may be approximated as:

$$x(z) \simeq x_0 + z^2/2r \tag{3.19}$$

This allows φ_- in (3.16) to be analytically computed as:

$$\varphi_- \simeq \int_{-\infty}^{+\infty} be^{-d\left(x_0 + z^2/2r\right)} dz = be^{-dx_0}\sqrt{2r\pi/d} \tag{3.20}$$

The cross-coupling power ratio (CCPR) is computed as:

$$CCPR = sin^2(\varphi_-). \tag{3.21}$$

To calculate the CCPR for the ADS-based ring coupler, the effective indices of the two lowest order (even and odd) super-modes are computed versus gap at 1565 nm with FIMMWAVE tool. Within a certain band, coupling in a coupler is maximum at the largest wavelength; thus, designing the ring coupler to achieve the target value of the CCPR at 1565 nm means that the CCPR at any other wavelength remains below that CCPR target.

Therefore, the target resolution of lower than 1 GHz is guaranteed in the entire C-band. Fig. 3.6 depicts $\frac{\pi}{\lambda}\,[n_S(x) - n_A(x)]$ versus the minimum gap size of the ring coupler. It is seen that for smaller values of the minimum gap, the difference between the super-modes is significant, while at larger gap values, the curve tends to zero. It is due to the fact that as the two waveguides part company, the two super-modes become closer in value and eventually identical when there is no coupling. Applying (3.17) to this curve, which is equal to a curve-fitting to an exponential function discloses the constant parameters of b and d, whose values are 1.432 x 10^5 and 2.45 x 10^6, respectively. Subsequently, using (3.20) and (3.21) the values of x_0 for the rings with radii of 540 and 180 μm and their corresponding CCPR of 4% and 1.35% — as calculated in the previous section — are computed. Both cases have identical values of $x_0 = 1.337\ \mu m$. For the case of fabrication with ±200 nm FPV, one might choose $x_0 = 1.537\ \mu m$ in the design, to ensure achieving a resolution of lower than 1 GHz in the worst FPV scenario. However, an increased minimum gap size results in an increase in insertion loss of transmitted power. That is, for a fabricated component with a real value of $x_0 = 1.537\ \mu m$, the CCPR for the rings with radii of 540 and 180 μm become 1.5%, and 0.5%, respectively, and their corresponding insertion loss values are -7.2 dB for both rings. Hence, adding a safety factor for FPV compensation may result in increased insertion loss. It should be noted that at the time the design was performed, the manufacturer was using contact lithography. Recently, it has started to use stepper lithography, which has an improved FPV performance.

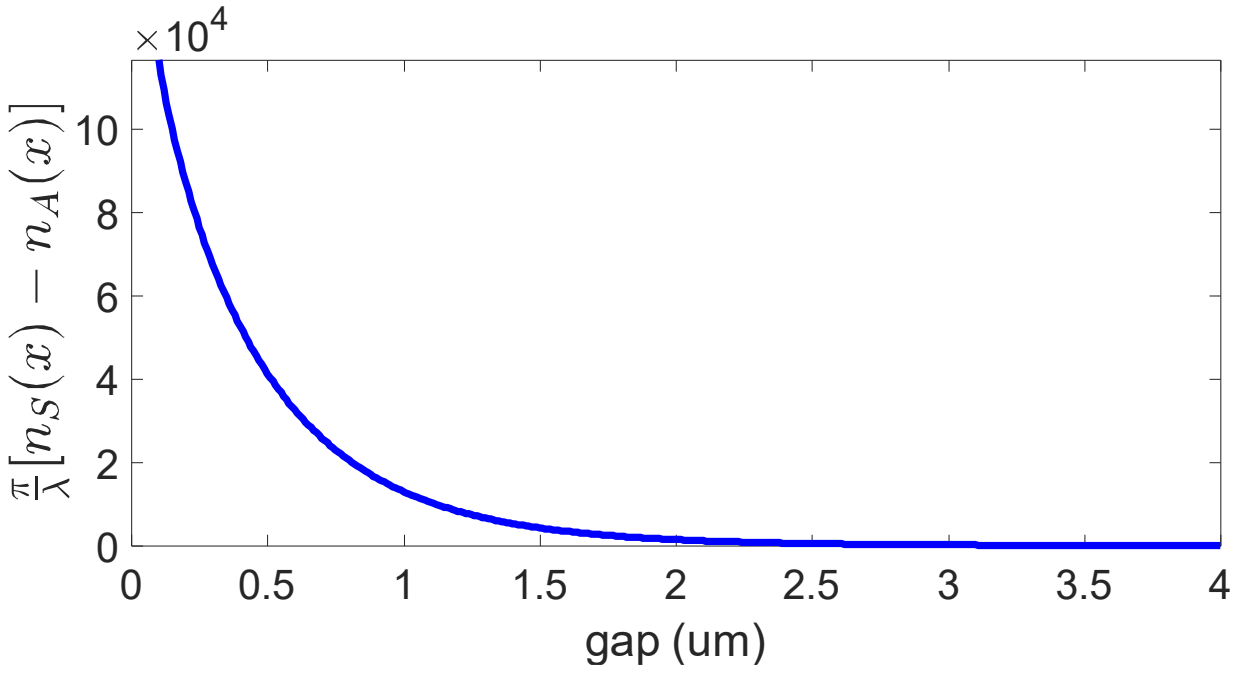

Fig. 3.6. The right-hand side of relation (3.17) versus the minimum gap size

The designed ring resonator was fabricated in different minimum gap values for a ring resonator with the FSR of 50 GHz to verify the validity of the simulations. Fig. 3.7 shows the picture of the fabricated chip with four ring resonators that have the same FSR but have different gap sizes.

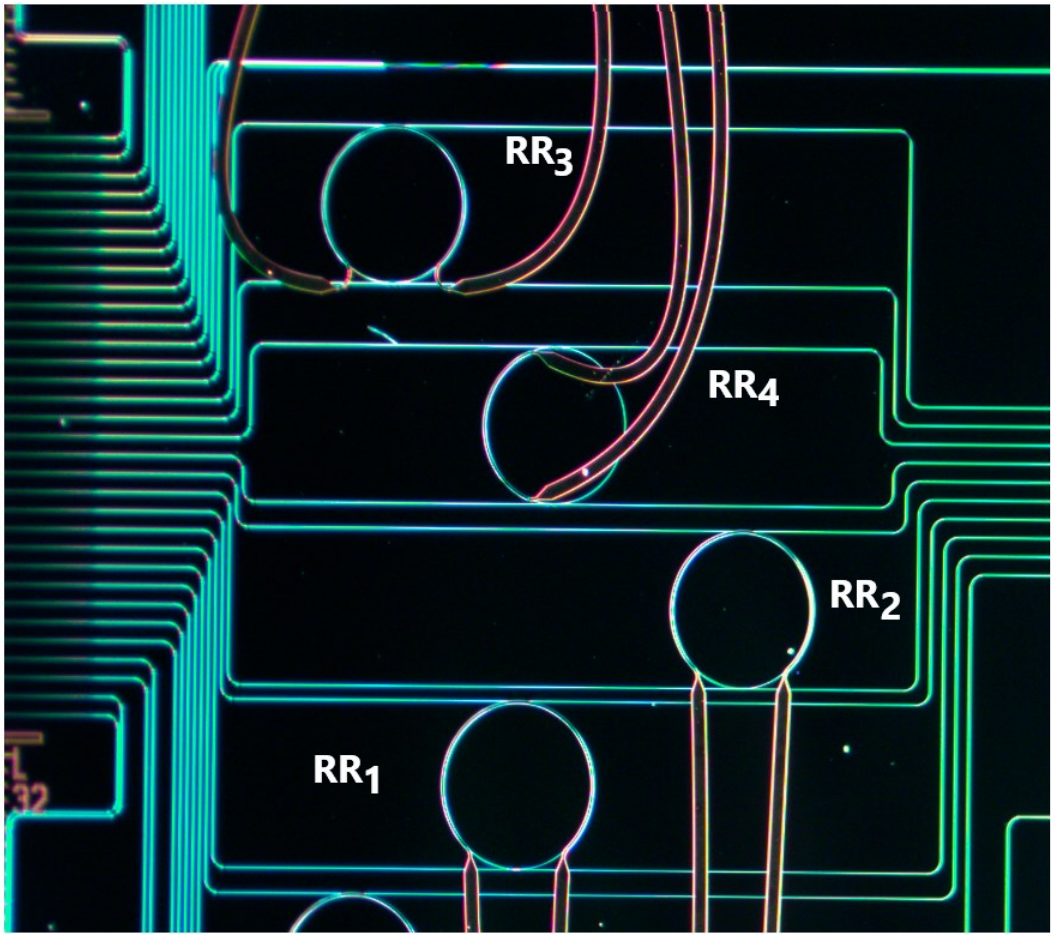

Fig. 3.7. The picture of the fabricated chip which includes ring resonators with the same FSR of 50 GHz but different gap sizes. RR; ring resonator. Adapted from G. M. Hasan *et al.* [83], licensed under Creative Commons Attribution 4.0 International.

The measurements of the ring resonators were carried out by other members of our research team. A comparison of the calculated and measured CCPR for the four minimum gap sizes of the fabricated ring resonators is performed by the other group members and is demonstrated in Fig. 3.8. A good agreement exists between the simulated and measured results.

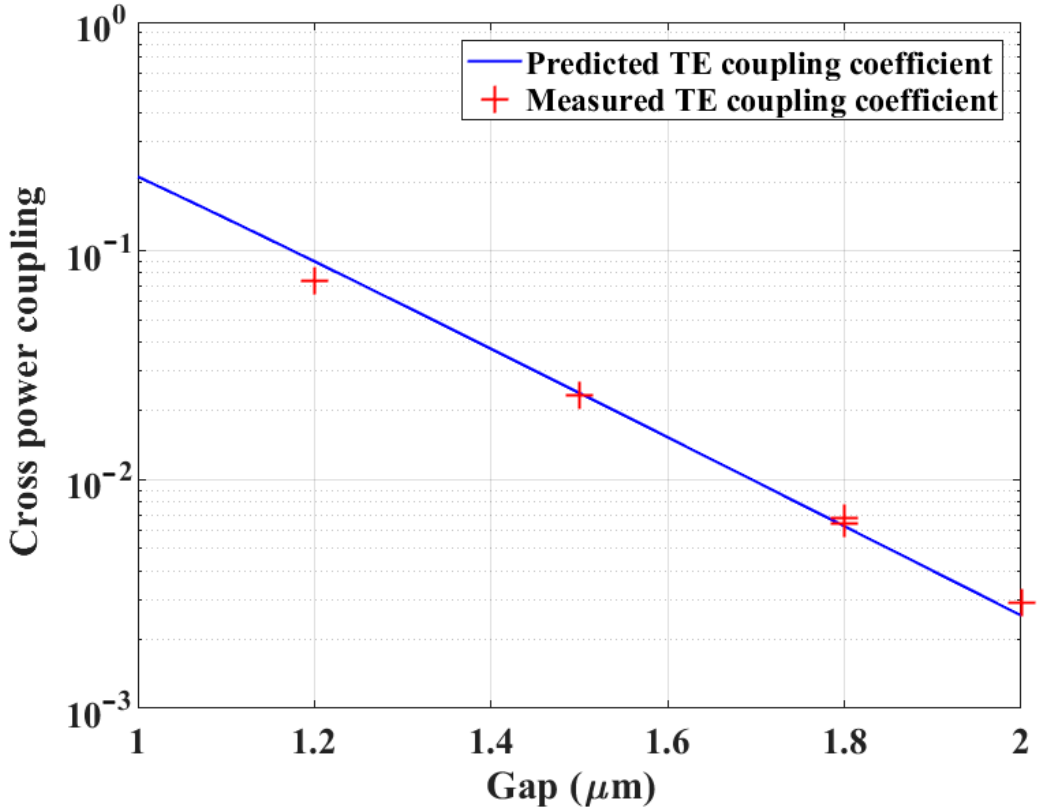

Fig. 3.8. The comparison of the simulated and measured CCPR values. Adapted from G. M. Hasan *et al.* [83], licensed under Creative Commons Attribution 4.0 International.

3.6 Summary of the main findings

The design feasibility evaluation of a silicon nitride ring resonator with a resolution of lower than 1 GHz and a finesse of at least 50 was performed in this chapter. First, the waveguide was introduced and characterized, and bend simulation was conducted to identify its bend loss. Then, the CCPR for a resolution of lower than 1 GHz was computed and finally using the super-mode theory, the minimum gap size of the ring coupler for the resolution of lower than 1 GHz was calculated.

Chapter 4 Ring Resonator Thermal Tuning

4.1 Introduction

Photonic integrated circuits (PIC) have revolutionized the photonics industry by dramatically reducing the system size from metre scale to just centimetres by gathering all components of a subsystem on a chip, which not only makes it easy for installation and maintenance, but also increases their reliability against mechanical vibrations, fluctuations in ambient temperature, and scales down the attenuation due to multiple fiber connections [94], [95], [96]. Monitoring an optical band consisting of many channels is key in communications systems to detect empty channels and allocate new signals to them. It also helps spot channels with defunct transmission. High resolution optical filters are required to detect optical channels with narrow bandwidth. The C-band spanning from 1530 to 1565 nm is one of the most crowded bands in optical communication systems. Fragmenting this band into sub-bands each with a bandwidth of lower than 1 GHz creates a huge number of narrow bands which calls for fine filtering. Scanning the C-band with a single fine PIC filter is very challenging. Hence, fine filtering in conjunction with coarse filtering has been proved as a practical answer to scan a wide spectrum with narrow-band channels. A combination of a ring resonator [62] as a fine filter and an arrayed waveguide grating (AWG) [97] as a coarse filter is a viable option which has been proposed to scan a wide optical band [83], [98], [99], [100].

The ring resonator as a key PIC component is used as a highly selective tunable filter. Its transmission function consists of a regular comb of narrow resonances (transmission peaks or notches depending on the configuration). The frequency interval

between resonances is known as the free spectral range (FSR). Low loss design of a ring resonator ensures its high-resolution performance as a fine filter. The resonant frequency of the ring resonator can be tuned by inducing a change in the effective index of the mode traversing the ring waveguide thereby adjusting the total optical path length. A path length change of one wavelength tunes the resonance comb over one FSR. In conjunction with a means of selecting any individual comb line, tuning over a single FSR is sufficient to effectively tune a single comb line over an arbitrarily broad band. It is noted that the goal in the above-mentioned configuration is to design a high-resolution ring resonator and ensure its tunability over an FSR.

An AWG on the other hand, acts as a coarse filter, where depending on the circuit architecture, it will require a channel spacing equal to one or a fraction of the FSR of the ring resonator. Such configurations make it feasible to scan the whole desired band by tuning the ring resonator by the amount of one FSR. Due to their dispersion mechanism arising from the phase difference between grating arms, AWGs are susceptible to phase errors, which degrade their performance [101]. To enhance their robustness against phase errors, different techniques such as using arrayed waveguides that are less sensitive to fabrication process variation (FPV) errors [102], designing on a low index contrast platform [103], designing with a larger channel spacing [59], could be applied. Thus, one would aim at an AWG designed on a low loss platform, made of waveguides resilient to FPV errors and with a large channel spacing. This requires a high-resolution ring resonator with the right FSR to be tunable over its FSR to fulfill the AWG requirement in the described scheme.

High-resolution ring resonator design needs to minimize the loss emanating from the scattering, absorption, bend, ring coupler mode mismatch as well as straight-to-bend mode mismatch loss in case of race-track resonators. Among many available PIC platforms, silicon nitride (Si_3N_4) has the advantage of low loss compared to silicon on insulator (SOI) [21], [104] while attaining a smaller footprint compared to doped silica devices [38]. A silicon nitride ring resonator enjoys a relatively small footprint and high FSR compared to one made on doped silica platform for a certain bend loss as design target due to higher core to cladding refractive index contrast which admits tighter bends; It also has less waveguide loss than an SOI platform, enabling the attainment of higher resolution filters for a certain FSR. Its higher achievable FSR compared to doped silica-based ring resonators for specified bend loss, allows an AWG design with a larger channel spacing, enhancing the AWG performance in terms of phase errors. Moreover, an increased channel spacing in an AWG decreases the number of output channels of the AWG, significantly reducing the complexity of the layout and the number of photodetectors and overall cost of the device.

The design of a low loss silicon nitride ring resonator with emphasis on the ring coupler for a resolution of lower than 1 GHz for a ring resonator with an FSR of 50 GHz has been investigated in [83]. A ring resonator with a higher FSR while maintaining a resolution of lower than 1 GHz requires less cross coupling power in the two ring coupler regions, which is usually achieved by increasing the gap in the couplers. While the on-resonant transmission remains unity in a lossless ring resonator regardless of the gap size, the increased gap in a lossy ring resonator will, however, result in an increase in the insertion loss. This is a trade-off between a high resolution and a low insertion loss design.

A designer needs to minimize the effects of all loss mechanisms to achieve the best performance.

Fine tuning of ring resonators has been demonstrated using a variety of physical effects including electro-optic (EO), piezo-electric (PE), and thermo-optic (TO) tuning. EO tuning mechanism alters the optical properties of the waveguide core or cladding by applying electrical field to the waveguide so that the effective index of the traversing wave changes. It calls for materials whose optical properties change significantly by applying electric field. In CMOS platforms, usually part of the cladding is replaced with special matters like lithium niobate or liquid crystal to achieve desired tuning [47], [105], [106], [107], [108], [109]. PE tuning causes mechanical change in the physical dimensions of the structure such as waveguide cross-section or length by applying electric field. The change in physical dimensions brings about optical tuning [46], [110], [111], [112]. TO tuning changes material refractive index by heating. It can be achieved by depositing a layer of highly resistive metal atop the waveguide structure. The resistive heater needs to be placed sufficiently away from the waveguide so that the caused optical loss resulting from light interaction with metal remains negligible. Applying electrical current to the heater scales up its temperature, heating the entire structure underneath. The temperature change causes the refractive index of the core and cladding to shift and so, tuning is obtained. [45], [113], [114], [115], [116]. While mostly highly resistive metals are used as heaters, other materials such as graphene are also considered for TO tuning [117], [118], [119]. The advantage of graphene is its significantly lower absorption loss compared to metals, so it can be placed very close to the waveguide, increasing thermal efficiency. Its implementation is more challenging than resistive metals, though. Tuning

can also be conducted using doped matter near the waveguide structure [113], [120]. For some dopants, light interaction with them generates heat and TO tuning mechanism takes place. For others, the dopant increase directly changes the structure refractive index and tuning is achieved.

The thermo-optic tuning, albeit slower than the other methods, is the simplest to implement due to simply depositing a layer of resistive metal above the waveguide structure to act as an electrical heater. The other methods call for specific materials less suited to deposition or the waveguide material itself to posses the desired EO or PE properties, imposing restrictions on the photonic design or adding to the complexity and cost of manufacturing. While many research groups have used thermal heaters for tuning, the tuning investigation itself has not widely been discussed. The design and analysis of a thermo-optic phaser shifter for a tunable Mach-Zehnder Interferometer (MZI) on an SOI platform has been performed in [121]. Authors in [122] carried out the design of a thermo-optic phase shifter for a silicon nitride MZI, exploring the design trade-off between different parameters. A study on silicon nitride thermal tuning was performed in [123] examining the effects of heater material, trenches and undercuts on performance.

In this chapter, the thermal tunability of silicon nitride ring resonators with different FSRs for three practically used waveguide structures operating over the C-band for the fundamental TE mode is assessed considering the FPV errors impacting the device performance. Applying data from practical materials as well as considering the FPV errors in the simulations ensures the obtained results are reliable and consistent with the performance of a fabricated chip. The effect of design variations on the electrical power needed for tuning is assessed and the extent of the tunability range of ring resonators

which is limited by the maximum safe operation temperature is estimated. While the targeted application of the tunability analysis of silicon nitride ring resonators in this thesis is the wavelength scanning function of an on-chip spectrometer, tunable ring resonators have a wide range of applications in different circuits as reconfigurable filters and modulators.

4.2 Method

The goal is to design a tunable ring resonator that has negligible bend loss compared to the intrinsic loss of the waveguide. First, the bend loss of rings made of various waveguides are evaluated using Photon Design's FIMMWAVE simulation tool. Proper ring resonator radii that demonstrate negligible bend loss are identified. Then, with the computed radius limits, ring resonator tunability is assessed in the fundamental TE mode. Proper distances between the heaters and waveguide cores are calculated so that mode losses caused by the presence of the resistive heater remain negligible compared to the total losses.

Tuning a ring resonator is conducted by changing the mode effective index in the ring waveguide. The needed change in the mode effective index for a resonance shift equal to one FSR is

$$\Delta N_{eff} = \lambda_0 / L \tag{4.1}$$

where λ_0 and L represent the central wavelength and the physical length of the ring, respectively. The variation in the effective index change in (4.1) due to shifting the local wavelength within the C-band is negligible. The thermal tuning of PIC components is

conducted by heating the structure, so the refractive indices of the materials vary due to their dependence upon temperature. The temperature dependence of a material refractive index is linear to a good approximation and can be represented as:

$$n(\lambda, T) = n(\lambda, T_0) + \left(\frac{dn}{dT}\right).\Delta T \tag{4.2}$$

where *T* is temperature, T_0 is the room temperature (293.15 °K), and dn/dT is refractive index temperature coefficient, which is a constant over the wavelength and temperature of study, and λ is the wavelength [124]. The structure of the waveguides in the studied ring resonators in this work consists of silicon nitride as core and silica as cladding with refractive index temperature coefficients equal to 2.45 x 10^{-5} /°K and 0.95 x 10^{-5} /°K, respectively. Fig. 4.1 depicts the cross section of a silicon nitride waveguide with a heater atop. The terms BOX, TOX, and OHX stand for buried oxide, top oxide, and over-heater oxide layers, respectively. Passing an electrical current through the resistive heater brings about a rise in temperature of the heater which subsequently increases the temperature in the waveguide cross section as heat traverses down away from the heater, resulting in a change in the refractive index of the material which alters the effective index of the mode and shifts the resonant wavelength of the ring resonator.

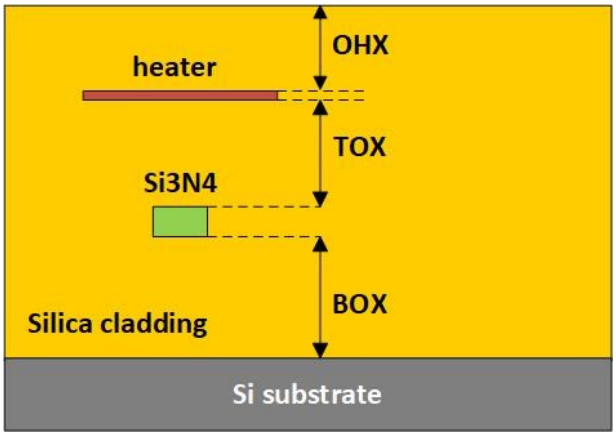

Fig. 4.1. Cross-section of a waveguide and heater.

COMSOL Multiphysics' finite element method (FEM) is used to simulate heat transfer as well as the optical mode of the waveguide (fundamental TE mode) in the presence of thermally induced refractive index change. Simulations consist of steady-state and time-dependent parts, with the former aimed at determining the ultimate heater temperature and total required electrical power for tuning over one FSR, while the latter is aimed at determining the tuning speed. All boundaries of the structure are set to free air convection, except the bottom side which is placed atop a heat sink with the constant room temperature.

In the first stage of the steady-state simulations, the two-dimensional (2D) cross-section of the waveguide and heater is simulated to find the required ultimate temperature in the heater for the desired shift in the effective index to take place. This simulation also reveals the limits in the heater width considering the maximum allowed temperature in the heater for its safe operation. In the second stage, the three-dimensional (3D) chip is simulated with the voltage applied to the resistive heater circuit to determine the required electrical power to increase the temperature of the heater to the value obtained in the first

stage. The temperature dependence of the heater resistance is considered to achieve reliable simulation results.

Next, time-dependent simulations are conducted to calculate the scanning speed for a tuning by the amount of one FSR and then going back to its initial state. The electrical power is applied as a triangular waveform whose frequency is the scanning rate. The power starts from zero and reaches its peak where a tuning equal to an FSR is attained; It then goes down to zero to complete one period of scanning where the resonant wavelength goes back to its initial state. In practice, a wavelength meter is used to measure the resonant wavelength on the fly as tuning is carried out. The tuned wavelength will follow the triangular shape of the applied electrical power with a certain time delay. However, the top and bottom peaks will be rounded off as the settling time for a certain tuning is theoretically infinite, and the maximum applied power only exists for a moment before starting to decrease. In other words, the electrical power calculated in the steady state simulations and applied in the form of a triangular waveform, cannot achieve a full FSR tuning. The higher the scanning rate becomes, the lower amount of the FSR is tuned. To overcome this problem, the applied power is increased provided the heater operates without failure. By applying the maximum allowed power to the heater at the peak of the triangular waveform, and targeting a full FSR tuning, the highest possible scanning rate can be computed.

4.3 Studied waveguides

The FSR of a ring resonator is inversely proportionate to its radius. So, an increased FSR calls for a tighter bend, and increases the bend loss. Therefore,

waveguide cross-sections with stronger light confinement in the core which makes them more tolerant to tighter bends are preferred. Three silicon nitride waveguide structures, designed by industry [81], [125] are studied taking account of their FPV errors to acquire trustable simulation results. The schematics of the three waveguide cross-sections used in the simulations are presented in Fig. 4.2.

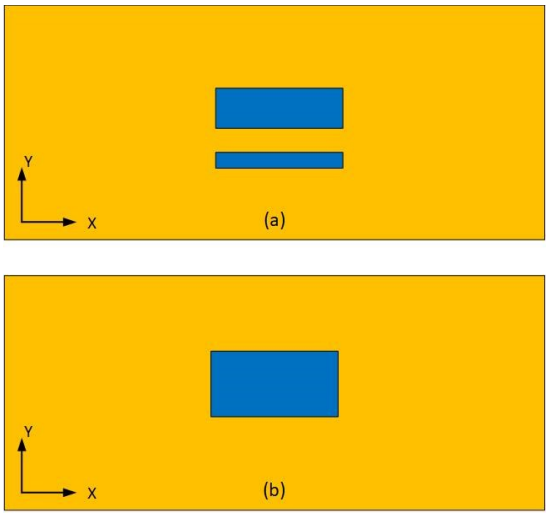

Fig. 4.2. Schematic cross-section of the simulated waveguides. a) ADS, b) AN800 and AN400. The shapes are not to scale.

The first waveguide structure has a core consisting of two separate silicon nitride strips with a lower layer thickness of 75 nm and an upper layer thickness of 175 nm separated by a 100 nm thick silica layer. The width of the top side of the upper strip is 1100 nm with a sidewall etching angle of 82 degrees with respect to the horizontal axis for the whole structure. This waveguide structure is referred to as the Asymmetric Double Strip (ADS) waveguide, which is also elaborated in Chapter 3. The waveguide is more tolerant to tight bends compared to other available types by the same manufacturer, which better fulfills the requirement of tighter bends and consequently higher FSRs [44]. It supports a single mode regime for TE polarization regardless of its FPV error. The FPV

error of this waveguide fabricated by contact lithography is up to 5% change in the thickness of deposited layers and ±200 nm in waveguide width. It should be noted that the manufacturer now is using the stepper lithography with much smaller FPV error values compared to the older contact lithography, based on which our design and simulation are performed.

The second and third waveguides have single cores of 800 nm and 400 nm thicknesses, and are named as AN800 and AN400, respectively [25]. The width of the top side of the strips are 1 um with an etching angle of 89 degrees. The FPV errors for both cases are up to ±4 nm in thickness change and up to ±10.4 nm in width change. The AN800 waveguide structure has the highest mode confinement among the studied waveguides and thus, has more tolerance to tighter bends. It also allows the heater to be placed closer to the core due to light penetrating less into the cladding, which reduces the required tuning power. The AN400 is a single mode waveguide over the C-band for either polarization while AN800 takes in higher order modes as well, so care must be taken in the design of components with AN800 to ensure that higher order modes are not excited. To compare the three waveguides, the effective indexes of the fundamental TE modes of the standard-sized waveguides versus wavelength over the C-band are computed using FIMMWAVE tool and depicted in Fig. 4.3. It is noted that the ADS and AN800 waveguides have the lowest and highest effective indexes, respectively. The higher effective index is an indicator of more light confined in the silicon nitride core of the waveguide. This allows tighter bends as well as closer vertical distance between the core and heater (see Fig. 4.1), which are explained further later in the chapter.

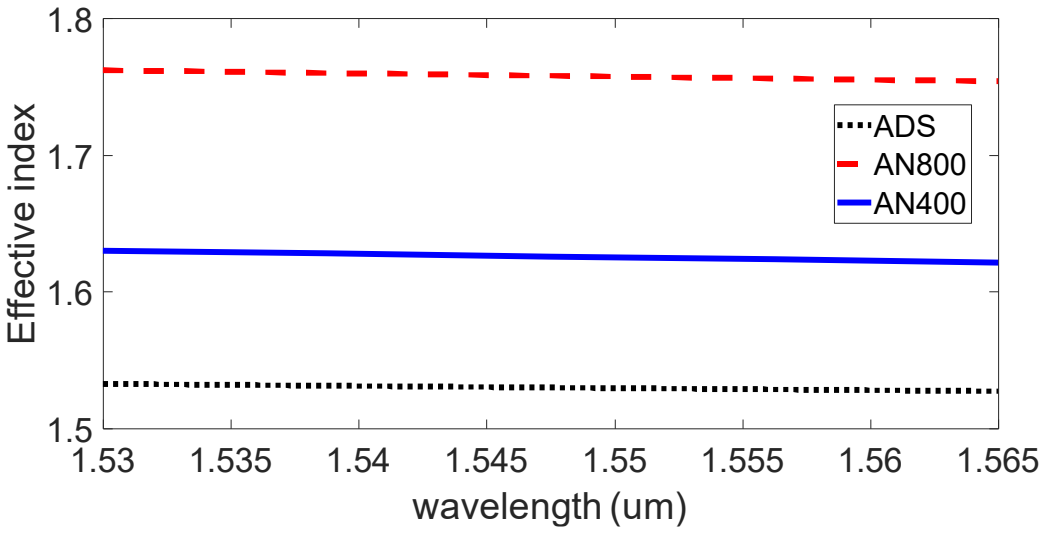

Fig. 4.3. A comparison of the fundamental TE mode effective indexes for the three standard-sized waveguides versus wavelength.

4.4 Ring resonator thermal tuning

The refractive index of the waveguide materials varies with temperature; thus, heating the waveguide results in a change in the effective index of the mode propagating in the waveguide and shifts the resonant wavelength of a ring resonator. Resonance wavelengths are spaced by the amount of one FSR; hence, tuning the resonant wavelength by the amount of one FSR scans the whole band. An increase in the FSR needs a larger shift in the mode effective index to sweep that FSR, which requires a higher temperature in the heater. The items that need to be considered in the heater design are the material, layout, power supply, width, distance from the waveguide core, and the presence of a cladding layer deposited over the heater (see Fig. 4.1).

4.4.1 Heater layout

A heater is designed to deliver thermal power to an optical waveguide structure in an efficient way. For a ring geometry, a convenient way to lay out a heater is to follow the waveguide underneath. Fig. 4.4 illustrates the shape of the heater in our design. The circular shape ensures the heater remains close to the waveguide for efficient tuning. The metals outside the circular section are for connecting to a power supply and are made of a different metal with relatively lower resistivity (in this case silver) in order not to dissipate power in unwanted regions of the circuit. It should be noted that the heater layout is not restricted to a full-ring case, and it can have layouts that cover the ring partially, e.g., a half-ring heater, in which case the resistance is halved. The amount of the tuning power, however, does not change for a different heater layout as the thermal power consumed for a certain shift in resonance wavelength, is constant. Hence, a full-ring heater draws less current than for example a half-ring and operate at a lower temperature.

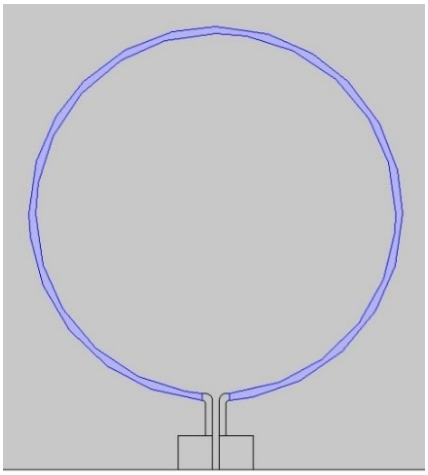

Fig. 4.4. Heater shape designed for a ring resonator with the highly resistive part highlighted.

One important matter in the heater design is the minimum distance between the positive and negative ports of the circuit. As the two opposite ports at the two ends of the heater experience a significant voltage difference, dielectric breakdown can take place if the two ports are placed too close. Dielectric breakdown is proportional to permittivity. The higher the permittivity, the more voltage difference is required for a breakdown. The minimum distance calculation is usually carried out by assuming air as the material between the ports of the heater, which is the case when no cladding exists over the heater. Air has the minimum permittivity among dielectrics and thus has the lowest dielectric breakdown value. So, a design for air works safely for other dielectrics, too. The value of the dielectric breakdown for air is 3 kV/mm. Once the maximum applied voltage to the heater is determined, the minimum safe distance can be identified.

4.4.2 Heater material and power supply

The heater needs to be made of a material with high resistivity to produce a large amount of heat from the electrical current flowing through it. On the other hand, as the electrical resistivities of metals normally have positive temperature coefficients, injecting power with a current source can cause thermal runaway. It is because the metal resistance increases by temperature rise and thus, constant injected electrical current scales up the drawn electrical power which causes the device to overheat and fall apart. Therefore, the power needs to be fed into the heater by a voltage source to ensure the total injected power remains under control and guarantees a safe device operation.

The heater failure takes place because the heater and waveguide cladding on which the heater is deposited possess different thermal expansion coefficients. As the

structure is heated, the two objects expand with different expansion ratios causing a bend in the structure. An excessive bend can induce either of the waveguide or the heater structures to fall apart if either object reaches its own yield stress i.e., the amount of the stress that causes a migration from the elastic region to the plastic one — in this case being a physical break for silica cladding or for the heater. Another factor that causes a heater failure is the detachment of the heater from the waveguide once the applied surface tensile stress due to the heating exceeds the limit. Hence, the design of the heater must consider the operational limit, which is represented in terms of a maximum electrical current density for a certain heater cross-section or equivalently, a maximum temperature in the heater, usually obtained by experiment and provided by a manufacturer. Table 4.1 shows two different heaters deposited on silica cladding made of Chromium (Cr) [24] and Aluminum (Al) [25] and their practical data consisting of thickness, electrical current density limit, temperature limit, and electrical resistivity at the room temperature. The limiting temperature for the Cr heater was not provided by the manufacturer and was achieved through the simulation of the heater operating at the limiting current density.

Table 4.1. Practical specifications for two different heaters

Heater	Cr	Al
Layer Thickness (nm)	150	400
Resistivity at room temperature (ohm.m)	7.5 ~ 9 e-7	3.3 e-8
Current density limit (MA/cm^2)	1.33	3
Temperature limit (°K)	506	473

It should be noted that the resistivity of a thin film metal differs from that of a pure material and the values in Table 4.1 are acquired from the manufacturers. Moreover, the temperature-dependent resistivity properties of the metals need to be included in the simulation [126]. The thermal and electromagnetic properties of the materials used in the simulation are provided in Appendix A. Also, heater thickness is a value usually set by manufacturers, which is related to the fabrication technology. The higher resistivity a heater has, the less electrical current it draws for a certain electrical power dissipation.

4.4.3 Heater width and its vertical position

Fig. 4.5 illustrates a waveguide and heater cross-section and a steady-state temperature distribution in COMSOL. It is deduced from the figure that a wider heater irradiates a larger area and so a lower heater temperature is needed for a certain amount of tuning [19]. Conversely, a narrower heater width requires a higher temperature in the heater.

Operation at a higher temperature is not preferred as it limits the extent of the tunability due to heater failure; hence, a wider heater is preferred to a narrower one. On the other hand, for a heater that is wider than the waveguide core by an order of magnitude, the required heater temperature remains almost constant as can be deduced from Fig. 4.5. Heater temperature is related to electrical current density. Therefore, excessive increase in the heater width will scale up the total current. The electrical power is proportional to the resistance multiplied by the square of the current. Although a wider heater has a reduced resistance, the squared effect of current prevails, and the total amount of the electrical power is raised. A trade-off between a higher operational

temperature with a narrower heater and a higher consumed power with a wider heater can be made.

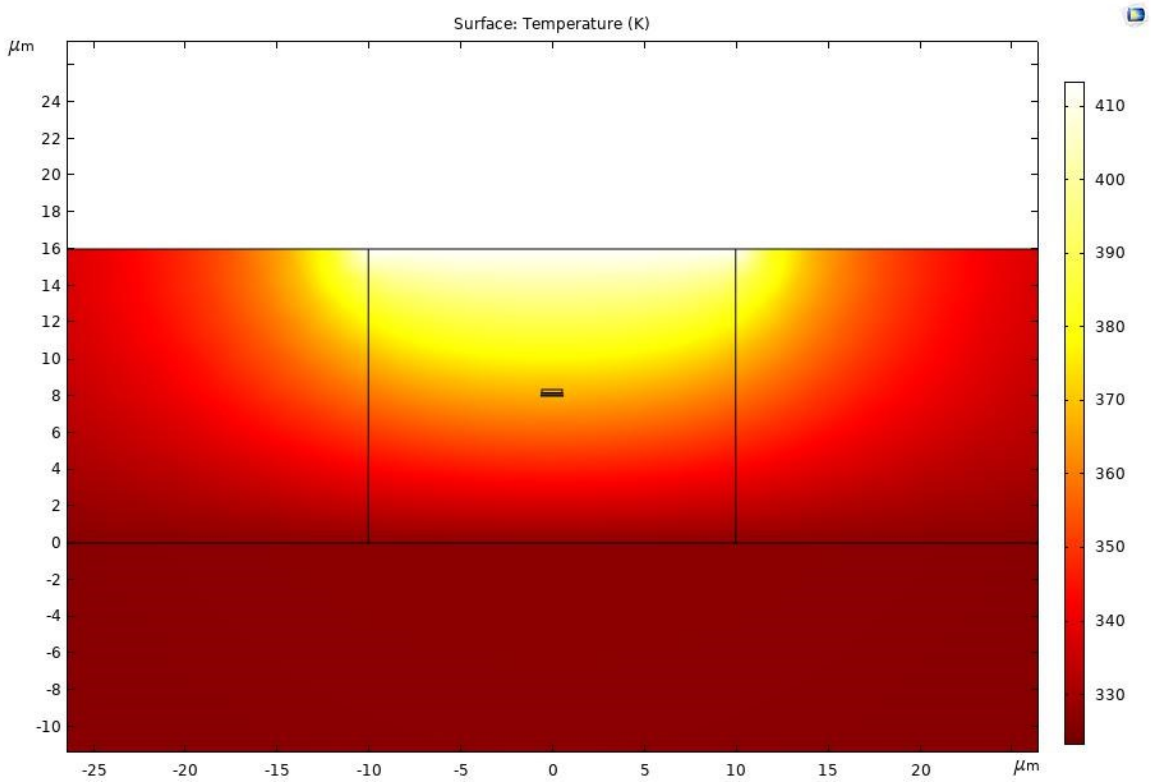

Fig. 4.5. Typical waveguide and heater cross-section and temperature distribution.

Moreover, as seen in Fig. 4.5, a larger distance between the waveguide core and heater, calls for a higher temperature in the heater for a certain tuning to take place; On the other hand, the interaction of a metallic heater with an optical mode result in optical loss, which is undesirable. Thus, the selection of the distance between the heater and waveguide core must be carefully performed to minimize the heater temperature while the added optical loss remains negligible. For the application of this work which aims at obtaining a low-loss ring resonator, minimizing the optical loss is pivotal; however, a design for a minimized power consumption may tolerate more optical loss than this application.

4.5 Simulations

4.5.1 Bend

The first step in characterizing the heater is bend loss evaluation, which determines appropriate values for the ring radius for the fundamental TE and TM modes of the waveguides. The bend loss analysis considers a worst-case scenario, in which the waveguide core has the minimum dimensions within the bounds of the FPV errors guaranteed by the manufacturers. Moreover, operation at the upper edge of the C-band (1565 nm) is assumed in the simulations as the bend loss increases with wavelength. Bend loss simulations for the ADS waveguide are conducted with 5% less thickness for layers as well as 200 nm less waveguide width. A similar approach is followed for AN800 and AN400 waveguides with 4 nm less thickness and 10.4 nm less width. Bend simulations are carried out by applying the Finite Difference Method (FDM) mode solver of Photon Design's FIMMWAVE tool and for bend radii corresponding to FSRs that are multiples of 50 GHz. Table 4.2 displays the computed bend loss values for both fundamental TE and TM modes for ADS, AN800, and AN400 waveguides for different FSRs.

Table 4.2. Bend loss for fundamental TE and TM modes in ADS, AN800, and AN400 waveguides for different FSRs

Mode / FSR	ADS TE	ADS TM	AN800 TE	AN800 TM	AN400 TE	AN400 TM
50 GHz	Negligible	0.4 dB/cm	Negligible			Negligible
100 GHz		High				

150 GHz	0.004 dB/cm	High	Negligible	Negligible
200 GHz	0.144 dB/cm			
300 GHz	High			0.02 dB/cm
400 GHz				0.4 dB/cm
500 GHz				

Simulation results reveal that the ADS waveguide has negligible bend loss compared to the waveguide intrinsic loss — 0.5 dB/cm as a specified maximum value provided by the manufacturer— for the TE mode for FSRs up to 150 GHz and a bend loss amount of 0.144 dB/cm for an FSR of 200 GHz. Rings with higher FSRs exhibit excessive bend loss. The TM mode, on the other hand, demonstrates a significant bend loss, which is not negligible compared to the intrinsic loss even for a ring with an FSR of 50 GHz. This means that the ADS waveguide is only reliable for the TE mode operation in rings with FSRs of up to 150GHz or 200GHz depending upon application requirement. The AN800 waveguide results show negligible bend loss for both polarizations in rings with FSRs of up to 500 GHz. Its declared intrinsic loss is 0.2 dB/cm. Rings made of the AN400 waveguide have negligible bend loss for FSRs up to 500 GHz for the TE mode. For the TM mode, bend loss is negligible for an FSR of 300 GHz, and a trivial bend loss of 0.02 dB/cm exists for the FSR of 400GHz — in comparison to the intrinsic loss of roughly 0.3 dB/cm as a value provided by the manufacturer for the AN400. With bend simulation results, maximum suitable FSRs of the ring resonators made of the three waveguides are determined.

4.5.2 Heater distance from waveguide core

To find out optimum values for TOX (see Fig. 4.1), extra optical losses of waveguides due to the presence of the heater are computed by varying TOX thicknesses considering the minimum waveguide dimensions guaranteed by the manufacturers within the bounds of the FPV errors. Photon Design's FIMMWAVE tool is used to conduct the simulations. The heater width is chosen to cover all the width of simulated cross-sections to ensure the acquired amounts of optical losses are reliable as worst-case scenarios. As the ADS waveguide is only reliable for the TE case according to the bend simulation results, only the TE mode is evaluated. The corresponding simulations of the AN800 and AN400, however, are conducted for both polarizations. It should be noted that except for the case of a polarization-independent ring resonator, a typical ring resonator is birefringent due to the asymmetrical geometry of the ring coupler and the waveguide birefringence, and thus, it is usually designed to operate with a specific polarization state only. In the simulations of the bend loss and the vertical position of the heater, however, both TE and TM polarizations are examined to ensure that the calculated allowable bends and the vertical positions of the heaters work well for either polarization. As mode expands with wavelength in the waveguide cross-section, this simulation is also carried out at 1565 nm to capture the maximum possible loss. As this application calls for minimum loss, an optimum TOX value is the minimum possible value at which added optical loss due to a heater presence is negligible compared to waveguide intrinsic loss. The simulation was conducted for TOX values with steps of 0.5 μm. Fig. 4.6 demonstrates the optical loss versus the vertical distance (TOX) between a waveguide core and Cr heater that is 20 μm wide and 150 nm thick (see Table 4.1) for the ADS, AN800 and AN400 waveguides.

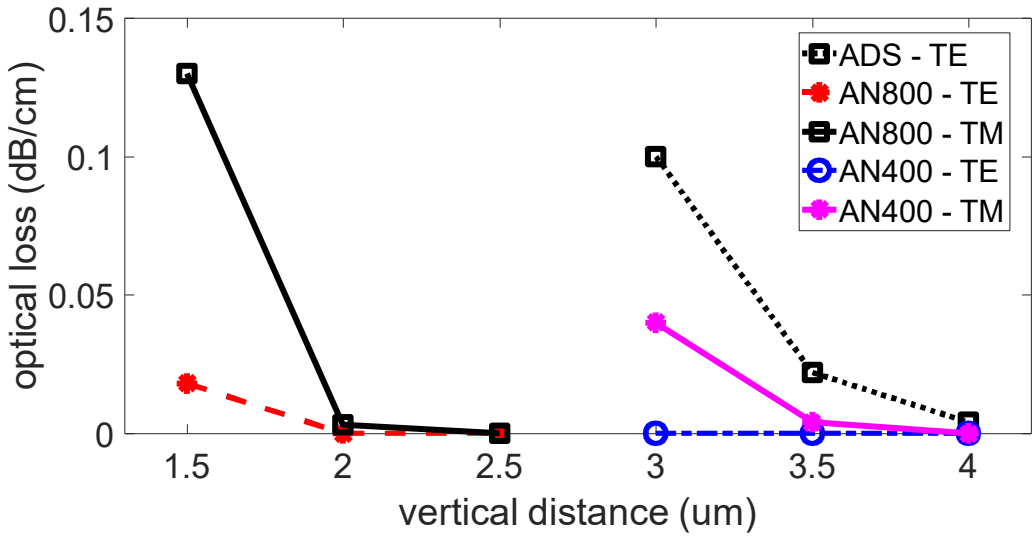

Fig. 4.6. Optical loss versus the vertical distance between a waveguide core and the Cr heater (TOX) for the ADS, AN800 and AN400 waveguides.

It is seen from the figure that the optimum TOX values of the ADS, AN800, and AN400 waveguides are 3.5 μm, 2 μm, and 3.5 μm, respectively. As expected, the AN800 has a lower TOX value than the other waveguides because of a larger core size, which accommodates a larger amount of a mode inside the core and less light spreads in the cladding; thus, the heater can be placed closer to the waveguide core, which lowers the required heater temperature. It is also noted that the TE mode is spread less than the TM mode in the cross-section and as such, experiences less loss.

4.5.3 Heater width effect

Steady-state thermal simulations are carried out for varied heater widths in ring resonators with different FSRs to assess the effect of the heater width on the power consumption and tunability extent. The heat transfer coefficient in free air convection boundary conditions is set to 10 W/m^2K. Optical mode simulations in COMSOL using the

FEM meshes are conducted for the fundamental TE polarization at the upper edge of the C-band (1565 nm) as the worst-case scenario. The surface area of the simulated chip is 16 x 16 mm^2— the typical size of the optical chips. The contact pads as seen in Fig. 4.4 are made of silver which has an order of magnitude lower resistivity than the resistive heater. The gap between the two silver pads is 40 μm which ensures that a dielectric breakdown is prevented provided that the applied voltage is kept below 120 V. The silicon substrate has a thickness of 1.5 mm sitting on a 5 mm thick copper layer for mechanical stability. Under-cladding thickness (BOX) is 8 μm (see Fig. 4.1) while TOX value is varied with respect to each waveguide structure as discussed in the past section. The resistive heater is made of Cr with OHX layer thickness of 2 μm. The simulations are performed by applying temperature-dependent electrical resistivity of the heater. As seen in Appendix A, Cr heater resistivity varies in practice; the upper bound of the resistivity is used in the simulations so that for a certain amount of the injected electrical power, an upper bound for the required voltage is identified.

Fig. 4.7 depicts the needed temperature increases from the room temperature (293.15 °K) to tune the ring resonators by the amount of one FSR versus the width of the heater. A lower bound of 1.5 μm for the width of the heater is selected in line with the minimum feature size allowed for the heater layer by the manufacturers.

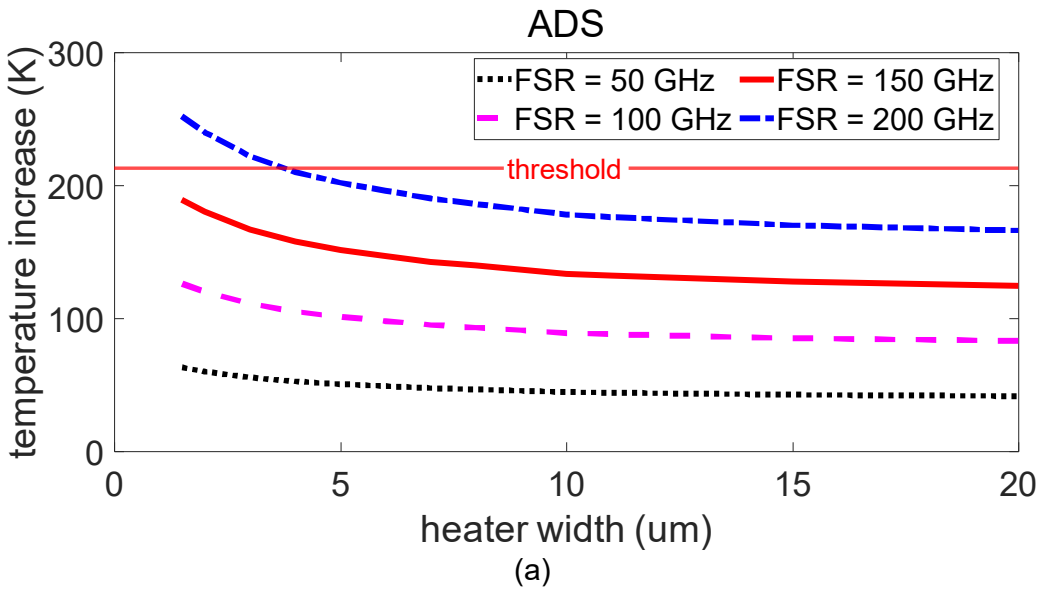
ADS
FSR = 50 GHz
FSR = 150 GHz
FSR = 100 GHz
FSR = 200 GHz
threshold
temperature increase (K)
300
200
100
0
0
5
10
15
20
heater width (um)
(a)

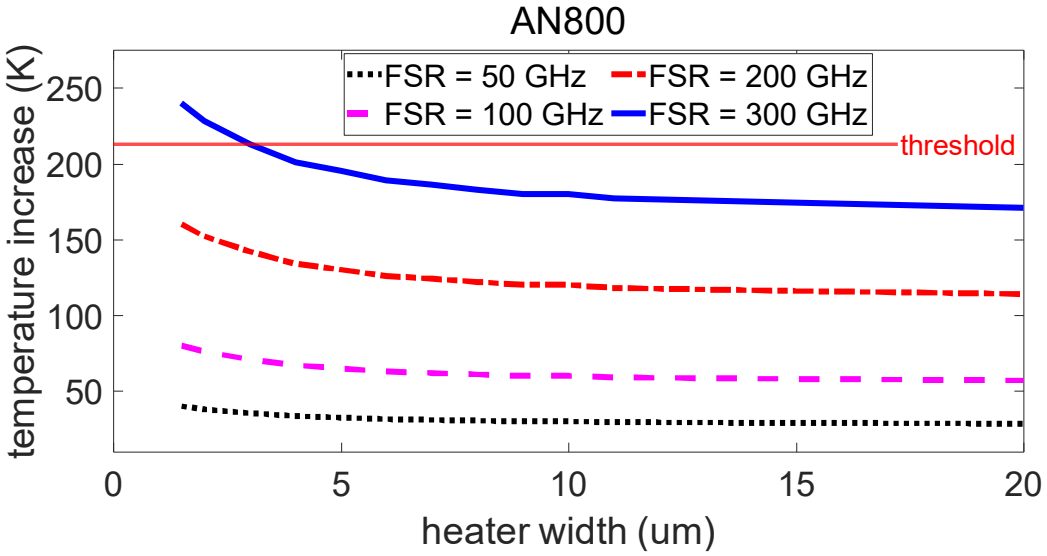
AN800
FSR = 50 GHz
FSR = 200 GHz
FSR = 100 GHz
FSR = 300 GHz
threshold
temperature increase (K)
250
200
150
100
50
0
5
10
15
20
heater width (um)
(b)

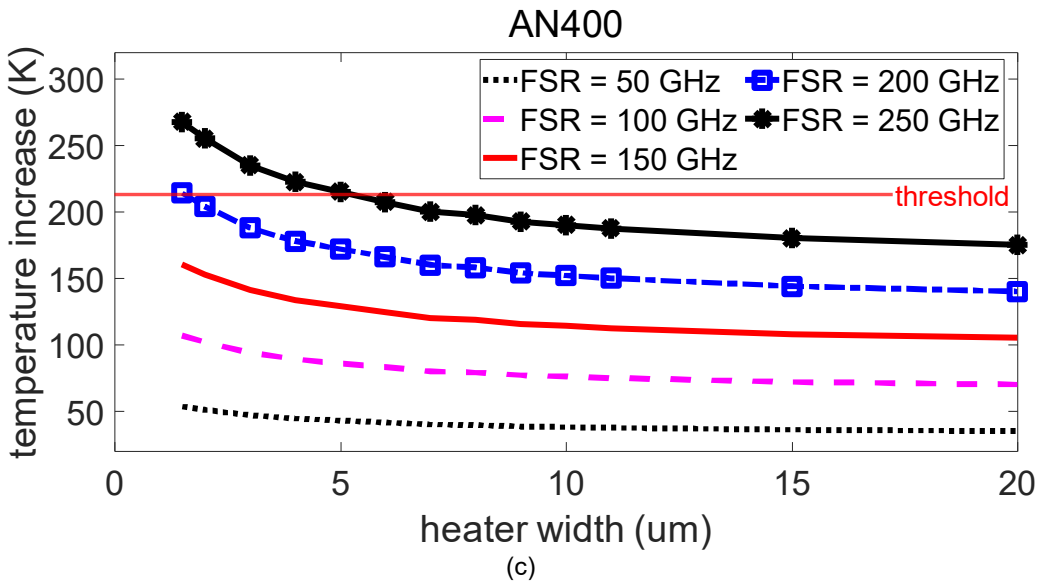

(c)

Fig. 4.7. Required temperature increases from the room temperature for ring resonators with different FSRs versus heater width for a) ADS, b) AN800, c) AN400 waveguides. Threshold lines define the safe operating limits for heaters.

As seen, the required heater temperature is scaled down as the heater is widened. The reason is that at a certain temperature a wider heater irradiates a larger area. Hence, for a certain tuning, a wider heater requires a lower temperature (see Fig. 4.5). Moreover, it is observed that the sensitivity of temperature to the heater width is reduced at larger heater widths. The reason is that once the heater is wide enough to cover the effective area in which the optical mode exists, its temperature pattern in the waveguide cross-section does not change significantly by further widening of the heater. Furthermore, one perceives that for a certain heater width, the temperature change is doubled as one doubles the FSR. This is explained by the fact that doubling the FSR doubles the required shift in the mode effective index; therefore, the temperature change in the heater needs to be doubled provided a linear relationship exists between the heater temperature and the mode effective index, which according to Fig. 4.7 is the case for the range of the applied temperature.

The threshold lines denote the maximum tolerable temperature for the heater (Cr in this case) beyond which the heater falls apart. This constraint along with the bend loss simulation results, limit the maximum FSR in the design. Putting together the results of bend and thermal simulations, the maximum FSR of the ring resonators made of the ADS, AN800, and AN400 waveguides are 200 GHz, 300 GHz, and 250 GHz, respectively. Also, it is observed from Fig. 4.7 that there are lower bounds on the width of the heater when the design aims at the highest reachable FSR, which is due to the failure temperature threshold. For instance, in Fig. 4.7(c), a ring resonator with the FSR of 250 GHz made of AN400 waveguide and 150 nm thick Cr heater can be designed only with heaters wider than 5 μm.

The steady-state simulations of the required electrical power to tune the ring resonators by the amount of one FSR reveal that the consumed power for a certain waveguide and heater structure remains unchanged regardless of the FSR. It can be elucidated by a comparison example. We assume P50, T50, P100, and T100 to be the tuning powers and the ultimate temperature shifts for a tuning by the amount of one FSR for the ring resonators with the FSRs of 50 GHz and 100 GHz, respectively. According to Fig. 4.7, doubling the FSR requires doubling the shift in temperature. Thus, T100 is twice T50. In the ring with the FSR of 50 GHz, if we inject another P50, the total tuning will be 100 GHz, and the total power will be 2P50. Thermal power is linearly proportionate to temperature shift; so, the temperature shift of the total power of 2P50 will be 2T50 or T100. It is observed that the heater temperatures are equal for the 50 GHz ring with 2P50 and a 100 GHz ring with P100. Electrical current in a certain heater is proportional to temperature. Thus, the two heaters need the same currents. The periphery of the ring

with the FSR of 50 GHz is twice the ring with the FSR of 100 GHz, so is its resistance. Hence, for constant electrical current, the electrical power of the ring with the FSR of 100 GHz will be half that of the ring with the FSR of 50 GHz. Thus, the power P100 is equal to 2P50/2 = P50. In other words, the required power for a tuning equal to one FSR is independent of the FSR. This comparison can be done for any other pair of rings with different FSRs.

Fig. 4.8 indicates the thermal power required to tune the ring resonators by the amount of one FSR for the three waveguides versus the width of the Cr heater. It is noted that the slope rises from almost zero to a constant amount as the width is increased. The reason is that at smaller widths there is a notable change in the required temperature as the width is increased (see Fig. 4.7); thus, the effect of the reduced temperature counteracts the width increase, causing the slope to remain close to zero. At larger widths, the required temperature is almost constant, and the effect of the width increase dominates, and the power keeps increasing.

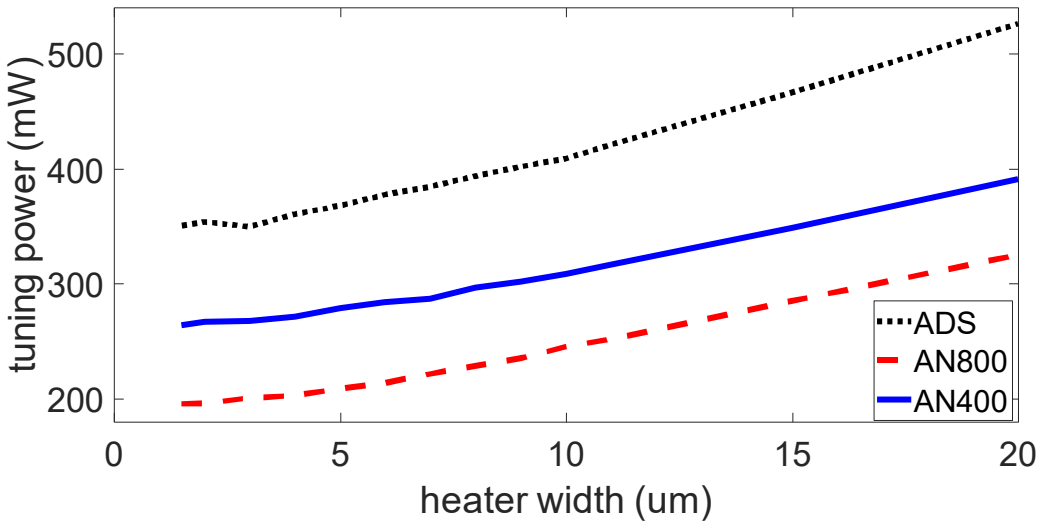

Fig. 4.8. Required tuning power for a wavelength shift by the amount of one FSR versus heater width.

Moreover, it is noted that AN800-based rings consume less power than the other two cases due to a closer position of the heater to the waveguide. Also, for a certain FSR, AN800-based rings have shorter periphery and therefore, smaller resistance, which further reduces the tuning power.

It is also seen that while AN400 and the ADS cases have the same distance from the heaters, AN400 consumes less power than ADS. The ADS waveguide has a mode spread over a lager area and thus, needs a higher temperature in the heater to heat up the area, ramping up the tuning power. Moreover, the ADS waveguide has larger periphery and thus, larger resistance, which also raises the tuning power.

As observed in Fig. 4.8, the smaller the width is, the less thermal power is required. From the power efficiency point of view, a narrower heater is more efficient. However, as illustrated in Fig. 4.7, the highest temperature at which the heater can safely operate, limits the selection of the heater width, which needs to be considered depending on the target FSR in a design. Hence, the optimum heater width differs for different FSRs. Thermal tuning efficiency is defined as the amount of dissipated thermal power per one FSR. The best thermal tuning efficiencies achieved from the simulations for the ADS, AN400, and AN800 waveguides are 350, 264, and 196 mW/FSR, respectively.

4.5.4 Scanning rate

The scanning rates of the ring resonators made of the three different waveguides versus heater width have been illustrated in Fig. 4.9. The simulation is performed by applying a time-dependent triangular heat rate waveform with its minimum at zero and its maximum being the maximum tolerable heat rate. This heat rate is equivalent to the

temperature of 496 °K at the heater and is unique for any waveguide-heater structure. This temperature is 10 degrees below the failing temperature of the Cr heater, acting as a safety factor. Acquired tuning rates of lower than 1 Hz were deemed unacceptable due to being too slow. It is noted that the scanning speed increases before being stable and ultimately descending. The reason for this behavior is explained by taking note of Fig. 4.7; the required temperature for a steady-state tuning decreases by widening the heater. It means that a wider heater receives a higher amount of power than the required one according to Fig. 4.7. As a result, the scanning rate is increased in a wider heater for a certain FSR. On the other hand, as the heater is widened, the required temperature remains almost constant; however, heat is spread in a larger area under the heater, and a smaller portion of the heat reaches the waveguide for tuning; thus, scanning speed is reduced at wider heaters as seen in Fig. 4.9. It is also noted that the scanning speed for AN800 is significantly higher than the other two cases. This is due to the heater being placed closer to the waveguide core, which causes a more rapid reaction of the waveguide to temperature fluctuations in the heater.

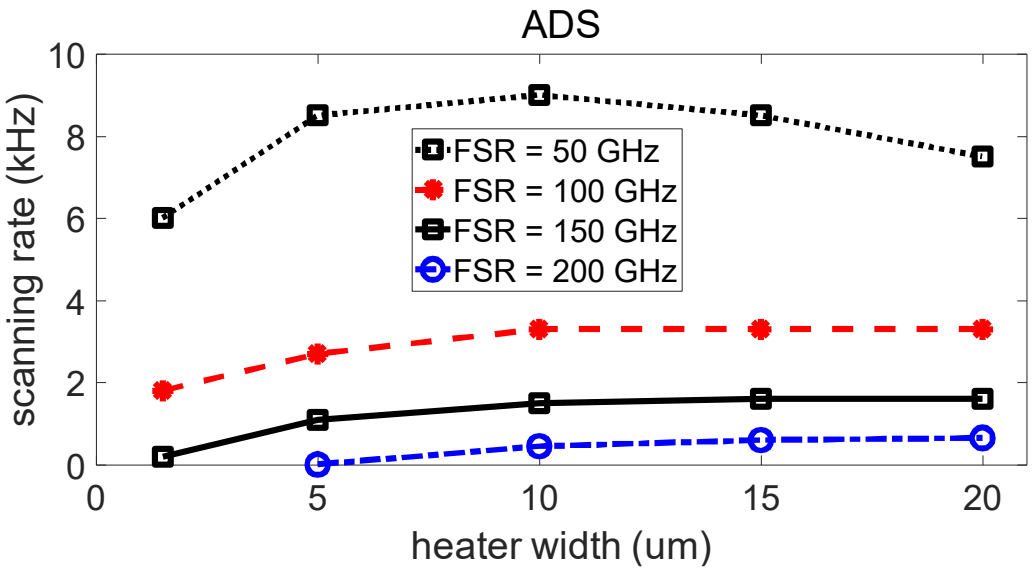
ADS
scanning rate (kHz)
heater width (um)
FSR = 50 GHz
FSR = 100 GHz
FSR = 150 GHz
FSR = 200 GHz
0
2
4
6
8
10
0
5
10
15
20

(a)

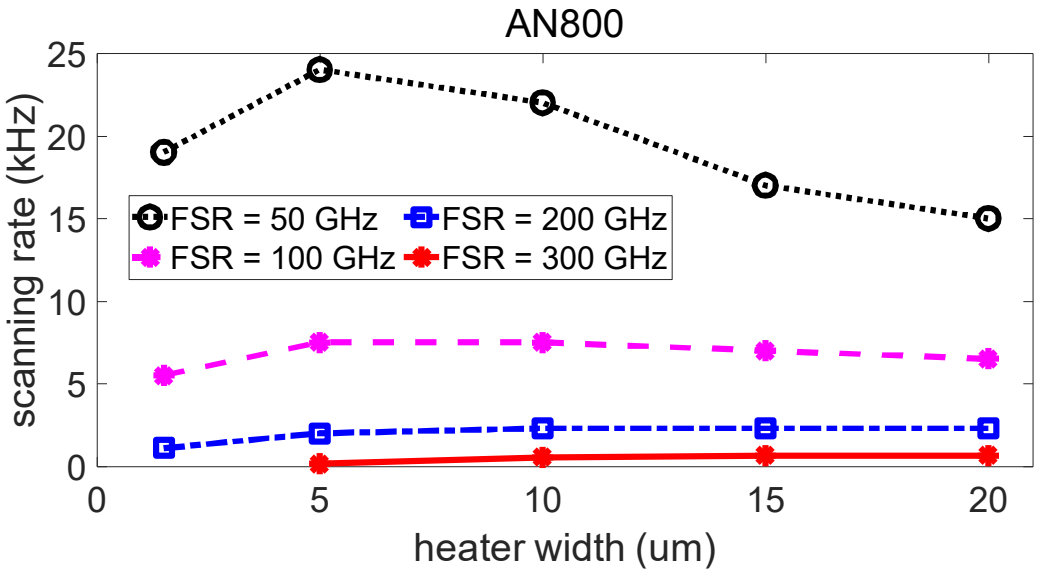
AN800
scanning rate (kHz)
heater width (um)
FSR = 50 GHz
FSR = 200 GHz
FSR = 100 GHz
FSR = 300 GHz
0
5
10
15
20
25
0
5
10
15
20

(b)

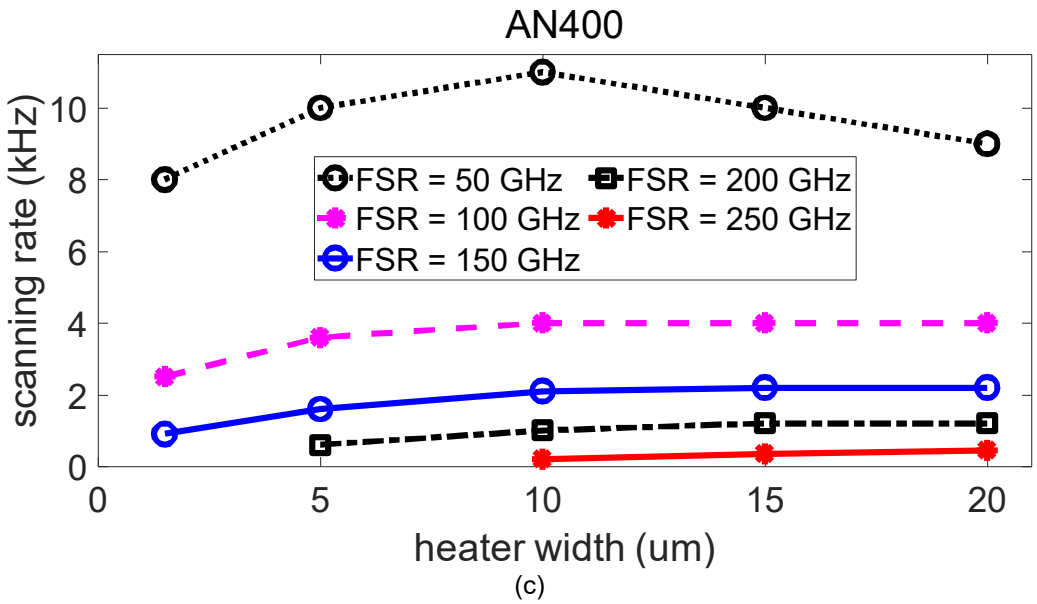

Fig. 4.9. Scanning rate versus heater width for a) ADS, b) AN800, c) AN400 waveguides. Markers indicate acquired data.

The data in Fig. 4.9 are the maximum possible scanning rates achieved by applying the triangular waveform whose peak is the maximum allowed thermal power. While some applications look for the fastest scan, others accept a lower scanning rate, which allows a specified scan to be conducted by a heat rate waveform with reduced peak power. Fig. 4.10 displays two heat rate waveforms applied in a 2D waveguide heater cross-section with 200 and 700 Hz, respectively. The ring resonator has an FSR of 200 GHz and is made of the AN400 waveguide equipped with a 5 μm wide Cr heater. The corresponding phase shift waveforms are also shown. Both phase shifts are 2π (equivalent to 200 GHz scan); however, the slower scan uses less peak power. Thus, a trade-off exists between scanning rate and applied thermal power for a certain scan.

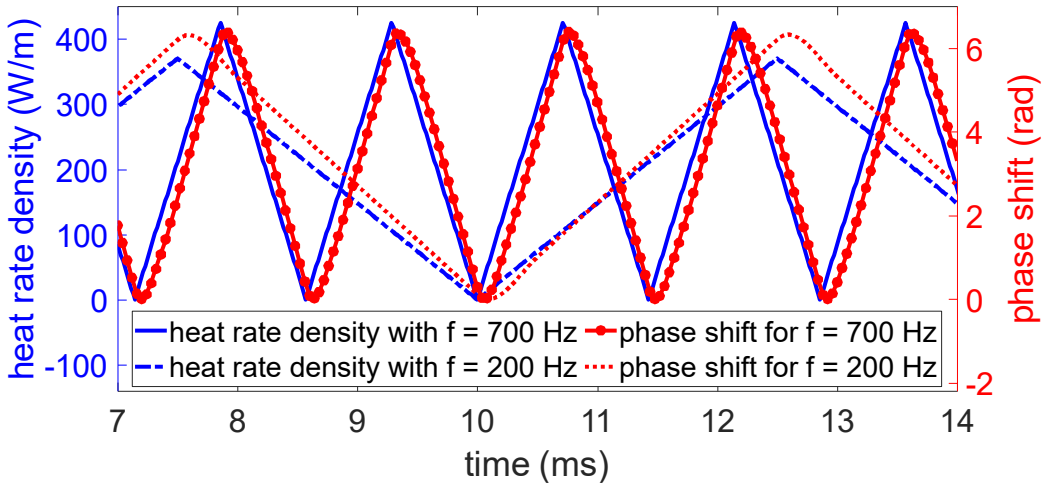

Fig. 4.10. Applied heat rate waveforms and corresponding phase shifts versus time for the AN400 waveguide equipped with a 5 μm wide Cr heater.

4.5.5 Sensitivity to over-heater cladding thickness

The sensitivity of the tuning power to the OHX thickness (see Fig. 4.5) was evaluated for the case of the AN800 waveguide for three different OHX values and demonstrated in Fig. 4.11. Slight fluctuations are most likely due to simulation errors. It is observed that a silica layer atop the heater slightly scales up the required tuning power. The likely reason for the difference is that when the heater is surrounded by silica, the heat spreads omnidirectionally; thus, more power is needed in the heater for tuning; in the case of heater exposure to air, heat spreads in silica easier through conduction than in air through convection, resulting in a need for less tuning power.

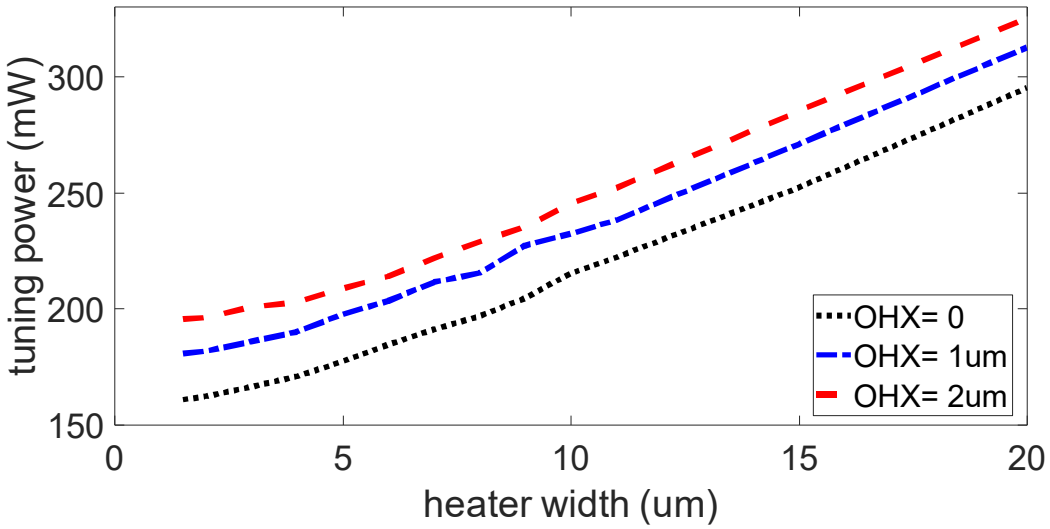

Fig. 4.11. Tuning power versus heater width for three different OHX values for AN800-based ring resonators.

4.5.6 Effect of heater material

The effect of heater material on performance is examined by comparing the amount of the required temperature rise and tuning power for the two practically used heaters introduced in Table 4.1. Similar to the Cr heater, simulations were performed to find out proper TOX values for the Al heater with negligible added optical mode loss in the presence of the heater. Fig. 4.12 illustrates the optical loss versus the vertical distance (TOX) between a waveguide core and Al heater that is 20 μm wide and 400 nm thick (see Table 4.1) for the ADS, AN800 and AN400 waveguides. The simulation steps are 0.5 μm. Acquired simulation results are then compared to those of the Cr heater and are presented in Table 4.3.

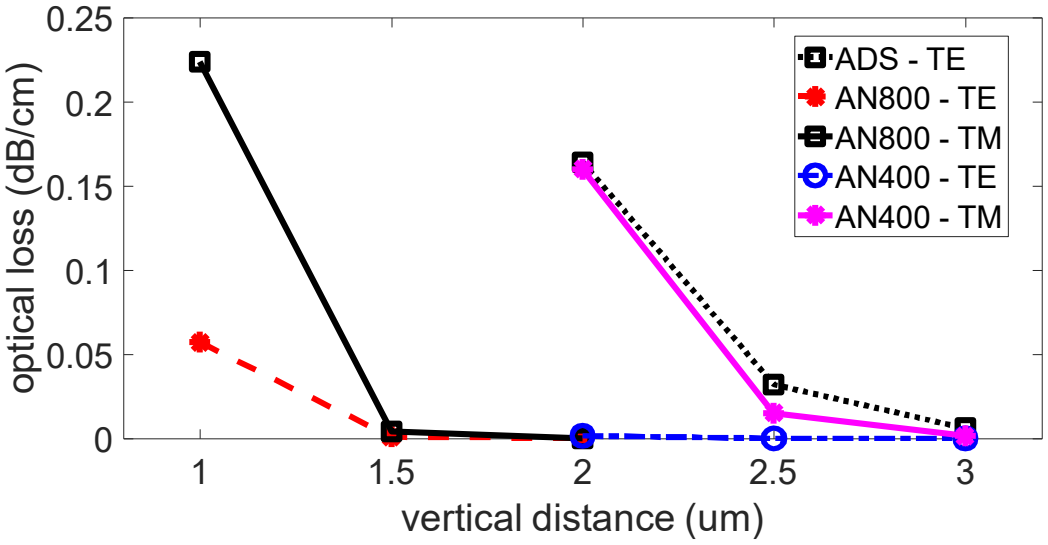

Fig. 4.12. Optical loss versus the vertical distance between a waveguide core and the Al heater (TOX) for the ADS, AN800 and AN400 waveguides.

Table 4.3. Optimum TOX values for Cr and Al heaters for negligible optical loss due to the heater presence while minimizing the vertical distance between the waveguide core and heater.

Heater / Waveguide	Cr	Al
ADS	3.5 μm	2.5 μm
AN800	2 μm	1.5 μm
AN400	3.5 μm	2.5 μm

It is noted that the TOX values differ for different heaters. Although the Al heater is thicker than the Cr heater (see Table 4.1), and aluminum has a larger absorption coefficient than chromium (see Appendix A), it can be placed closer to the waveguide. This is probably explained by the fact that the refractive index of aluminum is lower than chromium and is closer to the refractive index of the silica cladding. This makes it possible

for light not to be trapped inside the Al heater, reducing the optical loss. A comparison of the performances between Cr and Al heaters in ADS-based ring resonators is presented in Fig. 4.13.

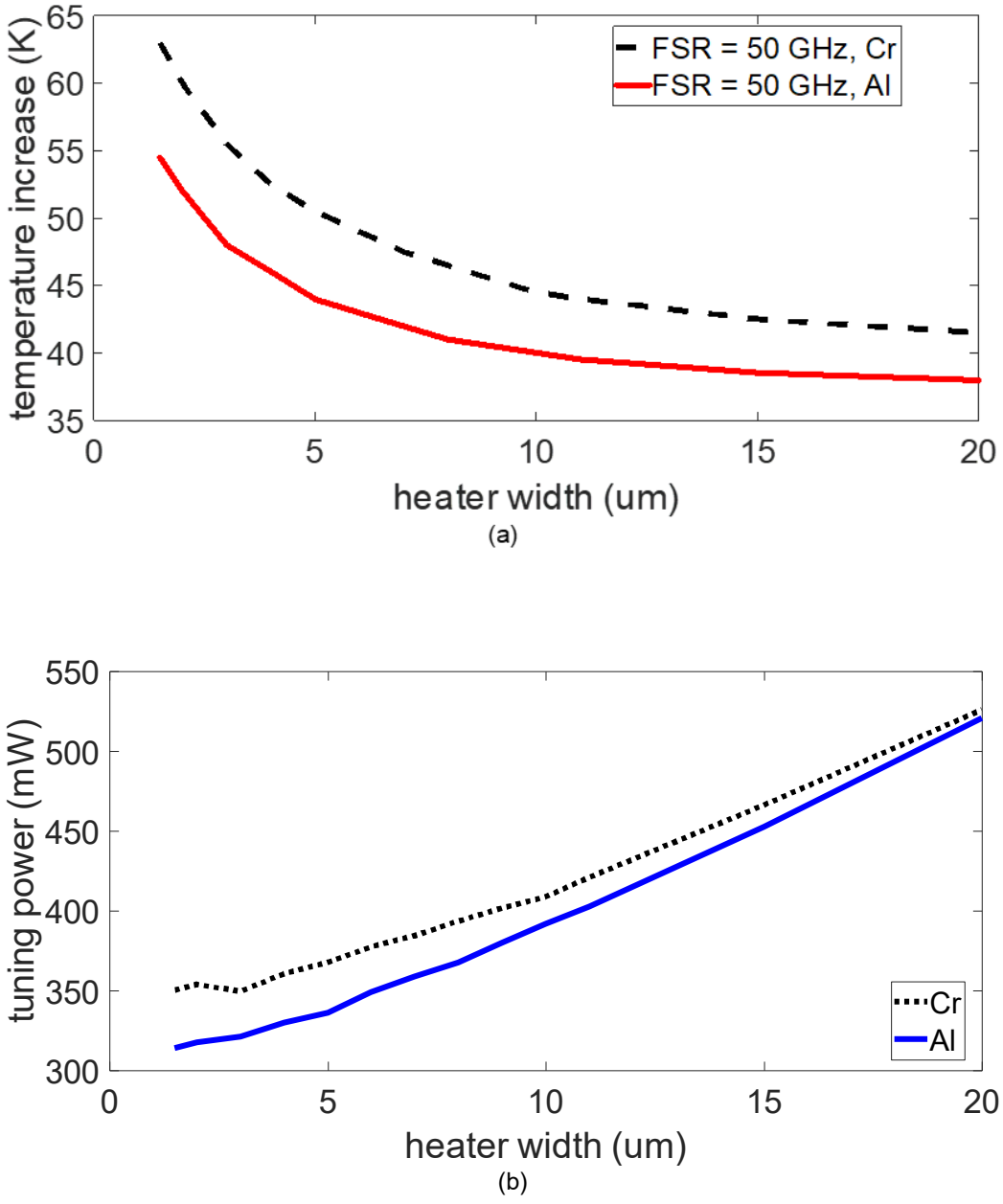

Fig. 4.13. The comparison of the Cr and Al heaters for ADS-based ring resonators; a) required temperature rise from the room temperature, b) consumed tuning power for a tuning by the amount of one FSR.

As seen in Fig. 4.13, the Al heater requires a lower temperature as it can be placed closer to the waveguide and as a result, less thermal power is needed for tuning. Although the Al heater has higher power efficiency than the Cr heater, due to its lower resistance, it draws higher electrical current from the power supply. For example, a Cr heater with a 20 μm width placed atop an ADS-based ring with an FSR of 50 GHz draws 23.67 mA current for a full FSR tuning, while an Al heater draws 180.88 mA current for the same tuning. Supplying such a large amount of current might cause technical problems for the electrical setup. Therefore, a heater made of aluminum which has lower resistivity than chromium, should be sufficiently small in cross-sectional area to increase the electrical resistance and overcome the problem of excessive current.

4.6 Discussion

To verify the simulations results, a structure that is already fabricated and tested by the manufacturer [81] is simulated. The ring resonator is made of the ADS waveguide with the FSR of 50 GHz and heated by a 20 μm wide Cr heater. TOX, and BOX values (see Fig. 4.5) are 8 μm each. There is no OHX layer added. The silicon substrate is 1.5 mm thick and placed above a 5 mm thick copper layer and the chip area is 16 x 16 mm^2. Boundary conditions are as stated already in the chapter. The expected experimental power for a tuning of 50 GHz is said to be no more than 600 mW. Our simulation results revealed a power consumption of 574 mW at 1574.5 nm and 584 mW at 1565 nm, which verifies the validity of the simulations.

The performed set of simulations characterized the thermal tunability of silicon nitride ring resonators including tunability extent, consumed electrical power and

scanning speed. The integration of the tunable ring resonator in the proposed spectrometer in Chapter 2 can monitor the C-band with the resolution of lower than 1 GHz. Bend simulations evaluated the extent of the FSRs that can be reached. The proper selection of the vertical position of a heater is key in reducing needed heater temperature and tuning power. For instance, an ADS-based ring resonator vertically distanced by the amount of 8 μm from a Cr heater with 20 μm width requires a temperature rise of 59.75 °K and a tuning power of 584 mW for a tuning by the amount of one FSR. It is while a TOX value of 3.5 μm reduces the needed temperature rise and tuning power 41.5 °K and 525 mW — a sizable reduction. Moreover, a proper selection of heater width can decrease tuning power while preventing the heater from falling apart due to thermal runaway. Reduced tuning power not only decreases total power budget on a chip; but also improves crosstalk performance.

It was also noticed that scanning speed reduces by increasing the FSR. This is important in designing a circuit to scan a wide band, consisting of a ring resonator as a fine filter integrated with an AWG as a coarse filter as elaborated in the introduction. Increasing the FSR of a ring resonator will reduce the number of required outputs in the AWG. As a result, the implementation of the PIC will become easier, the chip will occupy less footprint, and the overall cost will scale back. However, the scanning speed of the wavelength band will be lowered.

4.7 Summary of the main findings

The characterization of the thermal tuning of silicon nitride ring resonators made of practically used waveguide structures was studied in the C-band. The study included

the optical simulation of the waveguide, state-state and time-dependent thermal simulations, to find out the maximum tunable FSR, required tuning power, and tuning speed. The effects of the OHX thickness, and the material of the heater on performance were also evaluated. The simulations were carried out by considering the FPV errors to obtain reliable results. A good agreement between the simulation and the measurement performed by the manufacturer proved our simulations valid.

Chapter 5 Arrayed Waveguide Grating Design

5.1 Introduction

The design of the arrayed waveguide grating (AWG) according to the requirements of the incoherent weighted summation method and maximum tunable ring free spectral range (FSR) is carried out in this chapter. First, a theory of the AWG and its operation mechanism is provided. Then, the design specifications for the required AWG are determined. In the following, the method to design the AWG is explained and its simulation results are presented. Next, the overall performance of the spectrometer including the ring resonator and AWG in terms of its industry defined requirements is evaluated. Finally, the chapter is summarized.

5.2 Theory

The AWG is a dispersive on-chip component used for (de)multiplexing light into different wavelengths [27], [59], [97], [127], [128]. It consists of one (or more) input waveguides, arrayed waveguides, output waveguides, and two free propagation regions (FPR) where the first FPR is placed between the input and arrayed waveguides, and the second FPR is between the output and arrayed waveguides. Light enters the AWG from the input. It then spreads in the first FPR and illuminates the arrayed waveguides. The arrayed waveguides are arranged from the shortest to the longest, each of which being different from the adjacent waveguides by a (usually) constant amount in length. This length difference causes the light traversing in each waveguide gain a different phase shift. The phase shift difference is represented as:

$$\Delta\varphi = N_{eff}.\left(\frac{2\pi f}{c}\right).\Delta L \tag{5.1}$$

in which, N_{eff}, f, c, and ΔL are the effective mode index, frequency, light speed in the vacuum, and the length difference between adjacent arrayed waveguides. At the entrance of the second FPR, the light coming out of the arrayed waveguides forms a phased array. The phase shift arrangement of the array elements directs the light towards a certain angle with respect to the normal to the array axis, illuminating the output waveguides interface. Varying the frequency of light alters the array phase shift and so the beam is moved along the output interface. The amount of the frequency change required for the beam to move from the center of one output waveguide to the center of the adjacent one is the AWG channel spacing. The total output response of the AWG is obtained by computing the overlap integral of the electrical fields of the mentioned output beam and the fundamental mode of a specified output waveguide at the output interface.

The output beam is calculated by taking the endpoints of the arrayed waveguides as point sources illuminating the output waveguide interface. It is then revealed that the output beam versus angular position is related to the sources versus spatial position by Fourier transform. As the input waveguide illuminates the first FPR ununiformly, the amplitude pattern of the arrayed waveguides is maximum in the middle and diminishes towards either end. On the other hand, its phase experiences a linear change according to (5.1). Hence, the Fourier input is an array with bell-shaped amplitude and a linear phase distribution. The resultant output is also bell-shaped in its passband with its central angle being shifted because of the array phase shift. As such, the output beam moves along angular position by varying frequency; thus, at a certain output spatial observation point,

the output beam demonstrates a bell-shaped passband profile versus frequency. This shows that the AWG frequency response at any output waveguide is not uniform; and a technique is required to resolve the uneven channel profile problem.

5.3 Design specifications

Among different available techniques to overcome the uneven AWG channel profile, which are described in Chapter 2, the incoherent weighted summation technique was opted for the spectrometer because of a simpler optical architecture, a flat unity on-resonance response regardless of nonuniformity in the AWG channel profile envelope, no need for hand-overs between different channels and consequently, no need for the ring resonator FSR to be an integer multiple of AWG channel spacing, and finally no compromise between the flatness of the response and neighboring resonant frequency crosstalk. It was noted that the ring resonator FSR must be as large as possible for the best crosstalk performance. The simulations in Chapter 4 revealed that silicon nitride ring resonators can have tunable FSRs of up to 300 GHz. Hence, the AWG design in this chapter is carried out considering the ring resonator FSR. The AWG channel spacing needs to be small enough so that neighboring resonant frequencies do not cause significant crosstalk. Based on the results achieved in Chapter 2, the channel spacing between the adjacent channels is set to 100 GHz, which is one third of the ring resonator FSR. Also, the intersections points between adjacent channel profiles are chosen to be at -3dB, which is well above noise level. While this is not the only choice for the AWG design, it meets the requirements specified in Chapter 2 to achieve a flat on-resonance response as the resonant frequency is tuned. Moreover, the channel spacing of 100 GHz

is larger than the case studied in [57] and thus, is more robust against phase error crosstalk. Therefore, the goal is to conduct an AWG design with channels that are spaced by 100 GHz and intersect at -3dB power transmission lower than their peaks.

5.4 Design

The design needs the adjacent channel profiles to overlap at a point that is -3dB lower than the peaks, which is not possible in a conventional AWG whose input and outputs are identical at the FPR interfaces. One method to overcome this problem is using multiple AWGs in parallel as stated in [57]. For instance, two parallel AWGs where each has a channel spacing of 200 GHz and -3dB bandwidth of 100 GHz and are different only in the position of their inputs so that when the two AWGs are combined, they make interleaved channel profiles with the channel spacing of 100 GHz and intersect at the level -3dB below their peaks. This technique requires multiple (2 or more) AWGs in parallel, making the design and implementation more complicated. A power splitter is required to divide light equally into the number of parallel AWGs. Moreover, the footprint is also scaled up. As a result, the insertion loss and fabrication cost are ramped up. In this chapter, the parallel AWGs are consolidated into one AWG with an increased input waveguide width to achieve the desired channel profile arrangement, which reduces the number of optical components, footprint and cost. It is noted that unequal input and output waveguide widths results in extra insertion loss in AWG transmission because of mode mismatch between each output waveguide and the stigmatic image of the input waveguide. However, an increased input waveguide width, reduces the number of required arrayed waveguides due to light being spread in a smaller angle in the first FPR

and thus, illuminating a smaller number of arrayed waveguides. A reduced number of arrayed waveguides reduces the overall AWG footprint and shortens the lengths of the arrayed waveguides, improving insertion loss performance.

5.4.1 Waveguide

The AN400 waveguide (described in Chapter 4) is used as the input, output, and arrayed waveguides of the AWG as it is single mode and no higher order modes are generated in the arrayed waveguides and thus, inter-mode crosstalk is absent in the design. The width and height of the waveguide are 1 μm and 400 nm, respectively. It has a declared intrinsic loss of 0.3 dB/cm. The input, output, and arrayed waveguides are widened with linear tapers at the FPR interfaces to minimize the insertion loss and increase the channel bandwidth. The design is performed for the TE polarization in accordance with the previous simulations. Photon Design's EPPIPROP and FIMMPROP tools are used for simulation. EPPIPROP simulates the AWG as a whole and computes the channel profiles for each output. FIMMPROP is used to simulate the tapers to compute the fundamental TE mode loss within the tapers and the coupling between the neighboring waveguides. As the loss value for the fundamental TE slab mode in the FPR regions was not available, in EPPIPROP simulations, the AN400 waveguide loss is assumed to be a higher amount of 0.4 dB/cm to increase the reliability of simulation results. The fixed radius AWG layout in EPPIPROP was selected for the design. It should be noted that this AWG design requires a ring resonator with the FSR of 300 GHz. The simulations in Chapter 4, revealed that only the AN800 waveguide can achieve this FSR. Thus, a transition in the waveguide thickness from the ring resonator built with the AN800

waveguide to the AWG built with the AN400 waveguide is required — it is done by a vertical tapering of the AN800 waveguide to reduce its thickness to the same level of the AN400.

5.4.2 Nonuniformity

There are multiple design approaches for an AWG. The adopted method in this thesis is the one introduced in [97]. As the channel spacing between the adjacent outputs is 100 GHz, 44 output waveguides enable the full coverage of the C-band. The output waveguides need to be placed as close as possible to minimize the maximum angle of the beam illuminating the output waveguides. It is because the outer channel profiles experience the aberration effect and have larger side lobes than the inner channel profiles, degrading their crosstalk performances [129], [130], [131], [132], [133], [134], [135]. Reducing the aberration effect is advantageous in better suppressing the crosstalk caused by neighboring resonant frequencies in outer channel profiles. To reduce the aberration effect, the maximum beam angle illuminating the output interface needs to be reduced. Reducing the maximum output beam angle also reduces the nonuniformity in the envelope of the output channel profiles. The reason is that outer channels have extra insertion loss than inner channels in a cyclic AWG. The insertion loss difference between the middle channel and the outer channels on either side of the output array can be up to 3 dB if the AWG FSR is the same or smaller than the length of the total design band. In that case, two beams spaced by the amount of one AWG FSR illuminate two symmetric points within the output array with respect to the middle point of the output array, simultaneously. The simultaneous illumination of two output points halves the received

power on either output channel (a 3 dB reduction) with respect to the case where only one beam illuminates the middle channel of the output array. The maximum nonuniformity in this design is set to 1 dB, so that multiple output ports are not illuminated concurrently. This also ensures that the aberration effect is reduced compared to the case of 3 dB nonuniformity.

5.4.3 Input and output waveguides

Fig. 5.1 depicts the schematic view of the output waveguides at the FPR interface. As already stated, output waveguides must be placed as close as possible. However, they must be far enough so that neighbor coupling becomes negligible in the non-tapered area. It can be understood from Fig. 4.3 that the AN400 waveguide has higher mode confinement than the ADS waveguide. Also, Fig. 3.6 indicates that the ADS waveguide has negligible coupling at the gap of 3 μm, as the two lowest order super-modes have almost identical values. This means that at the gap of 3 μm, a more confining waveguide (AN400) has negligible coupling as well. Hence, the center-to-center spacing of the output waveguide array, which is the summation of the gap and the width of the waveguide, is set to 4 μm. The gap shown in Fig. 5.1 is set to 300 nm, which is the minimum gap size allowed by the manufacturer. The aim of the tapers is to maximize the output power and channel bandwidth. The taper must be long enough to minimize the insertion loss. However, too long a taper would cause neighbor coupling. Therefore, a trade-off exists in the design of the taper. FIMMPROP simulations, which are based on EME method, were conducted to calculate the length of the taper. With a length of 20 μm, the taper — starting

from 3.7 μm and ending at 1 μm — showed negligible neighbor coupling and insertion loss.

As there is only one input waveguide, the above simulations are not required for the input waveguide. The length of the input taper is determined solely by considering the insertion loss. The taper length depends on the input waveguide width at the FPR interface. Once it is determined, the taper length is then computed.

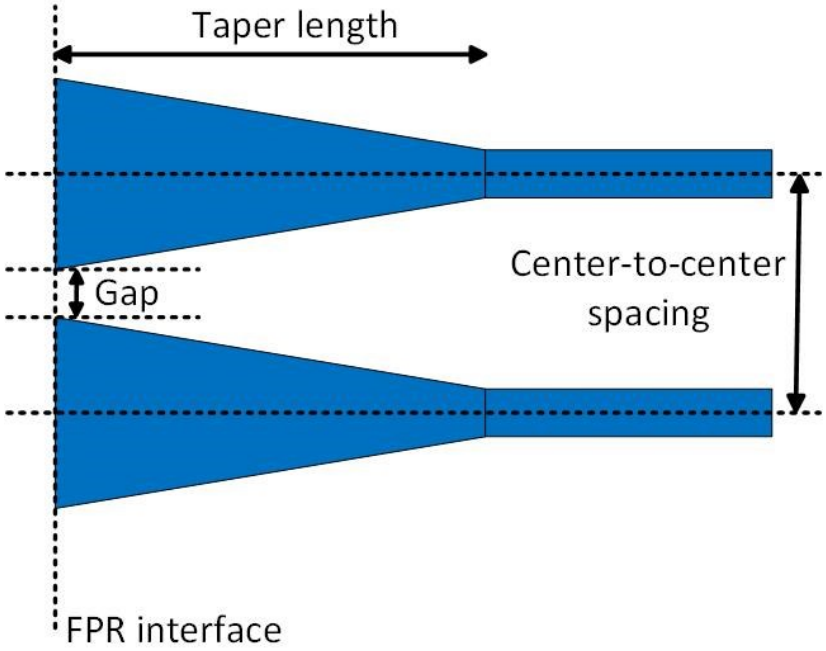

Fig. 5.1. Schematic view of the tapered arrayed or output waveguides at the FPR interface.

5.4.4 Arrayed waveguides

The schematic view of the arrayed waveguides is also the same as Fig. 5.1. The gap is 300 nm, and widened waveguides at the FPR interfaces are to minimize the insertion loss. Similar to output waveguides, the center-to-center distance between

arrayed waveguides must be minimized so that the angle between the output cyclic beams is maximized [97]. At the same time, the distance must be large enough to prevent undesired neighbor coupling. Ideally, coupling between arrayed waveguides should be zero to prevent manipulation of their amplitude and phase distributions. For this design, the maximum allowed normalized power coupling between adjacent arrayed waveguides (outside the tapered regions) is 0.001. EPPIPROP calculates the longest length of the arrayed waveguides and determines whether the worst neighbor coupling remains within the desired limit. If the neighbor coupling is unsatisfactory, a new center-to-center spacing needs to be used in the design until the neighbor coupling limit is satisfied. After several try and error, the center-to-center spacing is set to 4.3 μm. Thus, the width of each arrayed waveguide at the FPR interface is 4 μm. The length of the linear taper is computed similar to output waveguides and is 20 μm.

5.4.5 Rowland circle and Arrayed Waveguide Grating order

As instructed in [97], the effective mode width (w_e) of the arrayed waveguide at the FPR interface is computed. The width in this thesis is 4 μm as already stated. The fundamental TE mode profile of the waveguide is computed by FIMMWAVE. The main component of this mode, which is horizontal electric field is extracted. The data is plugged in the following relation:

$$w_e = \frac{\int_{-\infty}^{+\infty} E(x)^2 dx}{E_{max}^2} \tag{5.2}$$

where $E(x)$, and E_{max} are the horizontal component of the fundamental TE mode, and its maximum value, respectively. The corresponding MATLAB code is provided in Appendix

B. Next, the width of the far field envelop of the output frequency response is computed as:

$$\theta_0 = \frac{\lambda}{N_{FPR}.w_e.\sqrt{2\pi}} \tag{5.3}$$

where λ, and N_{FPR} are the design wavelength (center wavelength of the C-band in this case) and the fundamental TE slab mode effective index, respectively. Then, θ_{max} , which is the maximum allowed angle of the output beam is computed as:

$$L_u(dB) \approx 8.7 \times \theta_{max}^2/\theta_0^2 \tag{5.4}$$

where $L_u(dB)$ is the nonuniformity, which is determined in the previous part. There are 44 output waveguides in this design. Thus, with the computed θ_{max} and computing the length of the output array consisting of 22 elements (half of the output array as θ is symmetric with respect to 0), the approximate value of the Rowland mount (R_m) is achieved. The radius of the Rowland circle (R_c) is half that of the Rowland mount. The length difference between adjacent arrayed waveguides (ΔL) is then calculated by:

$$\Delta L = \frac{D.N_{FPR}.d_a.f_0}{R_m.N_g} \tag{5.5}$$

where d_a, f_0, and N_g are the center-to-center spacing od arrayed waveguides, center frequency of the design band, and the group index of the standard-sized arrayed waveguides (AN400 with the width of 1 μm). The parameter D is called the AWG dispersion and defined as

$$D = \frac{d_o}{Ch\_S} \tag{5.6}$$

where d_o, and Ch_S are the output waveguide center-to-center spacing, and channel spacing, respectively. The approximate AWG order is computed from ΔL using

$$m = \frac{N_{eff}.\Delta L}{\lambda_0} \tag{5.7}$$

The achieved value for m then rounded to the nearest integer value, which becomes the actual value used in the design. The slight change applied to m has a negligible effect on the nonuniformity. The parameters are then input in EPPIPROP to build the AWG layout, run it, and ultimately visualize the output channel profiles. The bend radius in the arrayed waveguide region must be large enough so that the mode traversing within it does not experience a change in the effective index. This ensures that scattering loss in the arrayed waveguide region is minimized. The bend radius of this design is 800 μm. After inserting the parameters, if the layout is not generated, “star coupler spacing” and “star coupler tilt” must be tuned to eventually a valid layout is generated. The input waveguide is initially set to be the same as the output waveguide at the FPR interface to minimize the mode mismatch loss between the input and output. The number of meshes used in input, output, and arrayed waveguides regions are increased in multiple simulations until the results converge. After running the simulation, from the visualized output response, the channel spacing is measured, and adjustments in R_c are made to attain the desired channel spacing (100 GHz). The FSR is computed using:

$$FSR = \frac{c}{N_g.\Delta L} \tag{5.8}$$

The calculated FSR of the AWG is 64.8 nm, — almost twice as large as the C-band length — confirming that the output waveguides are not illuminated by more than

one beam, concurrently. It is noted that the -3dB bandwidth of channel profiles is less than 100 GHz. Thus, in the next step, the width of the input waveguide at the FPR interface is increased so much so that the bandwidth reaches 100 GHz. The achieved input width is 8 μm. This width is larger than the 3.7 μm wide output waveguides and causes an increase in the insertion loss due to the mode mismatch. However, the wider input waveguide, directs light in a smaller angle in the first FPR, and as a result, fewer arrayed waveguides are needed to capture most of the light. A lower number of arrayed waveguides enables shorter arrayed waveguides and makes the overall AWG layout smaller. This reduces the insertion loss and fabrication cost.

The number of arrayed waveguides must be sufficiently large so that the envelope of illuminated arrayed waveguides gradually rather than abruptly reaches zero. This is important in reducing the side lobe levels in output channel profiles and improving the crosstalk, because output channel profiles are related to the envelope of arrayed waveguides by Fourier Transform. The number of arrayed waveguides, however, should not be too large. Otherwise, the layout would be unnecessarily large and insertion loss would be ramped up. To find the optimum number of arrayed waveguides, simulations are conducted with different numbers of arrayed waveguides and captured power percentages by arrayed waveguides at the interface of the first FPR and arrayed waveguides are observed. Fig. 5.2 illustrates the power percentage captured by arrayed waveguides versus the number of arrayed waveguides. It is observed that the captured power saturates at circa 95 arrayed waveguides. As such, the number of arrayed waveguides in this design is set to 95 where more than 99% of the incident light is captured by arrayed waveguides.

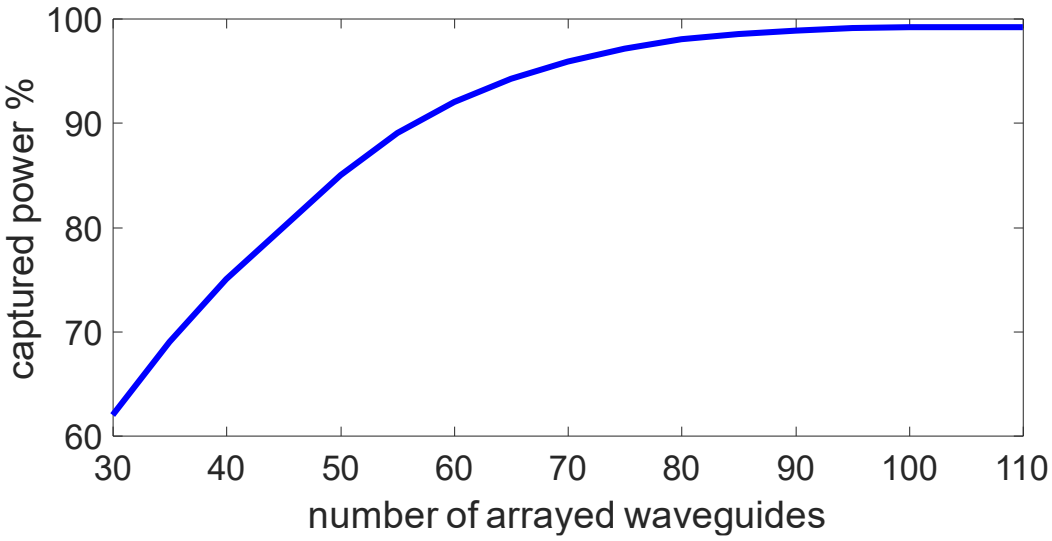

Fig. 5.2. Captured power percentage versus the number of arrayed waveguides.

Fig. 5.3 shows the intensity of light at the entrance of arrayed waveguides with 95 waveguides. The intensity of light is gradually reducing to zero at a Gaussian-like pattern indicating the enlargement of the input waveguide fundamental mode in the free space. The arrayed waveguides capture more than 99% of the light illuminating them. Once the optimum number of arrayed waveguides is determined, the AWG layout may become smaller in size further. Finally, neighbor coupling is computed for arrayed waveguides for the finalized design to ensure the coupling remains below the specified limit of 0.001 for the design. It is performed in EPPIPROP, and the result indicated that arrayed waveguides are far enough. In case a result is not satisfactory, a new value for arrayed waveguides spacing and width at the FPR interface must be chosen and the design process needs to be repeated. The values of the parameters used in the design are presented in Table 5.1. The layout of the AWG is indicated in Fig. 5.4. Its total area is 2.4 x 2.7 mm^2.

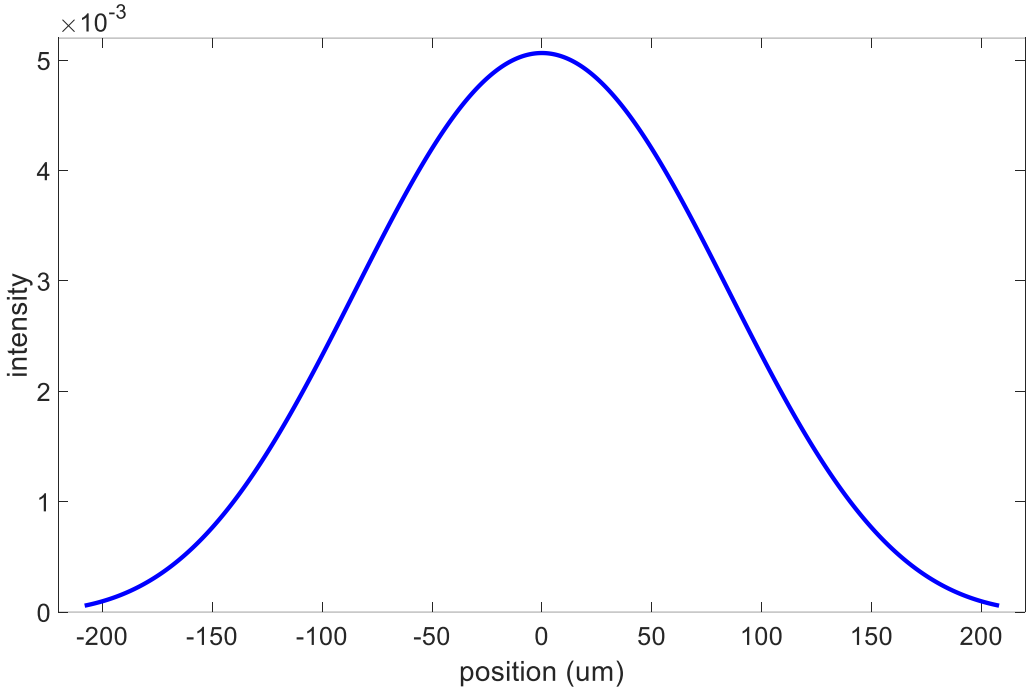

Fig. 5.3. The entrance interface of arrayed waveguides illuminated by the input waveguide. The number of waveguides are 95.

Table 5.1. Specifications of the AWG

input waveguide width at FPR interface	8 μm
output waveguide width at FPR interface	3.7 μm
arrayed waveguide width at FPR interface	4 μm
gap	0.3 μm
output waveguide center-to-center spacing	4 μm
arrayed waveguide center-to-center spacing	4.3 μm
output/arrayed waveguide taper length	20 μm
bend radius of arrayed waveguides	800 μm

design wavelength	1.5475 μm
Rowland circle radius	745 μm
number of arrayed waveguides	95
star coupler tilt	188°
star coupler spacing	2200 μm
AWG order	20

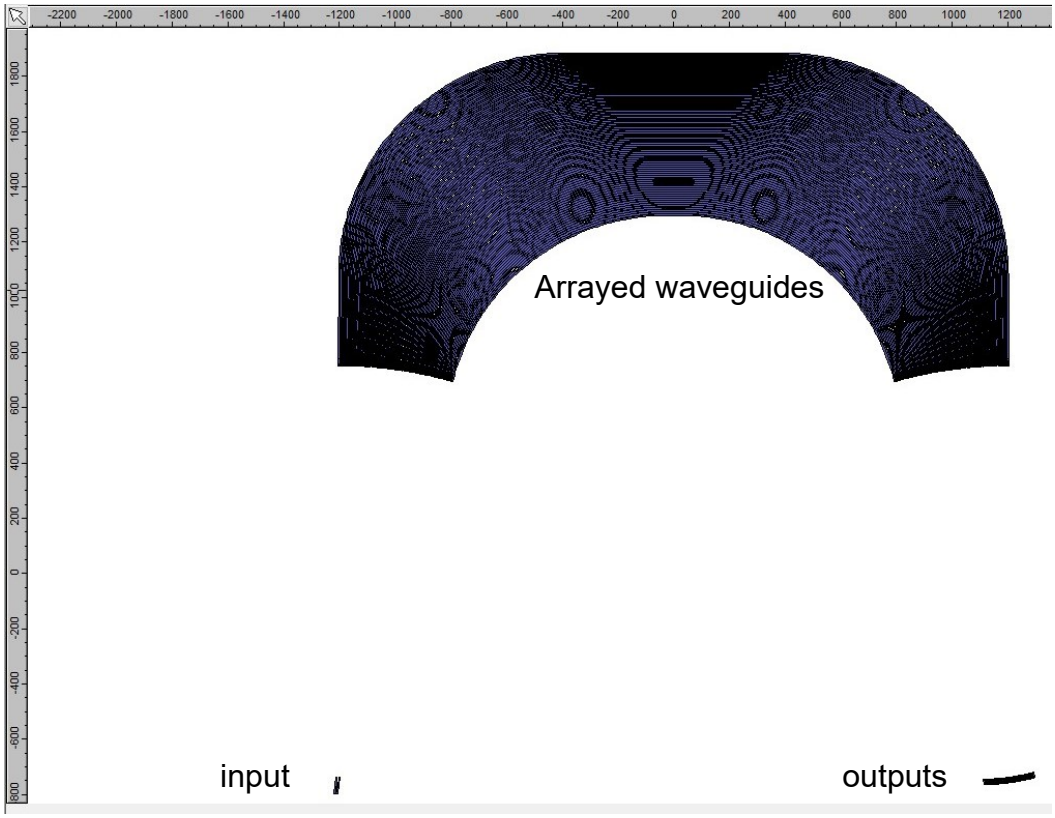

Fig. 5.4. The AWG layout. Dimensions are in μm.

Fig. 5.5 shows the simulated output channel profiles of the designed AWG versus the frequency normalized to the central frequency of the C-band. The peak insertion loss

and background crosstalk are 3.3 dB and 33 dB, respectively. It should be noted that the achieved crosstalk does not take in the phase error effect. The channel spacing is 100 GHz and the channel profiles intersect at -3dB, fulfilling the bandwidth requirement of 100 GHz for each channel.

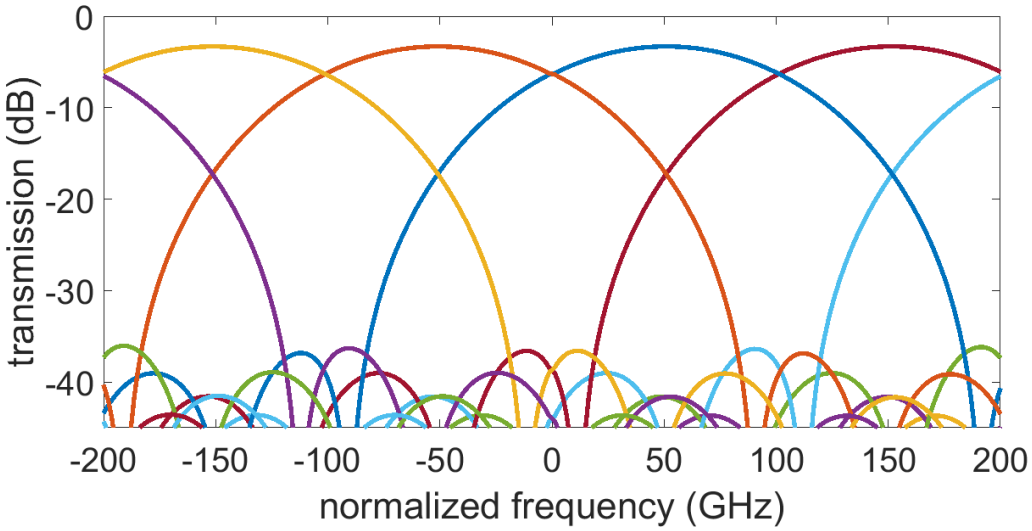

Fig. 5.5. The output frequency response of the designed AWG.

To demonstrate the effect of the widened input waveguide, several parameters of the designed AWG are compared to those of a conventional AWG whose input and output waveguide widths are identical at FPR interfaces and are equal to 3.7 μm. The results are demonstrated in Table 5.2. It is seen that although the conventional AWG has better peak insertion loss due to the identical input and output waveguides, it cannot achieve the required bandwidth for the same 100 GHz channel spacing. Also, the number of arrayed waveguides in the designed AWG is significantly lower, resulting in a more compact layout.

Table 5.2. Comparison between the conventional and designed AWGs

parameters	Conventional AWG	Designed AWG
channel spacing	100 GHz	100 GHz
-3 dB bandwidth	50 GHz	100 GHz
number of arrayed waveguides	195	95
peak insertion loss	2.27 dB	3.3 dB
footprint	3.5 x 5 mm^2	2.4 x 2.7 mm^2

5.5 Spectrometer performance

In this section, the performance of the spectrometer (see Fig. 2.12) is evaluated by applying the incoherent weighted summation technique to the combination of a ring resonator with a resolution of lower than 1 GHz, tunable over its FSR of 300 GHz, and the designed AWG. The VCP of the AWG, and overall spectrometer frequency response, generated for three resonant frequencies, are demonstrated in Fig. 5.6. The corresponding MATLAB code is attached to Appendix B. The crosstalk with respect to adjacent resonant frequencies of the ring resonator is -40dB. It is deduced from the figures that for the designed AWG, the neighboring resonant frequency crosstalk is very high for ring resonator FSR values below 100 GHz. Crosstalk performance improves by increasing the ring resonator FSR. Increasing the ring resonator FSR not only improves the crosstalk but also scales down the number of required AWG outputs (for a certain crosstalk performance) and subsequently photodetectors, which reduces the footprint, insertion loss, and cost. Fig. 5.7 displays the spectrometer frequency response for

different ring resonator tuning frequencies. A flat on-resonance frequency response is achieved. 3D plots of the VCP and spectrometer frequency response versus observation frequency together with resonant frequency of the ring resonator are depicted in Fig. 5.8. It is noted that shifting resonant frequency, moves the peaks of the VCP as well as spectrometer response. Positions and intensities of neighboring resonant frequencies causing crosstalk are clear in Fig. 5.8(b).

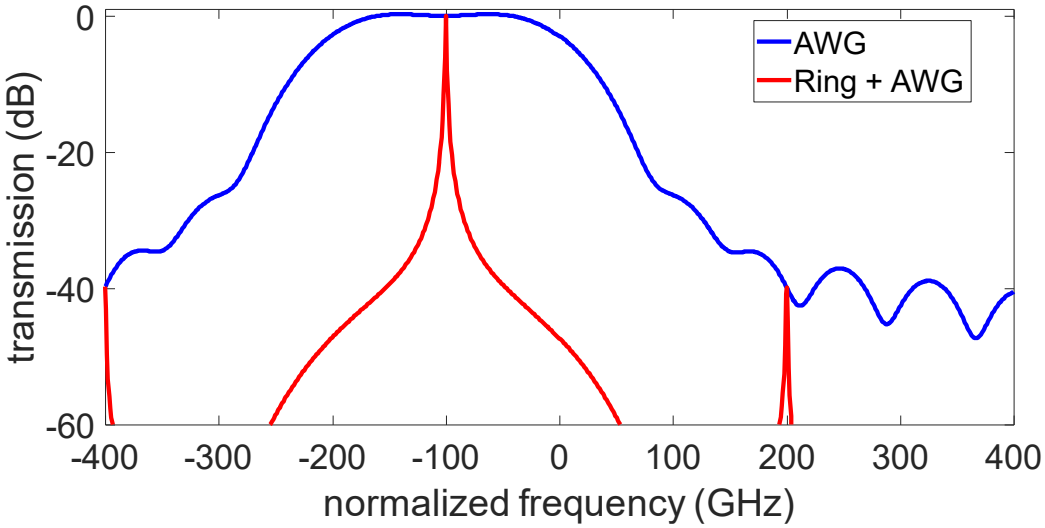

(a)

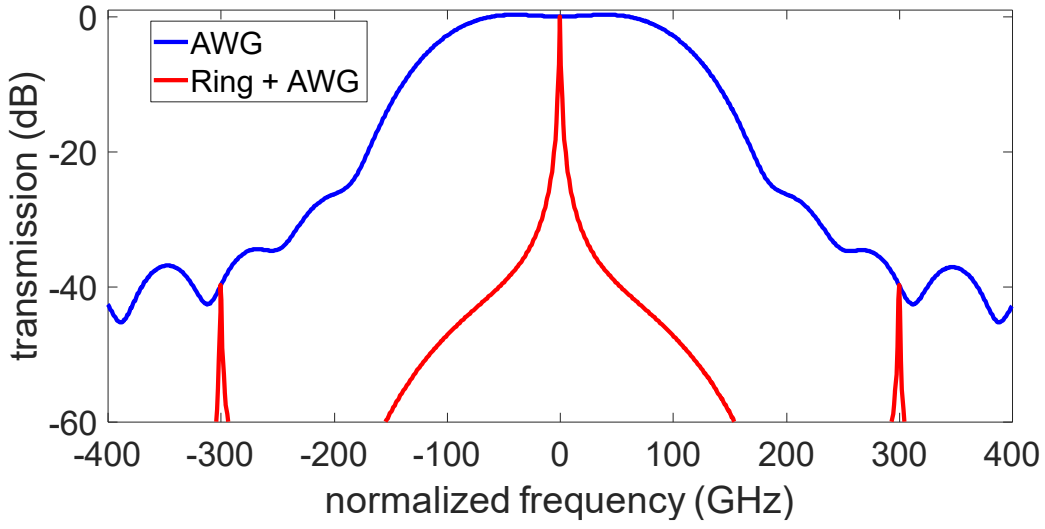

(b)

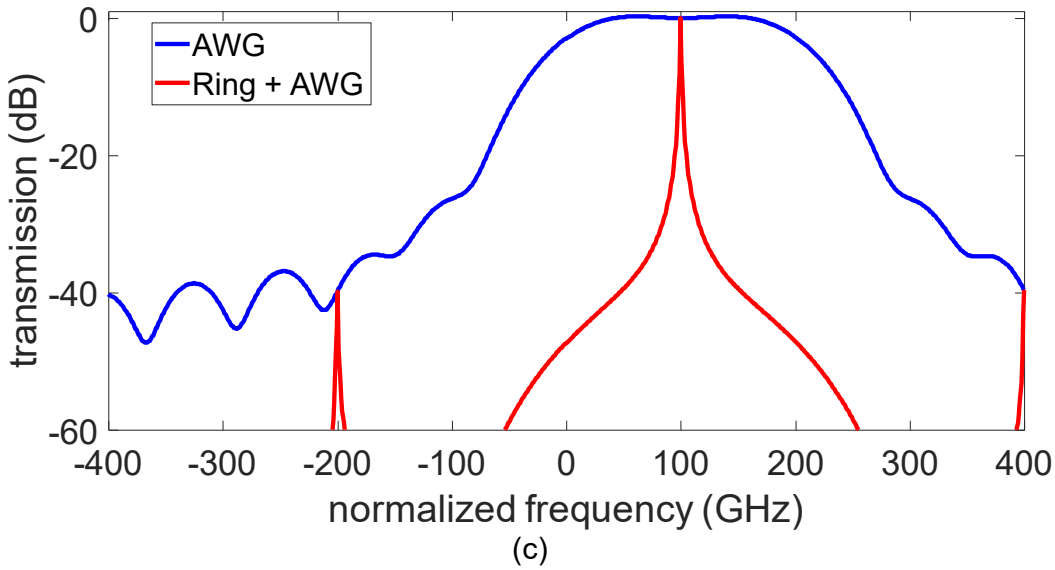

Fig. 5.6. The generated VCP (blue) and overall spectrometer response (red) for three different ring resonator resonant frequencies with respect to center frequency of the C-band; a) -100 GHz, b) zero, c) +100 GHz. The FSR of the ring resonator is 300 GHz. The channel spacing and -3dB bandwidth of the AWG are both equal to 100 GHz.

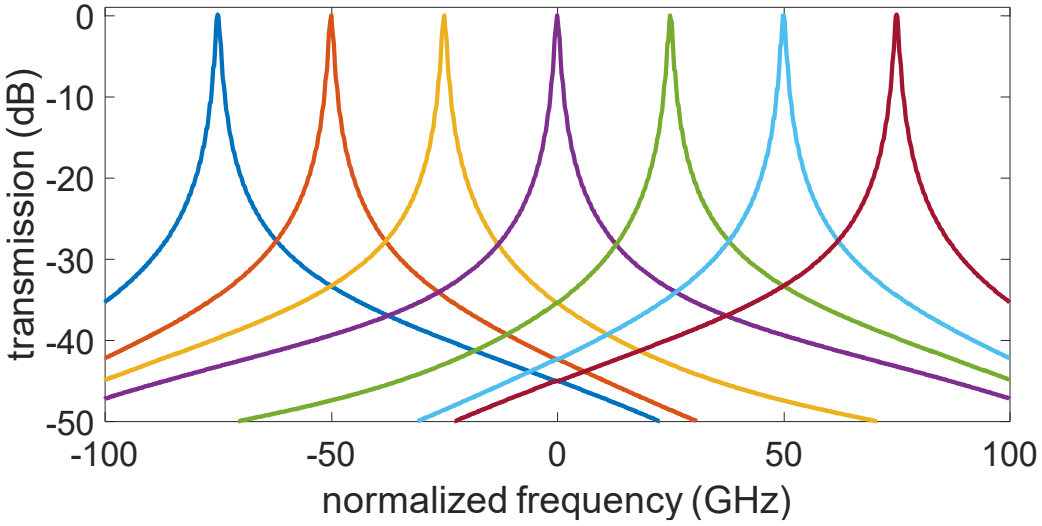

Fig. 5.7. The spectrometer frequency response for different ring resonator tuning frequencies.

The industry specified requirements of the thesis namely, a resolution of lower than 1 GHz, the C-band coverage, the limits in consumed tuning power, footprint, and scanning speed are satisfied.

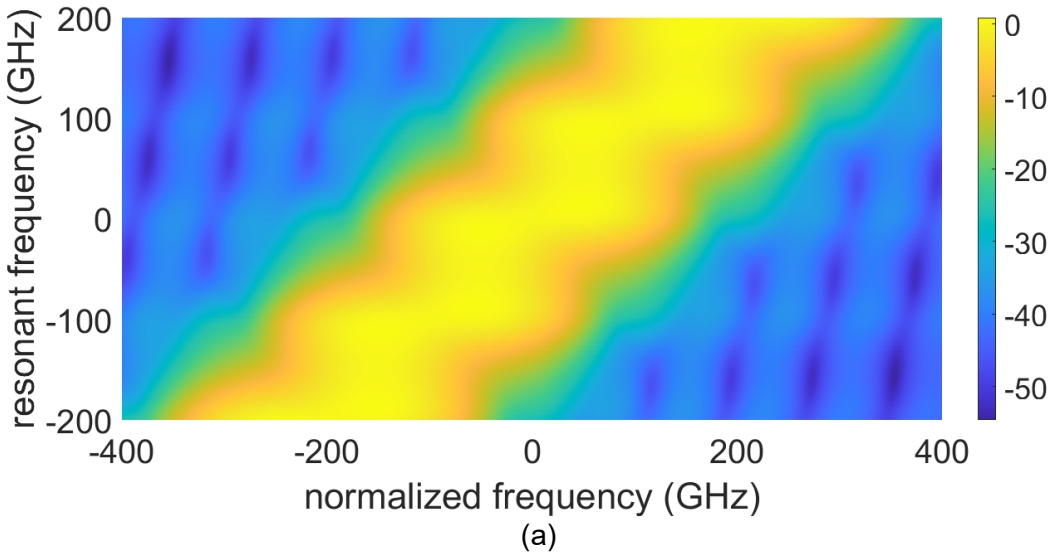

(a)

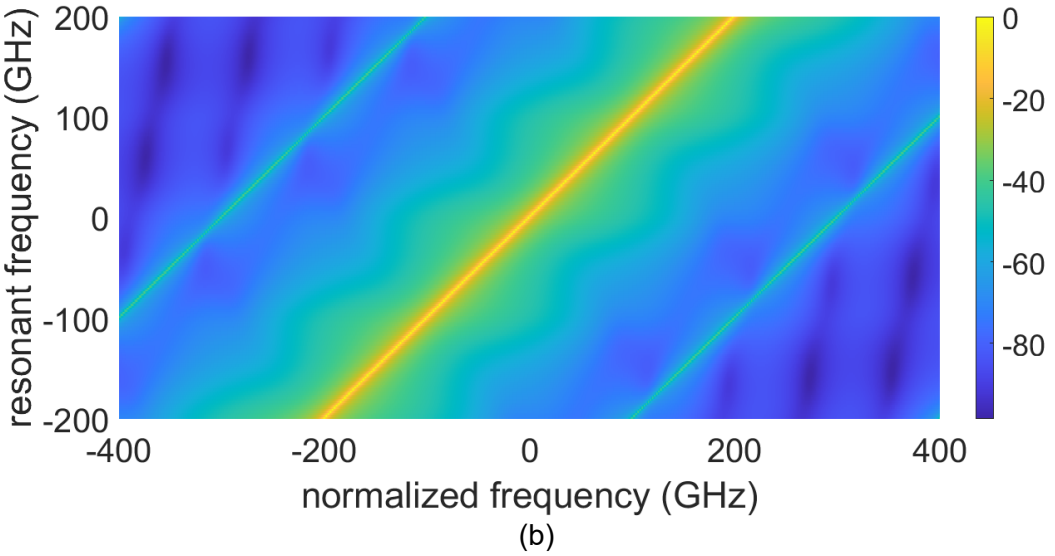

(b)

Fig. 5.8. 3D transmission (dB) views of a) the VCP and b) spectrometer response versus frequency and ring resonator resonant frequency.

5.6 Summary of the main findings

A special AWG was designed to fulfill the requirements for a flat on-resonance scanning of the C-band. The novel AWG eliminates the need for multiple parallel AWGs and has significantly fewer number of arrayed waveguides compared to conventional AWGs, consequently, reducing the footprint and design complication. The frequency

response of the spectrometer consisting of the ring resonator and AWG was simulated. A flat on-resonance scanning of the C-band was attained. A crosstalk level of -40 dB was achieved for a design with an AWG channel spacing and -3dB bandwidth of 100 GHz each, and the ring resonator FSR of 300 GHz. The designed spectrometer meets the industry specified requirements.

Chapter 6 Conclusion

In this chapter, first, a summary of the main findings is provided. Next, original contributions to knowledge are disclosed. Finally, suggestions for future work are made.

6.1 Summary

The project of the thesis was defined in chapter 1, the components and the integration platform for the spectrometer were determined and the objectives of the thesis were outlined. The ring resonator and arrayed waveguide gratings (AWG) on silicon nitride platform were chosen as the main spectrometer components functioning as a fine filter and coarse filter, respectively. The first objective of the thesis was to establish a method to scan the C-band with rub-GHz resolution and acquire a flat response over frequency. The second objective was to evaluate the feasibility of achieving a silicon nitride ring resonator with a resolution of lower than 1 GHz. The third objective was to evaluate thermal tuning of the silicon nitride ring resonator over its free spectral range (FSR), and finally, the last objective was to design a special AWG according to the constraints set by the proposed method for the spectrometer to achieve a flat frequency response.

In chapter 2, the method to achieve a flat on-resonance response with the spectrometer consisting of a ring resonator as the fine filter and an AWG as the coarse filter was introduced. The method is based on the incoherent weighted summation of the AWG output profiles, making a virtual channel profile (VCP) for each resonant frequency of the ring resonator. The weights are assigned based on the frequency position of the

resonant frequencies of the ring resonator with respect to the AWG output channel profile peaks. The resonant frequencies are informed to the processing unit using a wavelength meter. As the ring resonator is tuned, the resonant frequencies are moved and thus, the weights of instantaneous VCPs are altered as well. Applying this technique ensures a flat response is attained over the C-band at any resonant frequency irrespective of varied insertion loss in AWG output channel profiles.

The silicon nitride ring resonator was simulated in chapter 3 to assess its resolution. Bend simulations determined the range of acceptable radii for a ring. Accordingly, the right value of cross coupling power ratio (CCPR) for a resolution of lower than 1 GHz for ring resonators with two different FSRs were calculated. Finally, the gap size in the middle of the ring coupler is computed using the super-mode theory technique. The simulations proved that silicon nitride ring resonators can achieve a resolution of lower than 1 GHz.

In chapter 4, the tunability of silicon nitride ring resonators over their FSRs was evaluated for rings with various FSRs and different waveguides and by using resistive heaters for thermal tuning. The simulations shed light on the effect of different parameters on thermal tuning such as heater width, heater distance from waveguide, and heater material. The maximum allowed tuning range to avoid heater failure, and the corresponding tuning power were computed. Also, the scanning speed for a complete FSR sweep forward and then backward was calculated.

In chapter 5, the AWG specifications based on the requirements of the incoherent weighted summation method and achieved maximum tunable ring resonator FSR are

determined. The AWG was then designed and simulated. The designed AWG meets the required specifications and the combination of the ring resonator as the fine filter and the AWG as the coarse filter with the use of the mentioned method provides a flat on-resonance frequency response for the spectrometer as it sweeps the C-band with a resolution of lower than 1 GHz.

6.2 Contribution to knowledge

The architecture of the spectrometer on silicon nitride platform with a ring resonator as the fine filter and the AWG as the coarse filter together with a method to flatten the on-resonance response was introduced to scan the C-band with a resolution of lower than 1 GHz.

The incoherent weighted summation method was used to achieve a flat on-resonance frequency response regardless of the position of resonant frequencies. It makes VCPs with the weighted summation of AWG output channel profiles at instantaneous resonant frequencies of the ring resonator and filters out each tunable resonant frequency. Its optical part is simpler than the coherent superposition method while its electrical part does not need handovers between channel profiles. It can achieve a flat unity on-resonance response for any resonant frequency while keeping the crosstalk caused by neighboring resonant frequencies at a sufficiently low level. Also, the effect of nonuniformity of the envelope of AWG channel profiles on the spectrometer response is removed by using this method.

The silicon nitride ring resonator was evaluated to determine its bend radius limit and the feasibility of achieving a resolution of lower than 1 GHz. Also, the design of the ring coupler by using different methods was evaluated. It was noted that a resolution of lower than 1 GHz was attainable for silicon nitride ring resonators at the expense of some insertion loss. Moreover, the super-mode theory combined with the mode effective index simulation results was proved to be the right technique to determine the size of the minimum gap in the ring coupler.

The thermal tunability of silicon nitride ring resonators for different waveguide-heater structures was assessed. The effects of heater material, heater width, and heater distance from the waveguide were examined. The ring resonator FSR limit for tuning by the amount of one FSR was identified. Furthermore, scanning speed and tuning power values were computed for rings with different waveguides, heaters, and radii.

The use of multiple parallel AWGs was replaced with a consolidated AWG that was designed to have desired overlapping channel profiles. The design of the special AWG proved to be feasible. The wider input waveguide reduces the number of arrayed waveguides and thus, the overall footprint of the AWG. The reduced footprint not only reduces the fabrication cost of the component but also improves insertion loss as the arrayed waveguides become shorter. By applying the mentioned technique, a flat scanning of the C-band is achieved even though the AWG channel profiles are bell-shaped, and the envelope of the AWG channel profiles is not flat in a cyclic AWG.

6.3 Future research

In this section, suggestions for future work are provided. Some potential directions for the continuation of this work are as follows:

The frequency range of the spectrometer may be extended to cover other optical bands, increasing the capacity of the elastic optical network (EON).

In this thesis, the TE polarization was used for the design of the components. The spectrometer may be designed to be polarization insensitive, operating efficiently for either TE or TM polarizations.

Other tuning methods such as piezo-electric (PE) tuning or electro-optic (EO) tuning may be considered. The techniques mentioned are faster than thermal tuning and an increased scanning speed may be useful in other applications. However, EO tuning is sensitive to polarization and the design of polarization insensitive components with the EO tuning might pose a challenge.

Athermal operation of the spectrometer reduces sensitivity to ambient temperature. However, such a design that keeps the device at a constant temperature cannot be tuned thermally and another tuning method needs to be used.

To increase thermal scanning speed and isolate adjacent components on a chip and reduce thermal crosstalk, trenches may be included between components. However, they cannot be placed too close to the waveguides to avoid their contact with an optical mode and resultant optical loss. The effect of trenches in reducing thermal crosstalk and increasing scanning speed may be assessed.

High-Quality ring resonators trap light in the ring and thus achieve a resolution of lower than 1 GHz. It, however, may cause unwanted non-linear effects if light intensity passes a certain threshold. Future work may evaluate the effects of waveguide type and resolution on non-linearity and determine constraints for a linear operation of silicon nitride ring resonators.

The AWG is sensitive to the phase error emanating from fabrication imperfection in arrayed waveguides and the slab regions in the FPRs. This brings about distortion in AWG output channel frequency responses and an increased background noise level. While increasing AWG channel spacing is helpful in reducing phase error effect, other techniques such as using arrayed waveguides with reduced mode effective index sensitivity to waveguide imperfection may be considered to further improve crosstalk performance.

Rowland circle-based AWGs show the aberration effect, which causes varied side-lobe levels in different output channel profiles. The effect becomes more pronounced at the outer channels of an AWG. The designed AWG in this work may be modified to reduce or eliminate the aberration effect so that the spectrometer performance is not degraded while scanning the outer frequencies of the band.

References

[1] E. Agrell *et al.*, “Roadmap of optical communications,” *J. Opt.*, vol. 18, no. 6, p. 063002, May 2016, doi: 10.1088/2040-8978/18/6/063002.

[2] P. J. Winzer, D. T. Neilson, and A. R. Chraplyvy, “Fiber-optic transmission and networking: the previous 20 and the next 20 years [Invited],” *Opt. Express*, vol. 26, no. 18, pp. 24190–24239, Sep. 2018, doi: 10.1364/OE.26.024190.

[3] R.-J. Essiambre, G. Kramer, P. J. Winzer, G. J. Foschini, and B. Goebel, “Capacity Limits of Optical Fiber Networks,” *J. Light. Technol.*, vol. 28, no. 4, pp. 662–701, Feb. 2010, doi: 10.1109/JLT.2009.2039464.

[4] R.-J. Essiambre and R. W. Tkach, “Capacity Trends and Limits of Optical Communication Networks,” *Proc. IEEE*, vol. 100, no. 5, pp. 1035–1055, May 2012, doi: 10.1109/JPROC.2012.2182970.

[5] P. J. Winzer and R.-J. Essiambre, “Advanced Modulation Formats for High-Capacity Optical Transport Networks,” *J. Light. Technol.*, vol. 24, no. 12, pp. 4711–4728, Dec. 2006, doi: 10.1109/JLT.2006.885260.

[6] D. J. Richardson, J. M. Fini, and L. E. Nelson, “Space-division multiplexing in optical fibres,” *Nat. Photonics*, vol. 7, no. 5, pp. 354–362, May 2013, doi: 10.1038/nphoton.2013.94.

[7] W. Wu, J. Yang, J. Zhang, J. Huang, D. Chen, and H. Wang, “Ultra-high resolution filter and optical field modulator based on a surface plasmon polariton,” *Opt. Lett.*, vol. 41, no. 10, pp. 2310–2313, May 2016, doi: 10.1364/OL.41.002310.

[8] K. Feng *et al.*, “An Optoelectronic Equivalent Narrowband Filter for High Resolution Optical Spectrum Analysis,” *Sensors*, vol. 17, no. 2, Art. no. 2, Feb. 2017, doi: 10.3390/s17020348.

[9] F. Ramiro-Manzano, N. Prtljaga, L. Pavesi, G. Pucker, and M. Ghulinyan, “A fully integrated high-Q Whispering-Gallery Wedge Resonator,” *Opt. Express*, vol. 20, no. 20, pp. 22934–22942, Sep. 2012, doi: 10.1364/OE.20.022934.

[10] D. Kreutz, F. M. V. Ramos, P. E. Veríssimo, C. E. Rothenberg, S. Azodolmolky, and S. Uhlig, “Software-Defined Networking: A Comprehensive Survey,” *Proc. IEEE*, vol. 103, no. 1, pp. 14–76, Jan. 2015, doi: 10.1109/JPROC.2014.2371999.

[11]B. A. A. Nunes, M. Mendonca, X.-N. Nguyen, K. Obraczka, and T. Turletti, “A Survey of Software-Defined Networking: Past, Present, and Future of Programmable Networks,” *IEEE Commun. Surv. Tutor.*, vol. 16, no. 3, pp. 1617–1634, 2014, doi: 10.1109/SURV.2014.012214.00180.

[12] W. Xia, Y. Wen, C. H. Foh, D. Niyato, and H. Xie, “A Survey on Software-Defined Networking,” *IEEE Commun. Surv. Tutor.*, vol. 17, no. 1, pp. 27–51, 2015, doi: 10.1109/COMST.2014.2330903.

[13] O. Gerstel, M. Jinno, A. Lord, and S. J. B. Yoo, “Elastic optical networking: a new dawn for the optical layer?,” *IEEE Commun. Mag.*, vol. 50, no. 2, pp. s12–s20, Feb. 2012, doi: 10.1109/MCOM.2012.6146481.

[14] L. Velasco, A. P. Vela, F. Morales, and M. Ruiz, “Designing, Operating, and Reoptimizing Elastic Optical Networks,” *J. Light. Technol.*, vol. 35, no. 3, pp. 513–526, Feb. 2017.

[15] N. Sabri, S. A. Aljunid, M. S. Salim, R. B. Ahmad, and R. Kamaruddin, “Toward Optical Sensors: Review and Applications,” *J. Phys. Conf. Ser.*, vol. 423, no. 1, p. 012064, Apr. 2013, doi: 10.1088/1742-6596/423/1/012064.

[16] M. F. S. Ferreira *et al.*, “Roadmap on optical sensors,” *J. Opt.*, vol. 19, no. 8, p. 083001, Jul. 2017, doi: 10.1088/2040-8986/aa7419.

[17] X. W. Ye, Y. H. Su, and J. P. Han, “Structural Health Monitoring of Civil Infrastructure Using Optical Fiber Sensing Technology: A Comprehensive Review,” *Sci. World J.*, vol. 2014, no. 1, p. 652329, 2014, doi: 10.1155/2014/652329.

[18] D. V. Strekalov, C. Marquardt, A. B. Matsko, H. G. L. Schwefel, and G. Leuchs, “Nonlinear and quantum optics with whispering gallery resonators,” *J. Opt.*, vol. 18, no. 12, p. 123002, Nov. 2016, doi: 10.1088/2040-8978/18/12/123002.

[19] G. Frigenti, D. Farnesi, G. Nunzi Conti, and S. Soria, “Nonlinear Optics in Microspherical Resonators,” *Micromachines*, vol. 11, no. 3, Art. no. 3, Mar. 2020, doi: 10.3390/mi11030303.

[20] D. Thomson *et al.*, “Roadmap on silicon photonics,” *J. Opt.*, vol. 18, no. 7, p. 073003, Jun. 2016, doi: 10.1088/2040-8978/18/7/073003.

[21] T. Sharma *et al.*, “Review of Recent Progress on Silicon Nitride-Based Photonic Integrated Circuits,” *IEEE Access*, vol. 8, pp. 195436–195446, 2020, doi: 10.1109/ACCESS.2020.3032186.

[22] Z. Yang, T. Albrow-Owen, W. Cai, and T. Hasan, “Miniaturization of optical spectrometers,” *Science*, vol. 371, no. 6528, p. eabe0722, Jan. 2021, doi: 10.1126/science.abe0722.

[23] C.-12 Foundation, “Refraction of Light through a Prism | CK-12 Foundation.” Accessed: Jun. 16, 2024. [Online]. Available: https://flexbooks.ck12.org/cbook/cbse-physics-class-10/section/2.3/primary/lesson/refraction-of-light-through-prism/

[24] R. Cheng, C.-L. Zou, X. Guo, S. Wang, X. Han, and H. X. Tang, “Broadband on-chip single-photon spectrometer,” *Nat. Commun.*, vol. 10, no. 1, p. 4104, Sep. 2019, doi: 10.1038/s41467-019-12149-x.

[25] S. Janz *et al.*, “Planar waveguide echelle gratings in silica-on-silicon,” *IEEE Photonics Technol. Lett.*, vol. 16, no. 2, pp. 503–505, Feb. 2004, doi: 10.1109/LPT.2003.823139.

[26] P. Cheben *et al.*, “A high-resolution silicon-on-insulator arrayed waveguide grating microspectrometer with sub-micrometer aperture waveguides,” *Opt. Express*, vol. 15, no. 5, pp. 2299–2306, Mar. 2007, doi: 10.1364/OE.15.002299.

[27] X. J. M. Leijtens, B. Kuhlow, and M. K. Smit, “Arrayed Waveguide Gratings,” in *Wavelength Filters in Fibre Optics*, H. Venghaus, Ed., Berlin, Heidelberg: Springer, 2006, pp. 125–187. doi: 10.1007/3-540-31770-8_5.

[28] S.-H. Kong, J. H. Correia, G. de Graaf, M. Bartek, and R. F. Wolffenbuttel, “Integrated silicon microspectrometers,” *IEEE Instrum. Meas. Mag.*, vol. 4, no. 3, pp. 34–38, Sep. 2001, doi: 10.1109/5289.953457.

[29] X. Jiang, A. J. Qavi, S. H. Huang, and L. Yang, “Whispering-Gallery Sensors,” *Matter*, vol. 3, no. 2, pp. 371–392, Aug. 2020, doi: 10.1016/j.matt.2020.07.008.

[30] A. Nitkowski, L. Chen, and M. Lipson, “Cavity-enhanced on-chip absorption spectroscopy using microring resonators,” *Opt. Express*, vol. 16, no. 16, pp. 11930–11936, Aug. 2008, doi: 10.1364/OE.16.011930.

[31] M. Erfan, Y. M. Sabry, M. Sakr, B. Mortada, M. Medhat, and D. Khalil, “On-Chip Micro–Electro–Mechanical System Fourier Transform Infrared (MEMS FT-IR) Spectrometer-Based Gas Sensing,” *Appl. Spectrosc.*, vol. 70, no. 5, pp. 897–904, May 2016, doi: 10.1177/0003702816638295.

[32] M. Florjańczyk, P. Cheben, S. Janz, A. Scott, B. Solheim, and D.-X. Xu, “Multiaperture planar waveguide spectrometer formed by arrayed Mach-Zehnder interferometers,” *Opt. Express*, vol. 15, no. 26, pp. 18176–18189, Dec. 2007, doi: 10.1364/OE.15.018176.

[33] B. Redding, S. M. Popoff, and H. Cao, “All-fiber spectrometer based on speckle pattern reconstruction,” *Opt. Express*, vol. 21, no. 5, pp. 6584–6600, Mar. 2013, doi: 10.1364/OE.21.006584.

[34] J. Bao and M. G. Bawendi, “A colloidal quantum dot spectrometer,” *Nature*, vol. 523, no. 7558, pp. 67–70, Jul. 2015, doi: 10.1038/nature14576.

[35] N. Izhaky *et al.*, “Development of CMOS-Compatible Integrated Silicon Photonics Devices,” *IEEE J. Sel. Top. Quantum Electron.*, vol. 12, no. 6, pp. 1688–1698, Nov. 2006, doi: 10.1109/JSTQE.2006.884089.

[36] G.-S. Jeong, W. Bae, and D.-K. Jeong, “Review of CMOS Integrated Circuit Technologies for High-Speed Photo-Detection,” *Sensors*, vol. 17, no. 9, Art. no. 9, Sep. 2017, doi: 10.3390/s17091962.

[37] H. H. Radamson *et al.*, “State of the Art and Future Perspectives in Advanced CMOS Technology,” *Nanomaterials*, vol. 10, no. 8, Art. no. 8, Aug. 2020, doi: 10.3390/nano10081555.

[38] M. Kawachi, “Silica waveguides on silicon and their application to integrated-optic components,” *Opt. Quantum Electron.*, vol. 22, no. 5, pp. 391–416, Sep. 1990, doi: 10.1007/BF02113964.

[39] M. Okuno, “Recent progress on silica-based planar lightwave circuit technology,” in *Technical Digest. CLEO/Pacific Rim ’99. Pacific Rim Conference on Lasers and Electro-Optics (Cat. No.99TH8464)*, Aug. 1999, pp. 583–584 vol.3. doi: 10.1109/CLEOPR.1999.817730.

[40] W. Lin, C. J. Sun, and K. M. Schmidt, “Hybrid integration platform based on silica-on-silicon planar lightwave circuit,” in *Optoelectronic Integrated Circuits IX*, SPIE, Feb. 2007, pp. 49–56. doi: 10.1117/12.714410.

[41] K. Okamoto, “Progress and technical challenge for planar waveguide devices: silica and silicon waveguides,” *Laser Photonics Rev.*, vol. 6, no. 1, pp. 14–23, 2012, doi: 10.1002/lpor.201100003.

[42] W. Bogaerts *et al.*, “Nanophotonic waveguides in silicon-on-insulator fabricated with CMOS technology,” *J. Light. Technol.*, vol. 23, no. 1, pp. 401–412, Jan. 2005, doi: 10.1109/JLT.2004.834471.

[43] F. Amanti *et al.*, “Integrated Photonic Passive Building Blocks on Silicon-on-Insulator Platform,” *Photonics*, vol. 11, no. 6, Art. no. 6, Jun. 2024, doi: 10.3390/photonics11060494.

[44] C. G. H. Roeloffzen *et al.*, “Low-Loss Si3N4 TriPleX Optical Waveguides: Technology and Applications Overview,” *IEEE J. Sel. Top. Quantum Electron.*, vol. 24, no. 4, pp. 1–21, Jul. 2018, doi: 10.1109/JSTQE.2018.2793945.

[45] F. Gan *et al.*, “Maximizing the Thermo-Optic Tuning Range of Silicon Photonic Structures,” in *2007 Photonics in Switching*, Aug. 2007, pp. 67–68. doi: 10.1109/PS.2007.4300747.

[46] W. Jin, R. G. Polcawich, P. A. Morton, and J. E. Bowers, “Piezoelectrically tuned silicon nitride ring resonator,” *Opt. Express*, vol. 26, no. 3, pp. 3174–3187, Feb. 2018, doi: 10.1364/OE.26.003174.

[47] Y. S. Lee, G.-D. Kim, W.-J. Kim, S.-S. Lee, W.-G. Lee, and W. H. Steier, “Hybrid Si-$LiNbO_3$ microring electro-optically tunable resonators for active photonic devices,” *Opt. Lett.*, vol. 36, no. 7, pp. 1119–1121, Apr. 2011, doi: 10.1364/OL.36.001119.

[48] Y. Yang *et al.*, “Thermo-Optically Tunable Silicon AWG With Above 600 GHz Channel Tunability,” *IEEE Photonics Technol. Lett.*, vol. 27, no. 22, pp. 2351–2354, Nov. 2015, doi: 10.1109/LPT.2015.2464073.

[49] Y. Liu *et al.*, “Thermo-Optic Tunable Silicon Arrayed Waveguide Grating at 2-μm Wavelength Band,” *IEEE Photonics J.*, vol. 12, no. 4, pp. 1–8, Aug. 2020, doi: 10.1109/JPHOT.2020.3001595.

[50] K. Ishikawa and Q. Yu, “An Integrated AWG multi/demultiplexer with MEMS-VOA shutters,” in *The Ninth Intersociety Conference on Thermal and Thermomechanical Phenomena In Electronic Systems*, Jun. 2004, pp. 523-528 Vol.2. doi: 10.1109/ITHERM.2004.1318328.

[51] J. W. Provine, D. T. McCormick, D. A. Horsley, and N. C. Tien, “Wavelength routing with MEMS switch and a single AWG,” in *Active and Passive Optical Components for WDM Communications V*, SPIE, Oct. 2005, pp. 269–277. doi: 10.1117/12.630571.

[52] T. Kitoh, Y. Inoue, M. Itoh, M. Kotoku, and Y. Hibino, “Low chromatic-dispersion flat-top arrayed waveguide grating filter,” *Electron. Lett.*, vol. 39, no. 15, pp. 1116–1118, Jul. 2003, doi: 10.1049/el:20030737.

[53] K. Okamoto and H. Yamada, “Arrayed-waveguide grating multiplexer with flat spectral response,” *Opt. Lett.*, vol. 20, no. 1, pp. 43–45, Jan. 1995, doi: 10.1364/OL.20.000043.

[54] K. Maru, T. Mizumoto, and H. Uetsuka, “Demonstration of Flat-Passband Multi/Demultiplexer Using Multi-Input Arrayed Waveguide Grating Combined With Cascaded Mach–Zehnder Interferometers,” *J. Light. Technol.*, vol. 25, no. 8, pp. 2187–2197, Aug. 2007, doi: 10.1109/JLT.2007.901339.

[55] M. Hasan *et al.*, “Ultra-High Resolution Wideband on-Chip Spectrometer,” *IEEE Photonics J.*, vol. 12, no. 5, pp. 1–17, Oct. 2020, doi: 10.1109/JPHOT.2020.3021676.

[56] M. Hasan *et al.*, “Circuit design and integration feasibility of a high-resolution broadband on-chip spectral monitor,” Aug. 11, 2021, *arXiv*: arXiv:2108.10121. doi: 10.48550/arXiv.2108.10121.

[57] M. Hasan *et al.*, “High-resolution Si_3N_4 spectrometer: architecture & virtual channel synthesis and experimental demonstration,” *Opt. Express*, vol. 32, no. 6, pp. 8697–8714, Mar. 2024, doi: 10.1364/OE.509659.

[58] G. M. Hasan, M. Hasan, P. Liu, M. Rad, E. Bernier, and T. J. Hall, “Optical wavelength meter with machine learning enhanced precision,” *Photonics Res.*, vol. 11, no. 3, pp. 420–430, Mar. 2023, doi: 10.1364/PRJ.473686.

[59] K. Okamoto, *Fundamentals of optical waveguides*, 2nd ed. Amsterdam ; Boston: Elsevier, 2006.

[60] M. Popović, “Theory and design of high-index-contrast microphotonic circuits,” Thesis, Massachusetts Institute of Technology, 2008. Accessed: Apr. 09, 2025. [Online]. Available: https://dspace.mit.edu/handle/1721.1/42911

[61] I. Chremmos, O. Schwelb, and N. Uzunoglu, *Photonic Microresonator Research and Applications*. Springer, 2010.

[62] W. Bogaerts *et al.*, “Silicon microring resonators,” *Laser Photonics Rev.*, vol. 6, no. 1, pp. 47–73, 2012, doi: 10.1002/lpor.201100017.

[63] S. Feng, T. Lei, H. Chen, H. Cai, X. Luo, and A. w. Poon, “Silicon photonics: from a microresonator perspective,” *Laser Photonics Rev.*, vol. 6, no. 2, pp. 145–177, 2012, doi: 10.1002/lpor.201100020.

[64] L. Chrostowski *et al.*, “Silicon photonic resonator sensors and devices,” in *Laser Resonators, Microresonators, and Beam Control XIV*, SPIE, Feb. 2012, pp. 387–402. doi: 10.1117/12.916860.

[65] “Physical Layer Modeling and Optimization of Silicon Photonic Interconnection Networks - ProQuest.” Accessed: Apr. 09, 2025. [Online]. Available: https://www.proquest.com/openview/c720b4780cfb5705492e6d6ea8233b86/1?cbl=18750&pq-origsite=gscholar

[66] Z. Yao *et al.*, “Integrated Silicon Photonic Microresonators: Emerging Technologies,” *IEEE J. Sel. Top. Quantum Electron.*, vol. 24, no. 6, pp. 1–24, Nov. 2018, doi: 10.1109/JSTQE.2018.2846047.

[67] H. Lee *et al.*, “Chemically etched ultrahigh-Q wedge-resonator on a silicon chip,” *Nat. Photonics*, vol. 6, no. 6, pp. 369–373, Jun. 2012, doi: 10.1038/nphoton.2012.109.

[68] K. Y. Yang *et al.*, “Broadband dispersion-engineered microresonator on a chip,” *Nat. Photonics*, vol. 10, no. 5, pp. 316–320, May 2016, doi: 10.1038/nphoton.2016.36.

[69] J. V. Hryniewicz, P. P. Absil, B. E. Little, R. A. Wilson, and P.-T. Ho, “Higher order filter response in coupled microring resonators,” *IEEE Photonics Technol. Lett.*, vol. 12, no. 3, pp. 320–322, Mar. 2000, doi: 10.1109/68.826927.

[70] T. Komljenovic, S. Liu, E. Norberg, G. A. Fish, and J. E. Bowers, “Control of Widely Tunable Lasers With High-Q Resonator as an Integral Part of the Cavity,” *J. Light. Technol.*, vol. 35, no. 18, pp. 3934–3939, Sep. 2017.

[71] M. Borselli, T. J. Johnson, and O. Painter, “Beyond the Rayleigh scattering limit in high-Q silicon microdisks: theory and experiment,” *Opt. Express*, vol. 13, no. 5, pp. 1515–1530, Mar. 2005, doi: 10.1364/OPEX.13.001515.

[72] M. Soltani, S. Yegnanarayanan, and A. Adibi, “Ultra-high Q planar silicon microdisk resonators for chip-scale silicon photonics,” *Opt. Express*, vol. 15, no. 8, pp. 4694–4704, Apr. 2007, doi: 10.1364/OE.15.004694.

[73] E. S. Hosseini, S. Yegnanarayanan, A. H. Atabaki, M. Soltani, and A. Adibi, “High Quality Planar Silicon Nitride Microdisk Resonators for Integrated Photonics in the VisibleWavelength Range,” *Opt. Express*, vol. 17, no. 17, pp. 14543–14551, Aug. 2009, doi: 10.1364/OE.17.014543.

[74] M. Soltani, Q. Li, S. Yegnanarayanan, and A. Adibi, “Toward ultimate miniaturization of high Q silicon traveling-wave microresonators,” *Opt. Express*, vol. 18, no. 19, pp. 19541–19557, Sep. 2010, doi: 10.1364/OE.18.019541.

[75] Z. Xia *et al.*, “High resolution on-chip spectroscopy based on miniaturized microdonut resonators,” *Opt. Express*, vol. 19, no. 13, pp. 12356–12364, Jun. 2011, doi: 10.1364/OE.19.012356.

[76] K. Luke, A. Dutt, C. B. Poitras, and M. Lipson, “Overcoming Si_3N_4 film stress limitations for high quality factor ring resonators,” *Opt. Express*, vol. 21, no. 19, pp. 22829–22833, Sep. 2013, doi: 10.1364/OE.21.022829.

[77] Q. Li, A. A. Eftekhar, M. Sodagar, Z. Xia, A. H. Atabaki, and A. Adibi, “Vertical integration of high-Q silicon nitride microresonators into silicon-on-insulator platform,” *Opt. Express*, vol. 21, no. 15, pp. 18236–18248, Jul. 2013, doi: 10.1364/OE.21.018236.

[78] X. Ji *et al.*, “Ultra-low-loss on-chip resonators with sub-milliwatt parametric oscillation threshold,” *Optica*, vol. 4, no. 6, pp. 619–624, Jun. 2017, doi: 10.1364/OPTICA.4.000619.

[79] Y. Xuan *et al.*, “High-Q silicon nitride microresonators exhibiting low-power frequency comb initiation,” *Optica*, vol. 3, no. 11, pp. 1171–1180, Nov. 2016, doi: 10.1364/OPTICA.3.001171.

[80] D. T. Spencer, J. F. Bauters, M. J. R. Heck, and J. E. Bowers, “Integrated waveguide coupled Si_3N_4 resonators in the ultrahigh-Q regime,” *Optica*, vol. 1, no. 3, pp. 153–157, Sep. 2014, doi: 10.1364/OPTICA.1.000153.

[81] “TriPleX Silicon Nitride Waveguide Technology,” LioniX International. Accessed: Apr. 20, 2024. [Online]. Available: https://www.lionix-international.com/photonics/pic-technology/triplex-waveguide-technology/

[82] D. J. Blumenthal, R. Heideman, D. Geuzebroek, A. Leinse, and C. Roeloffzen, “Silicon Nitride in Silicon Photonics,” *Proc. IEEE*, vol. 106, no. 12, pp. 2209–2231, Dec. 2018, doi: 10.1109/JPROC.2018.2861576.

[83] G. M. Hasan *et al.*, “Ring Resonator Gap Determination Design Rule and Parameter Extraction Method for Sub-GHz Resolution Whole C-Band Si3N4 Integrated Spectrometer,” *Photonics*, vol. 9, no. 9, Art. no. 9, Sep. 2022, doi: 10.3390/photonics9090651.

[84] H. A. Haus and W. Huang, “Coupled-mode theory,” *Proc. IEEE*, vol. 79, no. 10, pp. 1505–1518, Oct. 1991, doi: 10.1109/5.104225.

[85] G. L. Pedrola, *Beam Propagation Method for Design of Optical Waveguide Devices*. John Wiley & Sons, 2015.

[86] “Beam propagation method,” *Wikipedia*. Sep. 12, 2023. Accessed: Oct. 07, 2024. [Online]. Available: https://en.wikipedia.org/w/index.php?title=Beam_propagation_method&oldid=1174979431

[87] A. V. Lavrinenko, J. Lægsgaard, N. Gregersen, F. Schmidt, and T. Søndergaard, *Numerical Methods in Photonics*. CRC Press, 2018.

[88] “What is Finite-Difference Time-Domain (FDTD)?” Accessed: Oct. 07, 2024. [Online]. Available: https://www.ansys.com/blog/what-is-fdtd

[89] “MODE - 2.5D varFDTD solver introduction,” Ansys Optics. Accessed: Oct. 07, 2024. [Online]. Available: https://optics.ansys.com/hc/en-us/articles/360034917213-MODE-2-5D-varFDTD-solver-introduction

[90] S. Farahvash, M. Kavehrad, E. S. Simova, and S. K. Juma, “Analysis of optical fibers using eigen mode expansion method,” in *Physics and Simulation of Optoelectronic Devices VI*, SPIE, Jul. 1998, pp. 759–764. doi: 10.1117/12.316729.

[91] “Principles of EigenMode Expansion (EME) - FIMMPROP.” Accessed: Oct. 07, 2024. [Online]. Available: https://www.photond.com/products/fimmprop/fimmprop_introduction_20.htm

[92] J. A. Besley and J. D. Love, “Supermode analysis of fibre transmission,” *IEE Proc. - Optoelectron.*, vol. 144, no. 6, pp. 411–419, Dec. 1997, doi: 10.1049/ip-opt:19971381.

[93] M. Bahadori *et al.*, “Design Space Exploration of Microring Resonators in Silicon Photonic Interconnects: Impact of the Ring Curvature,” *J. Light. Technol.*, vol. 36, no. 13, pp. 2767–2782, Jul. 2018, doi: 10.1109/JLT.2018.2821359.

[94] D. Liang and J. E. Bowers, “Integrated Optoelectronic Devices on Silicon,” *MRS Online Proc. Libr. OPL*, vol. 1396, p. mrsf11, Jan. 2012, doi: 10.1557/opl.2012.140.

[95] M. J. R. Heck *et al.*, “Hybrid Silicon Photonic Integrated Circuit Technology,” *IEEE J. Sel. Top. Quantum Electron.*, vol. 19, no. 4, pp. 6100117–6100117, Jul. 2013, doi: 10.1109/JSTQE.2012.2235413.

[96] A. Rahim *et al.*, “Expanding the Silicon Photonics Portfolio With Silicon Nitride Photonic Integrated Circuits,” *J. Light. Technol.*, vol. 35, no. 4, pp. 639–649, Feb. 2017.

[97] M. K. Smit and C. Van Dam, “PHASAR-based WDM-devices: Principles, design and applications,” *IEEE J. Sel. Top. Quantum Electron.*, vol. 2, no. 2, pp. 236–250, Jun. 1996, doi: 10.1109/2944.577370.

[98] H. Ghorbani, R. Tewari, M. Rad, E. Bernier, and T. J. Hall, “Design and Simulation of a Si3N4 Sub-GHz Resolution Integrated Micro-Spectrometer,” in *2019 International Conference on Numerical Simulation of Optoelectronic Devices (NUSOD)*, Jul. 2019, pp. 45–46. doi: 10.1109/NUSOD.2019.8806837.

[99] M. Hasan *et al.*, “Circuit architecture and integration feasibility of a high-resolution broadband on-chip spectral sensor,” in *OSA Advanced Photonics Congress (AP) 2020 (IPR, NP, NOMA, Networks, PVLED, PSC, SPPCom, SOF) (2020), paper SpM3I.1*, Optica Publishing Group, Jul. 2020, p. SpM3I.1. doi: 10.1364/SPPCOM.2020.SpM3I.1.

[100] Z. Zhang *et al.*, “Integrated scanning spectrometer with a tunable micro-ring resonator and an arrayed waveguide grating,” *Photonics Res.*, vol. 10, no. 5, pp. A74–A81, May 2022, doi: 10.1364/PRJ.443039.

[101] J. F. Bauters, J. R. Adleman, M. J. R. Heck, and J. E. Bowers, “Design and characterization of arrayed waveguide gratings using ultra-low loss Si3N4 waveguides,” *Appl. Phys. A*, vol. 116, no. 2, pp. 427–432, Aug. 2014, doi: 10.1007/s00339-014-8494-0.

[102] D. Martens *et al.*, “Compact Silicon Nitride Arrayed Waveguide Gratings for Very Near-Infrared Wavelengths,” *IEEE Photonics Technol. Lett.*, vol. 27, no. 2, pp. 137–140, Jan. 2015, doi: 10.1109/LPT.2014.2363298.

[103] D. Dai *et al.*, “Low-loss Si_3N_4 arrayed-waveguide grating (de)multiplexer using nano-core optical waveguides,” *Opt. Express*, vol. 19, no. 15, pp. 14130–14136, Jul. 2011, doi: 10.1364/OE.19.014130.

[104] R. Baets *et al.*, “Silicon Photonics: silicon nitride versus silicon-on-insulator,” in *Optical Fiber Communication Conference (2016), paper Th3J.1*, Optica Publishing Group, Mar. 2016, p. Th3J.1. doi: 10.1364/OFC.2016.Th3J.1.

[105] J. P. George *et al.*, “Lanthanide-Assisted Deposition of Strongly Electro-optic PZT Thin Films on Silicon: Toward Integrated Active Nanophotonic Devices,” *ACS Appl. Mater. Interfaces*, vol. 7, no. 24, pp. 13350–13359, Jun. 2015, doi: 10.1021/acsami.5b01781.

[106] F. Eltes, J. Fompeyrine, and S. Abel, “BaTiO3-based modulators for integrated optical interconnects,” in *Optical Interconnects XIX*, SPIE, Mar. 2019, pp. 153–158. doi: 10.1117/12.2511464.

[107] B. Desiatov, A. Shams-Ansari, M. Zhang, C. Wang, and M. Lončar, “Ultra-low-loss integrated visible photonics using thin-film lithium niobate,” *Optica*, vol. 6, no. 3, pp. 380–384, Mar. 2019, doi: 10.1364/OPTICA.6.000380.

[108] C.-T. Wang *et al.*, “Highly sensitive optical temperature sensor based on a SiN micro-ring resonator with liquid crystal cladding,” *Opt. Express*, vol. 24, no. 2, pp. 1002–1007, Jan. 2016, doi: 10.1364/OE.24.001002.

[109] M. Notaros, T. Dyer, M. Raval, C. Baiocco, J. Notaros, and M. R. Watts, “Integrated visible-light liquid-crystal-based phase modulators,” *Opt. Express*, vol. 30, no. 8, pp. 13790–13801, Apr. 2022, doi: 10.1364/OE.454494.

[110] J. P. Epping *et al.*, “Ultra-low-power stress-optics modulator for microwave photonics,” in *Integrated Optics: Devices, Materials, and Technologies XXI*, SPIE, Feb. 2017, pp. 80–87. doi: 10.1117/12.2266170.

[111] N. Hosseini *et al.*, “Stress-optic modulator in TriPleX platform using a piezoelectric lead zirconate titanate (PZT) thin film,” *Opt. Express*, vol. 23, no. 11, pp. 14018–14026, Jun. 2015, doi: 10.1364/OE.23.014018.

[112] P. R. Stanfield, A. J. Leenheer, C. P. Michael, R. Sims, and M. Eichenfield, “CMOS-compatible, piezo-optomechanically tunable photonics for visible wavelengths and cryogenic temperatures,” *Opt. Express*, vol. 27, no. 20, pp. 28588–28605, Sep. 2019, doi: 10.1364/OE.27.028588.

[113] P. Pintus *et al.*, “PWM-Driven Thermally Tunable Silicon Microring Resonators: Design, Fabrication, and Characterization,” *Laser Photonics Rev.*, vol. 13, no. 9, p. 1800275, 2019, doi: 10.1002/lpor.201800275.

[114] K. Chen, F. Duan, and Y. Yu, “Performance-enhanced silicon thermo-optic Mach–Zehnder switch using laterally supported suspended phase arms and efficient electrodes,” *Opt. Lett.*, vol. 44, no. 4, pp. 951–954, Feb. 2019, doi: 10.1364/OL.44.000951.

[115] Y. Xie *et al.*, “Thermally-Reconfigurable Silicon Photonic Devices and Circuits,” *IEEE J. Sel. Top. Quantum Electron.*, vol. 26, no. 5, pp. 1–20, Sep. 2020, doi: 10.1109/JSTQE.2020.3002758.

[116] A. Mirza, F. Sunny, P. Walsh, K. Hassan, S. Pasricha, and M. Nikdast, “Silicon Photonic Microring Resonators: A Comprehensive Design-Space Exploration and Optimization Under Fabrication-Process Variations,” *IEEE Trans. Comput.-Aided Des. Integr. Circuits Syst.*, vol. 41, no. 10, pp. 3359–3372, Oct. 2022, doi: 10.1109/TCAD.2021.3132555.

[117] S. Yan *et al.*, “Slow-light-enhanced energy efficiency for graphene microheaters on silicon photonic crystal waveguides,” *Nat. Commun.*, vol. 8, no. 1, p. 14411, Feb. 2017, doi: 10.1038/ncomms14411.

[118] Y. Yi, P. Pignalosa, and D. Wu, “Tunable and Ultra-Small Graphene Integrated Silicon Racetrack Micro Resonator,” *IEEE J. Sel. Top. Quantum Electron.*, vol. 23, no. 1, pp. 173–178, Jan. 2017, doi: 10.1109/JSTQE.2016.2604365.

[119] C. Qiu, Y.-B. Wang, Y.-Y. Chen, Y.-X. Lei, L. Qin, and L.-J. Wang, “Design and Analysis of a Novel Graphene-Assisted Silica/Polymer Hybrid Waveguide With Thermal–Optical Phase Modulation Structure,” *IEEE Photonics J.*, vol. 11, no. 2, pp. 1–10, Apr. 2019, doi: 10.1109/JPHOT.2019.2909003.

[120] J. Hernández-Betanzos, M. Blasco-Solvas, C. Domínguez-Horna, and J. Faneca, “Advancements in CMOS-Compatible Silicon Nitride Optical Modulators via Thin-Film Crystalline or Amorphous Silicon p–n Junctions,” *Photonics*, vol. 11, no. 8, Art. no. 8, Aug. 2024, doi: 10.3390/photonics11080762.

[121] M. Jacques, A. Samani, E. El-Fiky, D. Patel, Z. Xing, and D. V. Plant, “Optimization of thermo-optic phase-shifter design and mitigation of thermal crosstalk on the SOI platform,” *Opt. Express*, vol. 27, no. 8, pp. 10456–10471, Apr. 2019, doi: 10.1364/OE.27.010456.

[122] D. Pérez *et al.*, “Thermal tuners on a Silicon Nitride platform,” Apr. 11, 2016, *arXiv*: arXiv:1604.02958. doi: 10.48550/arXiv.1604.02958.

[123] R. Alemany, P. Muñoz, D. Pastor, and C. Domínguez, “Thermo-Optic Phase Tuners Analysis and Design for Process Modules on a Silicon Nitride Platform,” *Photonics*, vol. 8, no. 11, Art. no. 11, Nov. 2021, doi: 10.3390/photonics8110496.

[124] S. S. Cheung and M. R. T. Tan, “Silicon Nitride (Si_3N_4) (De-)Multiplexers for 1-μm CWDM Optical Interconnects,” *J. Light. Technol.*, vol. 38, no. 13, pp. 3404–3413, Jul. 2020.

[125] “Technology,” LIGENTEC. Accessed: Apr. 20, 2024. [Online]. Available: https://www.ligentec.com/technology/

[126] Chu T. K. and C. Y. Ho, “Electrical Resistivity of Chromium, Cobalt, Iron, and Nickel.” Accessed: Apr. 20, 2024. [Online]. Available: https://apps.dtic.mil/sti/citations/tr/ADA129078

[127] H. Takahashi, K. Oda, H. Toba, and Y. Inoue, “Transmission characteristics of arrayed waveguide N/spl times/N wavelength multiplexer,” *J. Light. Technol.*, vol. 13, no. 3, pp. 447–455, Mar. 1995, doi: 10.1109/50.372441.

[128] C. R. Doerr and K. Okamoto, “Advances in Silica Planar Lightwave Circuits,” *J. Light. Technol.*, vol. 24, no. 12, pp. 4763–4789, Dec. 2006, doi: 10.1109/JLT.2006.885255.

[129] D. Wang, G. Jin, Y. Yan, and M. Wu, “Aberration theory of arrayed waveguide grating,” *J. Light. Technol.*, vol. 19, no. 2, pp. 279–284, Feb. 2001, doi: 10.1109/50.917905.

[130] N. Cvetojevic, N. Jovanovic, J. Lawrence, M. Withford, and J. Bland-Hawthorn, “Developing arrayed waveguide grating spectrographs for multi-object astronomical spectroscopy,” *Opt. Express*, vol. 20, no. 3, pp. 2062–2072, Jan. 2012, doi: 10.1364/OE.20.002062.

[131] J. Zou, Z. Le, J. Hu, and J.-J. He, “Performance improvement for silicon-based arrayed waveguide grating router,” *Opt. Express*, vol. 25, no. 9, pp. 9963–9973, May 2017, doi: 10.1364/OE.25.009963.

[132] J. Zou *et al.*, “High Resolution and Ultra-Compact On-Chip Spectrometer Using Bidirectional Edge-Input Arrayed Waveguide Grating,” *J. Light. Technol.*, vol. 38, no. 16, pp. 4447–4453, Aug. 2020.

[133] A. Stoll, K. V. Madhav, and M. M. Roth, “Design, simulation and characterization of integrated photonic spectrographs for astronomy: generation-I AWG devices based on canonical layouts,” *Opt. Express*, vol. 29, no. 16, pp. 24947–24971, Aug. 2021, doi: 10.1364/OE.430794.

[134] A. Stoll, K. Madhav, and M. Roth, “Design, simulation and characterization of integrated photonic spectrographs for astronomy II: low-aberration Generation-II AWG devices with three stigmatic points,” *Opt. Express*, vol. 29, no. 22, pp. 36226–36241, Oct. 2021, doi: 10.1364/OE.438943.

[135] J. Zhan, Y. Zhang, W.-L. Hsu, S. Veilleux, and M. Dagenais, “Design and implementation of a Si_3N_4 three-stigmatic-point arrayed waveguide grating with a resolving power over 17,000,” *Opt. Express*, vol. 31, no. 4, pp. 6389–6400, Feb. 2023, doi: 10.1364/OE.480823.

Appendix A

The thermal and electromagnetic properties of the materials used in the simulations are shown in Table A.1. The presented values are taken on the upper edge of the C-band (1565 nm) and at the room temperature (293.15 °K). Empty cells indicate that the respective property is not used in the simulations. It should be noted that the optical absorption and scattering loss of silica and silicon nitride waveguide structures are used combined (separately for each material) in the simulations as provided in section 4.5 and are not available individually.

Table A.1. The thermal and electromagnetic properties of the materials used in the simulations

Material	Specific heat (J/Kg. K)	Density (Kg/m^3)	Thermal Conductivity (W/m. K)	Electrical resistivity (Ω. m)	Optical absorption coefficient (1/cm)
Silica (SiO_2)	703	2203	1.38	-	-
Silicon nitride (Si_3N_4)	650	2900	30	-	-
Silicon (Si)	700	2329	130	-	-
Chromium (Cr)	480	7150	89	7.5~9E-07	3.3825E+05
Aluminum (Al)	904	2700	235	3.3E-08	1.27E+06
Silver (Ag)	230	10500	420	1.58E-08	-

Appendix B

MATLAB codes used in simulations are attached here.

B1. MATLAB code for Fig. 3.5

The following MATLAB code is used for the simulation of Fig. 3.5. In this code, the values of wavelength, effective and group index values, loss, and desired cross-coupling power values are input, and MATLAB computes the drop port transmission as well as FWHM, FSR, finesse, and Quality factor.

```
%---------------------------------------
% MATLAB code for Fig 3.5
clear;
clc;
clf;

lam0 = 1.5475e-6; % simulated wavelength
Neff=1.5303; % mode effective index
Ng0=1.7694; % group index


coupler_loss= 0; % coupling loss for ring coupler #1
k1 = [sqrt(0.04) sqrt(0.0135)]; % amplitude coupling ratio for ring coupler #1
loss2= 0.5 ; % intrinsic + bend loss (dB/cm)
R =[540e-6 180e-6]; % bend radius

L =2*pi*R; % ring length
lambda =1e-9*(1530:0.0001:1565); % wavelength
phi =(2*pi./(lambda.'))*Neff*L; % corresponding phase shift in one round-trip
r1 = sqrt(1-k1.^2); % self-coupling amplitude ratio for ring coupler #1
r2 = r1; % self coupling amplitude ratio for ring coupler #2
loss3 = L.*1e2*loss2; % total round trip loss (dB)
a = sqrt((10.^(-0.1*loss3))*(1-coupler_loss)^2); % round-trip amplitude transmission
due only to loss


phi0 =2*pi/lam0*Neff*L; % phase at the simulation wavelength
m0 =fix(phi0./2/pi); % integer m value near the simulation wavelength
lam0_res =Neff*L./m0; % actual resonant wavelength near the simulated wavelength
FWHM0 =(1-r1.*r2.*a).*(lam0_res).^2./(pi*Ng0*L.*sqrt(r1.*r2.*a))*1e12; % FWHM (pm)
FSR0 =lam0^2/Ng0./L*1e9; % FSR (nm)

% drop port transmission plot
```

```
Td= ((1-r1.^2).*(1-r2.^2).*a).'./(1-2*(r1.*r2.*a).'.*cos(phi.')+((r1.*r2.*a).^2).');
% Drop port transmission
plot(lambda*1e6, 10*log10(Td(1,:)), '-b','LineWidth',3);
hold on;
plot(lambda*1e6, 10*log10(Td(2,:)), ':k','LineWidth',3);
legend('FSR= 50 GHz','FSR= 150 GHz','location', 'best','NumColumns',2);
xlabel('wavelength (um)')
ylabel('power transmission (dB)')
xlim([1.546 1.55])
ax = gca;
ax.FontSize = 30;
box on

F = FSR0*1e-9./FWHM0*1e12; % Finesse
Q = lam0_res./FWHM0*1e12; % Quality Factor
%---------------------------------------
```

B2. MATLAB code to compute the effective mode width of arrayed waveguides at the FPR interface

The effective mode width of arrayed waveguides at the FPR interface is attached.

```
%---------------------------------------
% Effective mode width computation


A1=importdata('The text file extracted from FIMMWAVE.txt'); % horizontal electric
field
A2=A1.data;
plot(A2(:,1),A2(:,2)) % polting the electric field
integral_1=trapz(A2(:,1),(A2(:,2)).^2);
w_e=integral_1/(max(A2(:,2))^2)*1e-6; % effective mode width of arrayed waveguides at
FPR interface
%---------------------------------------
```

B3. MATLAB code for Fig. 5.6

The MATLAB code to generate Fig. 5.6 is attached. For any AWG output channel frequency response data loaded, and the assigned ring resonator FSR, plots for the VCP and overall spectrometer responses can be generated.

```
%----------------------------------------
% AWG 100 GHz channel spacing and 100 GHz of -3 dB bandwidth
% Ring resonator FSR 300 GHz
% waveguide Si3N4 400 nm thick AN400
% C-band (1530 - 1565 nm)

clear;
clc;
clf;
fig = 0;

fop = 0; % operating centre frequency ~ (-1700, 1700) GHz

% load the data
lam = readmatrix('AWG_w_4_CH_100GHz_BW_100GHz.xlsx','Range', 'B5:B3504');   % vacuum
wavelength (um)
awg = readmatrix('AWG_w_4_CH_100GHz_BW_100GHz.xlsx','Range', 'EG5:FX3504'); % channel
spectra power (dB)

x = ((1./lam)-(1/1.5475))*299792.458; % frequency offset in GHz from 1.5475 um

p = 10.^(awg/10); % power in Watt

% AWG virtual channel sythesis
m = 5; % the number of resonant frequencies (arbitrary)
n = 16*4096; % the number of frequency points
y = linspace(fop-200,fop+200,m);      % tuning frequency
xq = linspace(fop-400,fop+400,n);   % source frequency

for j = 1:m
     f = y(j);    % detuning (GHz)
     a = zeros(1,n);
     b = zeros(1,n);
    for k = 1:44 % number of output channels
        w = g(f+(k-22.5)*100,100);
        a = a + w*interp1(x,p(:,k),xq,'spline');
        b = b + w*w;
    end

    z1 = a./b;
    z2 = h(xq-f,300);
    z3 = z2.*z1;

    % log plot
    z1 = 10*log10(z1);
    z2 = 10*log10(z2);
    z3 = 10*log10(z3);
```

```
    fig = fig + 1;
    figure(fig);
    plot(xq,z1,'b-',xq,z3,'r-','linewidth',4)
%     grid on
%     grid minor

    xlabel('normalized frequency (GHz)')
    ylabel('transmission (dB)')
    legend('AWG','Ring + AWG','location','best')
    axis([fop-400 fop+400 -60 1])
    ax = gca;
    ax.FontSize = 30;
    box on
    pause(0.1);

end


function t = h(x,fsr)
% Ring resonator
bw = 1; % bandwidth (GHz)
z = exp(1i*2*pi*x/fsr);
p = exp(-bw*pi/fsr);
w = 1-p./z;
t = abs((1-p)./w).^2;     % ring power transmission
end

function t = g(x,bw)
% Gaussian AWG channel power spectra / weights
    sig = bw/(2*sqrt(log(2)));
    t = (10^(-0.330786941))*exp(-((x/sig).^2));
    % this coefficient (10^(-0.330786941)) is to make sure the weight
    % function has the same peak as AWG channel profiles (in this case,
    % middle channel profile as the primary resonance is around that channel profile)
end
%----------------------------------------
```